Retrieval of Upper Stratospheric and Lower Mesospheric Ozone Profiles from SCIAMACHY Limb Scatter Measurements and Observations of the Ozone Depletion During the Solar Proton Event in October and November 2003

von
Dipl.-Phys. Günter J. Rohen

30. März 2006

Contents

Abstract

The purpose of this thesis is to establish a retrieval technique which provides reliable ozone concentration profiles in the upper stratosphere and lower mesosphere. This technique uses ultraviolet limb scatter measurements from the eight-channel-spectrometer SCIAMACHY on board the environmental satellite Envisat of the European Space Agency. Comprehensive sensitivity studies and profile validations have been done in order to analyze the ozone data quality. The retrieved profiles are used to explore novel (geo)physical features of the upper atmosphere.

For the inversion, the strongly absorbant Hartley bands of ozone between 250 and 310 nanometer were used. Fraunhofer lines and emission lines from atmospheric constituents had to be taken into account for the selection of what ended up being thirteen appropriate wavelengths. The inversion of the limb radiance profiles to ozone concentration profiles is achieved with an Optimal Estimation iteration scheme, applying the atmospheric radiative transfer model SCIARAYS. This fully spherical model derives the weighting functions analytically and considers the first two orders of Rayleigh-King scattering. The second order of scattering is shown to be negligible. Thus, the computational rate of the retrieval is shown to be fairly high.

The retrieved vertical ozone profiles are supposed to cover an altitude range as wide as possible. The technique used here provides a high sensitivity at an altitude between thirty-five and sixty-five kilometers. A vertical resolution of about three to four kilometers is reached. Weighting functions and averaging kernels reveal an area of high sensitivity of up to seventy kilometers, although the sensitivity decreases significantly above sixty-five kilometers.

Fits of the respective modeled and measured limb radiance profiles

have been analyzed to optimize the selection of wavelengths. They show a root-mean-square agreement of about 1.5 percent. The retrieval is almost independent on *a priori* information. Sensitivity studies show an accuracy on the retrieved profiles below twenty percent, whereas the largest error source is an incorrect tangent height registration. The accuracy of the tangent height specification of about five hundred meters is achieved by an upstream tangent height retrieval. Further error sources are the uncertainties of the solar zenith angle specification and the temperature-dependent cross sections. This is followed by a quantitative and overall summary of the ascertained errors.

Comprehensive validations with coinciding observations from the MIPAS and HALOE spectrometers and from a ground based microwave radiometer show an agreement within ten percent, at least for altitudes between thirty-five and fifty kilometers. The validation above fifty kilometers is still incomplete. Nevertheless, comparisons show reasonable agreement, and even above fifty kilometers an agreement within the derived errors is achieved.

Profiles were retrieved operationally for the whole SCIAMACHY measurement data set since July 2002. They are used to describe the global morphology of ozone in the upper atmosphere. The ozone gradient from the summer to the winter hemisphere in the lower mesosphere has been displayed and quantified. In addition to the expected tropical stratospheric ozone maximum in the summer hemispheres, a large accumulation of ozone at the edge of the polar vortex (called 'collar effect') is observed.

Apart from the establishment of the retrieval technique, a second major focus of the thesis is on observations of the ozone depletion during the historically large solar proton storm between 26 October and 6 November 2003, known as the 'Halloween' storm. Detailed maps and daily resolved time series up to five weeks after the first event have been compared with the results from a chemistry, transport, and photolysis model of the middle atmosphere that includes the production of the ozone destructive catalysts HO_x (H, OH, H_2O) and NO_x (N, NO, NO_2) due to highly energetic particle precipitation.

A strong ozone depletion of more than fifty percent down into the stratosphere is observed at high geomagnetic latitudes in the northern

hemisphere, whereas the observed ozone depletion in the more sunlit southern hemisphere is much weaker.

Two regimes can be distinguished, one above about fifty kilometers dominated by HO_x and one below about fifty kilometers, dominated by NO_x driven ozone loss. The regimes display a different temporal behavior of ozone depletion and recovery. The presented observations of two contemporaneous maxima of ozone depletion at different altitudes are caused by these HO_x and NO_x regimes and are the first ever observed.

SCIAMACHY near-infrared spectra of $O_2(a^1\Delta_g \to X^3\Sigma_g^-)$ transitions at $1.27\,\mu m$ are used to quantify the limb emission rates of this transition spectra during the 'Halloween' storm, accompanying the ozone depletion. A strong anti-correlation between the ozone depletion and the limb emission rates of the $O_2(a^1\Delta_g \to X^3\Sigma_g^-)$ transitions is identified and described. They indicate novel facilities to provide information about this Solar–Earth interaction.

Publication List

The work that was performed for this thesis gave rise to the following publications:

Peer-Reviewed Publications in Journals

Rohen, G., von Savigny, C., Sinnhuber, M., Llewellyn, E. J., Kaiser, J. W., Jackman, C. H., Kallenrode, M.-B., Schröter, J., Eichmann, K.-U., Bovensmann, H. and Burrows, J. P., 2005: Ozone depletion during the solar proton events of October/November 2003 as seen by SCIAMACHY. *J. Geophys. Res.*, **110**, A9, A09S39, DOI `10.1029/2004JA010984`.

Rohen, G. J., von Savigny, C., Llewellyn, E. J., Kaiser, J. W., Eichmann, K.-U., Bracher, A., Bovensmann, H. and Burrows, J. P., 2006: First results of ozone profiles between 35 and 65 km retrieved from SCIAMACHY limb spectra and observations of ozone depletion during the solar proton events in Oct./Nov. 2003. *Adv. Space Res.*, **37**(12), 2263-2268, DOI `10.1016/j.asr.2005.03.160`.

Bracher, A., Bovensmann, H., Bramstedt, K., Burrows, J. P., von Clarmann, T., Eichmann, K.-U., Fischer, H., Funke, B., Gil-López, S., Glatthor, N., Grabowski, U., Höpfner, M., Kaufmann, M., Kellmann, S., Kiefer, M., Koukouli, M. E., Linden, A., López-Puertas, M., Tsidu, G. M., Milz, M., Noël, S., Rohen, G., Rozanov, A., Rozanov, V. V., v. Savigny, C., Sinnhuber, M., Skupin, J., Steck, T., Stiller, G. P., Wang, D.-Y., Weber, M. and Wuttke, M. W., 2005: Cross comparisons of O_3 and NO_2 measured by the atmospheric Envisat instruments GOMOS, MIPAS, and SCIAMACHY. *Adv. in Space Res.*, **36**, 855–867, DOI `10.1016/j.asr.2005.04.005`.

Conference Contributions

Rozanov, A. V., Eichmann, K.-U., von Savigny, C., Rohen, G. J., von König, M., Bovensmann, H., Rozanov, V. V. and Burrows, J. P., 2003: Bestimmung atmosphärischer Spurenstoffprofile aus Sciamachy Limb-Streulichtmessungen. 67$^{\text{th}}$ Tagung der Deutschen Physikalischen Gesellschaft (Dpg), Hannover, Germany, 24–28 March.

Rohen, G. J., von Savigny, C., Eichmann, K.-U., Kaiser, J. W., De-Grandpre, J., Bovensmann, H. and Burrows, J. P., 2003: Mesospheric ozone profiles retrieved from Sciamachy limb measurements: first results. Invited talk, 1$^{\text{st}}$ Limb Workshop, Bremen, Germany, 14–16 April.

Rohen, G. J., von Savigny, C., Llewellyn, E. J., Kaiser, J. W., Eichmann, K.-U., Bracher, A., Sinnhuber, M., Bovensmann, H. and Burrows, J. P., 2004: Retrieval of upper stratospheric/lower mesospheric ozone profiles from Sciamachy limb spectra. 2$^{\text{nd}}$ Limb Workshop, Stockholm, Sweden, 11–14 October.

Rohen, G. J., von Savigny, C., Llewellyn, E. J., Kaiser, J. W., Eichmann, K.-U., Bracher, A., Sinnhuber, M., Bovensmann, H., Burrows, J. P., Jackman, C. H. and Kallenrode, M.-B., 2005: Ozone profile retrieval in the Hartley bands from Sciamachy limb spectra: theory and applications. Invited talk, Mipas Imk Data User Meeting, Imk, Karlsruhe, Germany, 8 December.

Rohen, G. J., von Savigny, C., Llewellyn, E. J., Kaiser, J. W., Eichmann, K.-U., Bracher, A., Sinnhuber, M., Bovensmann, H., Burrows, J. P., Jackman, C. H. and Kallenrode, M.-B., 2006: Retrieval of mesospheric ozone profiles from Sciamachy limb spectra: theory and applications. Saddu Meeting, Bremen, Germany, 12–13 January.

Rohen, G. J., von Savigny, C., Llewellyn, E. J., Kaiser, J. W., Eichmann, K.-U., Bracher, A., Sinnhuber, M., Bovensmann, H., Burrows, J. P., Jackman, C. H. and Kallenrode, M.-B., 2006: Ozone depletion during the Halloween storm. Invited talk, Awi Blockseminar, Bremerhaven, Germany, 13 February.

Rohen, G. J., von Savigny, C., Llewellyn, E. J., Kaiser, J. W., Eich-

mann, K.-U., Bracher, A., Sinnhuber, M., Bovensmann, H., Burrows, J. P., Jackmann, C. H. and Kallenrode, M.-B., 2006: Retrieval of mesospheric ozone profiles from SCIAMACHY limb measurements: theory and applications. Invited talk, Forschungszentrum Jülich, ICG-1, Jülich, Germany, 28 February.

Rohen, G. J., von Savigny, C., Llewellyn, E. J., Kaiser, J. W., Eichmann, K.-U., Bracher, A., Sinnhuber, M., Bovensmann, H. and Burrows, J. P., 2006: Retrieval of ozone profiles in the upper stratosphere and lower mesosphere from SCIAMACHY limb spectra in the Hartley bands. 3$^{\text{rd}}$ International Limb Workshop, Montreal, Canada, 25–28 April.

Rohen, G. J., von Savigny, C., Llewellyn, E. J., Kaiser, J. W., Eichmann, K.-U., Bracher, A., Sinnhuber, M., Bovensmann, H. and Burrows, J. P., 2006: Ozone profile retrievals in the Hartley bands from SCIAMACHY limb measurements; theory and applications. 36$^{\text{th}}$ COSPAR Scientific Assembly, Beijing, China, 16–23 July (submitted).

Rohen, G. J., von Savigny, C., Llewellyn, E. J., Kaiser, J. W., Bracher, A., Sinnhuber, M., Bovensmann, H., Burrows, J. P., Jackman, C. H., and Kallenrode, M. B., 2006: Retrieval of mesospheric ozone profiles from SCIAMACHY limb scatter measurements in the Hartley bands: methodology, tests and applications. 3$^{\text{rd}}$ Workshop on the Atmospheric Chemistry Validation of Envisat (ACVE-[3]), ESA-ESRIN, Frascati, Italy, 4–7 September (submitted).

1 Motivation, Aims, and Structure of this Work

In 1840, Schönbein noticed the same sharp smell of a product of water electrolysis in his laboratory and also near a lightning strike in his village church. He seized upon a suggestion of a workmate and named it ozone (*from Greek ozein*: 'smell'). Walter Noel Hartley identified this gas later as a substance which absorbs atmospheric ultraviolet solar radiation in the spectral range below 290 nm (Hartley, 1881). In his honor, the corresponding absorption bands were named the 'Hartley bands'.

The importance of the absorbing property of ozone for life was not full realized for the next one hundred years until ozone observations from a ground based spectrometer led to the discovery of large ozone losses over the Antarctic Halley Bay (Farman et al., 1985). The lethal threat of ultraviolet radiation focused public interest on the concerns that anthropogenic activity could alter the natural composition of the atmosphere. Since this discovery, it has become clear that a thorough understanding of those factors that affect the distribution of ozone is vital. Further comprehensive investigations that compared the results from models and experiments confirmed the presumption of anthropogenic depletion of the ozone layer. In this context, the discovery of the catalytically ozone destructing property of chlorofluorocarbons by Molina and Rowland (1974), is perhaps one of the clearest examples of anthropogenic influence on the atmosphere. This special efforts of Molina were honored officially with the Nobel Prize in 1995, together with J. P. Crutzen, for their pioneer work on stratospheric ozone (Crutzen, 1970).

However, sophisticated measurement techniques are currently routinely applied to retrieve accurate atmospheric parameters in order

to support the endeavor of protecting the atmosphere. In addition to these works, a retrieval technique is introduced here that enhances the capabilities of retrieving ozone concentration profiles from satellite borne limb scatter measurements.

The first ozone observations from ultraviolet scatter measurements in limb viewing mode were made more than twenty years ago when Rusch et al. (1983) used limb radiances around 265 nm and 295 nm to determine ozone concentration profiles. However, there was no documented investigation of the selected wavelengths. Other attempts to use the Hartley bands failed due to the poor data quality (McPeters et al., 2000). While limb observations with satellite borne spectrometers are still novel, although quite common, it remains a challenge to derive reliable ozone profiles; this is the first major objective of the presented thesis.

This thesis also aims to establish applications for the retrieved ozone profiles. The data from the Sciamachy observations enable the global morphology of ozone to be explored, which is a valuable contribution for the investigation of the dynamic and of chemical properties of the upper atmosphere. In particular, global chemical and transport models require initial information. Precise satellite observations will enable more accurate model simulations and tests.

Another application of the retrieved ozone profiles are observations of ozone depletion during solar storms, providing novel insights into atmospheric and extraterrestrial phenomena. This is not only applicable for border tests of present models, measurements, and methodologies, but is also important for our current knowledge of Sun-Earth interactions. Little is known about the properties of solar storms as well as their impact on the Earth's magnetic field and atmospheric chemistry. The impact of solar storms on Earth's life is also a mystery. Solar storms are believed to enhance corrosion, almost completely destroy electronics, and are at least a deadly threat for astronauts.

1.1 Outline of this Thesis

The thesis is structured in three major parts:

Part I describes the required knowledge of the instrument, of the atmospheric chemistry and spectroscopy as well as of the radiative transfer model and of the inversion scheme.

Part II introduces the scientific background to the retrieval. Results of the retrieval are shown, and comprehensive sensitivity and validation studies are presented.

Part III gives a detailed description of two applications; the global morphology of ozone and observations of ozone depletion due to enhanced solar proton precipitation in October and November 2003.

Finally, a conclusion of the presented work is drawn, and an outlook for future investigations is given. The appendix includes a list of abbreviations, the acknowledgments, and the bibliography.

Part I

Fundamentals

2 SCIAMACHY on Envisat

2.1 The Envisat Satellite

The Environmental satellite (Envisat) (ESA, 2005), a joint project of sixteen European member countries of the European Space Agency (ESA), was launched in March 2002 with the ARIANE-5 rocket from Kourou in French Guiana. The total mass of the satellite is 8140 kg and the external dimensions of Envisat are $26\,\text{m} \times 10\,\text{m} \times 5\,\text{m}$ including the solar panels, which provide Envisat with electrical power. The expected lifetime of Envisat is five years. The entire cost of the Envisat project will be about two billion euros over fifteen years.[1] Envisat is therefore both one of the largest satellites and most significant environmental satellite programs to date.

Envisat was injected into a Sun-synchronous polar orbit[2] at an altitude of 799.8 km. The required velocity to stay in the planned altitude is approximately $447\,\text{km}\,\text{min}^{-1}$, this corresponds to about $7\,\text{km}\,\text{s}^{-1}$ over the ground. The Sun-synchronous orbit with an inclination angle[3] of 98.55° has a descending node[4] at about 10:00 a.m. local time (LT). The Sun-synchronous orbit implies almost the same overflight time for the same latitude (for the precise overflight times see Figure 2.1). Each orbit period lasts 100.59 min, and Envisat passes therefore through

---

1 That works out to 7 € per citizen of each ESA member nation, or about one cup of coffee each year of operation.

2 The Sun-synchronous orbit is the orbit where the satellite's orbital plane has a fixed orientation relative to the Sun.

3 The inclination angle is the angle between the equatorial plane and the orbit plane.

4 Descending node means that the equator is crossed southwards by the sub-satellite track.

about fourteen orbits per day. Within six days SCIAMACHY provides
an almost complete global coverage.
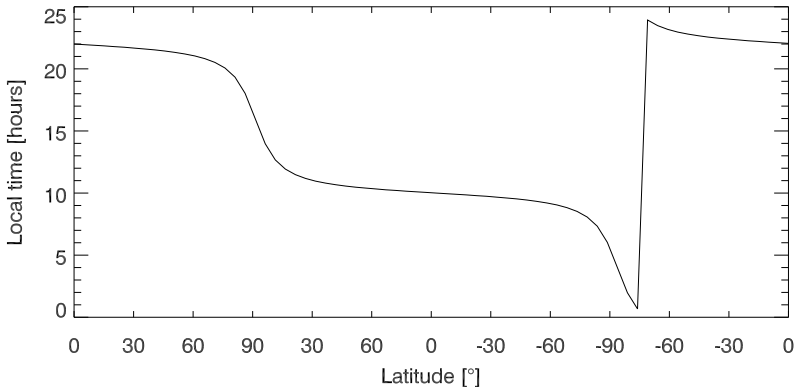
Figure 2.1: SCIAMACHY overflight local times. Courtesy of E. J. Llewellyn

Ten instruments are on board Envisat. Four instruments are mainly
used to monitor the position of the satellite relative to the ground.
These are the Radar Altimeter (RA-2), the MicroWave Radiometer
(MWR), the Doppler Orbitography and Radiopositioning Integrated
by Satellite (DORIS), and the Laser RetroReflector (LRR). The LRR
is a passive device that is used as a reflector by ground-based stations
employing high-power pulsed lasers.

Three instruments monitor the Earth's surface. The Advanced
Synthetic Aperture Radar (ASAR), the MEdium Resolution Imag-
ing Spectrometer (MERIS), and the Advanced Along Track Scanning
Radiometer (AATSR).

Three instruments observe the Earth's atmosphere. The Michel-
son Interferometer for Passive Atmospheric Sounding (MIPAS) (En-
demann and Fischer, 1993; Fischer and Oelhaf, 1996) is a Fourier
transform spectrometer for measurements of highly resolved gaseous
emission spectra in the spectral range from the near to mid-infrared[5].
One of MIPAS's benefit is the high spectral resolution of 0.06 nm,
which makes even weakest emissions resolvable. Since ozone profiles

---

5 MIPAS has a spectral coverage from 4.15 μm to 14.6 μm.

retrieved from MIPAS spectra will later be used for comprehensive validations, a brief description of this instrument is given in Appendix A. The second spectrometer on Envisat, the Global Ozone Monitoring by Occultation of Stars (GOMOS) (Bertaux et al., 1991; ESA, 2001) is also described in Appendix A.

The third spectrometer on Envisat, the SCanning Imaging Absorption spectroMeter of Atmospheric CHartographY (SCIAMACHY) (Burrows et al., 1995; Bovensmann et al., 1999, 2004), is the successor to the Global Ozone Monitoring Experiment (GOME[6]) (Burrows et al., 1999b).

2.2 The SCIAMACHY Instrument

The initial concept of this instrument was presented by Burrows and Chance in 1991, and refined by Goede et al. in 1994. SCIAMACHY (*from Greek*: 'fighting with shadows') is designed to measure radiances[7] in eight channels in a wide spectral range from 214 nm to 2384 nm with a moderate resolution of 0.21 nm to 1.56 nm (see Table 2.1).

Six additional devices measure the polarization of the recorded light through Brewster reflection of a pre-disperse prism. The bands of the polarization measurement devices correspond approximately to the main channels 2 to 6, and to channel 8.

Figure 2.2 shows the two optical banks of SCIAMACHY. For all measurements, the radiation is directed by the elevation mirror onto a telescope with an off-axis parabolic mirror. The telescope focuses the beam onto the entrance slit of the spectrometer. Leaving a pre-dispersing prism, the main beam forms a spectrum in the middle of the instrument. Reflective optics are employed to separate the spectrum into four parts. The shorter wavelength radiation is directed to channel 1 (240 nm to 314 nm) and channel 2 (314 nm to 405 nm). The majority of the spectrum (405 nm to 1750 nm) passes to channels 3 to 6.

---

6 GOME is sometimes called the 'little SCIAMACHY' because it is a side development of SCIAMACHY.

7 Radiance is a measure for the intensity of radiation with dimension $[\mathrm{W\,m^{-2}\,nm^{-1}\,sr^{-1}}]$.

Table 2.1: SCIAMACHY spectral channels and resolution. The table shows also the different detector materials and the temperature to which the detectors are cooled to reduce dark current.

Channel	Range [nm]	Resolution	Material	Temperature [K]
1	214–314	0.21	Si	200
2	309–404	0.22	Si	200
3	392–605	0.47	Si	235
4	598–790	0.42	Si	235
5	776–1056	0.55	Si	235
6	991–1750	1.56	InGaAs	200
7	1940–2040	0.21	InGaAs	150
8	2260–2384	0.24	InGaAs	150
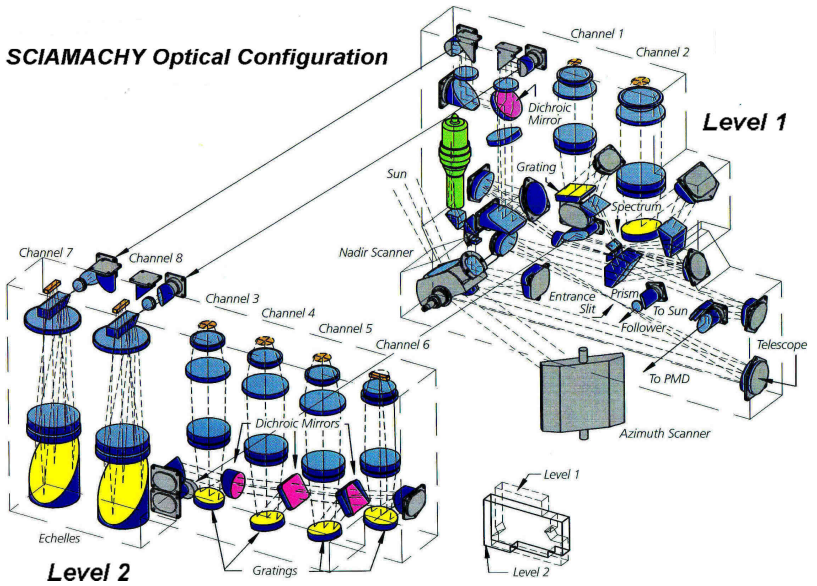
Figure 2.2: Optical banks of SCIAMACHY. Also shown are the paths of the beam to each of the eight channels. The azimuth-scanner is adjusted to the Envisat flight direction. Courtesy of ESA.

The near-infrared part of the spectrum (1940 nm to 2380 nm) is reflected toward channel 7 and 8. Each individual channel comprises a grating and transmission optics, in order to reduce the internally scattered light, as well as a diode array detector.

In channels 1 to 5 the detectors are silicon monolithic diode arrays, whereas InGaAs detectors are used for the near infrared channels. This is due to the large electronic bandgap of silicon ($\sim 1.1\,\mathrm{eV}$) while photons at $2.4\,\mu\mathrm{m}$ have an energy of $0.5\,\mathrm{eV}$. To reduce the dark current and detector noise, the diode arrays are cooled to between $150\,\mathrm{K}$ to $200\,\mathrm{K}$, and the entire instrument is cooled to $253\,\mathrm{K}$. The cooling is provided by a simple passive radiator mounted on top of the instrument.

Several calibration facilities exist on board Sciamachy. A NePtCr hollow cathode discharge lamp emits narrow spectral lines, these lines are used for spectral calibration. A 5 W Tungsten halogen white lamp is used to monitor pixel-to-pixel gain differences and long-term degradation. Two sand blasted aluminum diffuser plates are mounted on the back of the scan mirrors to enable measurements of the Sun's irradiance.

It is apparent that Sciamachy is able to record spectra over a wide spectral range. This allows different trace gases to be retrieved simultaneously (see Figure 2.3 for the list of molecules).

2.3 Limb Observation Geometry

A novelty of Sciamachy are the three different observation geometries. Each geometry has its own particular advantage with respect to vertical altitude resolution and spatial coverage.

In nadir mode (Buchwitz et al., 2005), air masses directly below the satellite are observed (see Figure 2.4). The nadir mirror scans across the satellite track with a field of view of $25\,\mathrm{km} \times 0.6\,\mathrm{km}$. The spatial resolution in the nadir scan mode depends on the scan velocity and the integration time of the detectors. The scan velocity along track is determined by the spacecraft velocity, and the across track velocity is determined by the nadir scan mirror rate, approximately $240\,\mathrm{km\,s^{-1}}$
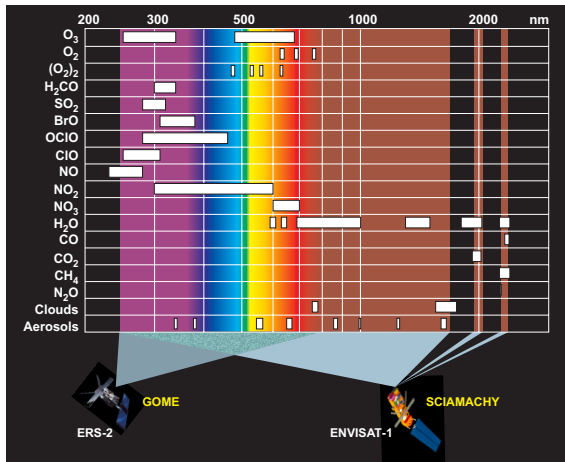
Figure 2.3: Spectral coverage of SCIAMACHY and its predecessor GOME. Also depicted are the spectral ranges where the atmospheric parameter has to be explored for retrievals. Courtesy of S. Noël.
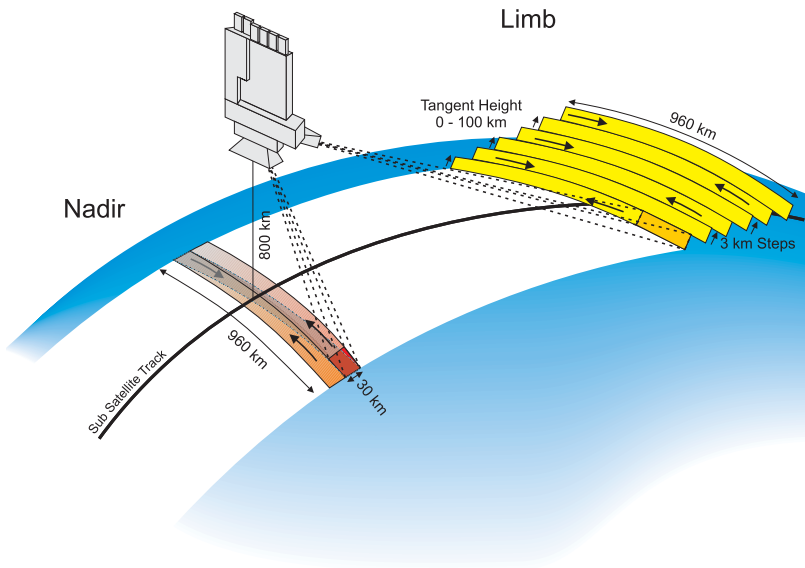
Figure 2.4: Nadir and limb geometry at SCIAMACHY measurements. Courtesy of S. Noël.

over the ground. Thus the typical spatial resolution is approximately 240 km across track and 30 km along track. Nadir measurements therefore provide relatively good spatial resolution.

In occultation mode[8], SCIAMACHY looks directly at the Sun or the Moon. Occultation measurements are made only during orbital sunrise, or when the Moon is visible, and thus global coverage is not obtained. The instrument tracks the Sun actively during sunrise and tracks the Moon from half Moon to full Moon at a fixed azimuth mirror position. The field of view is about 30 km in azimuthal and about 2.5 km in elevation at the tangent point. The spatial resolution depends on the integration time, 62 ms for solar occultation measurements and about 1 s for lunar measurements, and is thus approximately 30 km × 2.5 km at the tangent point. Due to the high intensity of the Sun and the Moon, occultation measurements are very accurate.

In limb mode, SCIAMACHY scans the limb of the Earth from the surface up to 92 km (Figure 2.4).[9] The field of view is 110 km × 2.6 km at the tangent point, but due to the integration time of 0.375 s, the spatial resolution is expanded to about 240 km across track and along track about 500 km horizontally and 3 km vertically. Each horizontal scan can be divided into separate measurements. For instance, in channel 1, the horizontal scan can consist of four measurements each with an integration time of 0.375 s. The across track azimuthal coverage is therefore about 960 km at the tangent point in this case.

After one horizontal scan the elevation mirror performs a vertical step of about 3.3 km at the tangent point, this takes 150 ms. During an entire vertical scan which includes measurements at 31 different tangent heights and lasts 60 s, the spacecraft moves approximately 460 km in along-track direction thus the tangent point also moves during the complete measurement. In contrast to that, the location

_____

8 See also the spectrometer in occultation mode, Halogen Occultation Experiment (HALOE) on the Upper Atmospheric Research Satellite (UARS) (Russell et al., 1993), and the description profile retrieval from SCIAMACHY occultation measurements (Meyer et al., 2005).

9 During the first two years of the mission, the top tangent height was set to approximately 105 km.

of the respective tangent point moves in the opposite direction due to the sphericity of the Earth and the scan and look direction.

A typical orbit starts with four limb measurements in twilight, followed by the solar occultation measurement during sunrise in the northern hemisphere, and an optimized limb-nadir sequence (see Figure 2.5). This sequence requires the synchronization of integration times, scan ranges, and viewing directions for all limb and nadir measurements. Through this technique, precise observations of the troposphere can also be made. When the Moon is visible in the southern hemisphere, lunar occultation measurements are performed every second orbit. In addition to the atmospheric measurements, calibration measurements are performed on a regular basis during eclipse periods (for details of the calibration measurements see Frerick et al., 1997). Figure 2.6 shows a typical Sciamachy orbit on 29 July 2004.
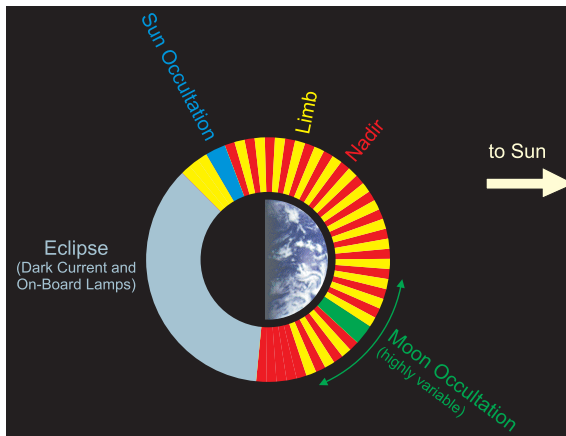
Figure 2.5: Sciamachy measurement sequence along one orbit

At the present time O_3 (von Savigny et al., 2005b; Rohen et al., 2006), BrO, NO_2, and OClO (Rozanov et al., 2005) have all been retrieved successfully from limb scatter measurements.

Finally, Table 2.2 gives an overview of Envisat's and Sciamachy's properties.

SCIAMACHY Swath Geolocation Display for Limb in Orbit 12612
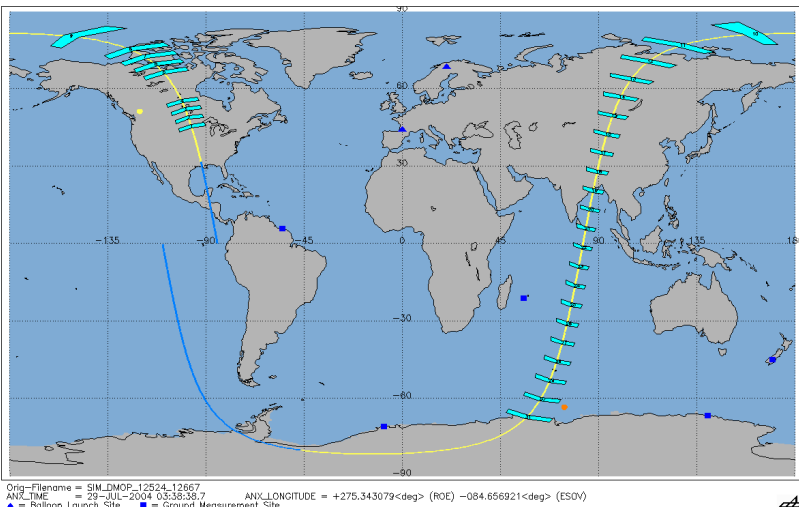
Figure 2.6: Sciamachy orbit on 29 July 2004. The rectangles along this orbit indicate the area of a Sciamachy limb measurement. The yellow circle above Western Canada marks the location of the satellite during the solar occultation measurement, and the orange point marks its location during the lunar occultation measurement over Antarctica. Figure courtesy of the German Aerospace Center (Dlr).

Table 2.2: Some properties of Envisat and Sciamachy

Launch	March 1, 2002 02:07:58 Cet from Kourou, French Guiana
Orbit	Sun-synchronous polar orbit
Altitude	799.8 km
Inclination angle	98.55°
Equator crossing time	About 10:00 a.m. Lt descending node
Orbit period	100.59 min
Repeat cycle	35 days
Field of view	Azimuthal 110 km, elevation 2.6 km
Coverage	Azimuthal 960 km, elevation 0 km to 92 km

3 Ozone Chemistry and Spectroscopy

It is not the aim of this chapter to review the entirety of atmospheric chemistry and spectroscopy. Rather, a scientific background is presented. This is required to classify the profile retrieval in contrast to other methodologies and to discuss its advantages, disadvantages, and possibilities. The chemistry of atmospheric ozone is therefore described only briefly. In addition, a short historical overview of ozone observations and related retrieval techniques are presented in this chapter. Atmospheric spectroscopy is treated as it indicates the possibilities for further ozone concentration retrievals from SCIAMACHY limb spectra and for geophysical applications. For the nomenclature and the basic scientific background perusal of the common literature is recommended (Herzberg, 1950; Brasseur and Solomon, 1984; Wayne, 1985).

3.1 Stratospheric Ozone Chemistry

The first explanation of the stratospheric ozone layer was given by Chapman (1930). He suggested the reaction cycle, which is now known as the Chapman cycle:

$$O_2 + h\nu \quad \rightarrow \quad O + O \tag{3.1}$$

$$O + O_2 + M \quad \rightarrow \quad O_3 + M \tag{3.2}$$

$$O_3 + h\nu \quad \rightarrow \quad O + O_2 \tag{3.3}$$

$$O + O_3 \quad \rightarrow \quad 2\,O_2 \tag{3.4}$$

$$O + O + M \quad \rightarrow \quad O_2 + M\,. \tag{3.5}$$
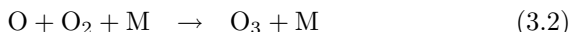
Ozone is produced through the photolysis of O_2 by ultraviolet radiation (3.1) and the subsequent recombination of O and O_2 (3.2). M is a collision partner that is necessary for energy and momentum conservation. Collision partners are most probably nitrogen or oxygen molecules, since they are the most abundant in the atmosphere. Destruction of ozone molecules is only possible through photolysis (3.3) and odd oxygen[1] recombination.

Three body recombination (3.2) and ozone photolysis (3.3) cause a rapid adjustment of the photochemical equilibrium between O and O_3. The production rate of O_3 depends on the O_2 concentration and on the incident solar radiation. The molecular oxygen concentration decreases with increasing altitude, whereas the ultraviolet radiation increases strongly. Hence, the ozone concentration has its maximum in the middle atmosphere.

Catalytic Cycles

First measurements indicated that the altitude of the ozone layer predicted by the Chapman cycle was too high. A catalytic ozone destruction process was suggested by Bates and Nicolet (1950), it is based on the reaction of ozone and HO_x[2]. Other atmospheric trace gases have been identified as being involved in catalytic reactions: NO_x[3], for instance, was found to be conserved in the stratosphere (Crutzen et al., 1975). A chlorine catalytic cycle[4] (Stolarski and Cicerone, 1974) and a bromine related catalytic cycle (Wofsy et al., 1975) have also been suggested. Additionally, the conservation of catalysts and the release of catalytic radicals through photolysis of the reservoir of atmospheric chlorofluorocarbons was discovered, these enhance the long-term catalytic effects (Molina and Rowland, 1974).

---

1 The sum of O and O_3 concentrations is often referred to as 'odd oxygen' in the literature. This family concept is used because of the rapid interconversion of O and O_3.

2 HO_x denotes H, OH, and HO_2.

3 NO_x denotes NO, and NO_2.

4 These chlorine related catalytic cycles are called ClO_x cycles.

A general catalytic scheme can be described as:

$$X + O_3 \quad \rightarrow \quad XO + O_2 \,, \qquad (3.6)$$

$$XO + O \quad \rightarrow \quad X + O_2 \,, \qquad (3.7)$$

$$\text{Net: } O + O_3 \quad \rightarrow \quad 2\,O_2 \qquad (3.8)$$
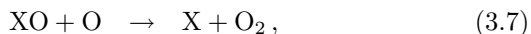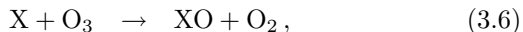
where X denotes the potential catalysts OH, H, NO, Cl or Br. Since the catalysts are not consumed, they are capable of completing the cycle thousands of times. The scheme is only truncated through reactions, that transfer X into a non-catalytic compound.

3.2 Lower Mesospheric Ozone Chemistry

Figure 3.1 shows the fractional contributions of the odd oxygen loss due to the Chapman reactions and the catalytic reactions, (Wmo, 1986). The Chapman and the ClO_x catalytic cycles have their largest impact between $40\,km$ and $50\,km$, but even here, HO_x and NO_x induced depletion of odd oxygen is of the same order of magnitude.
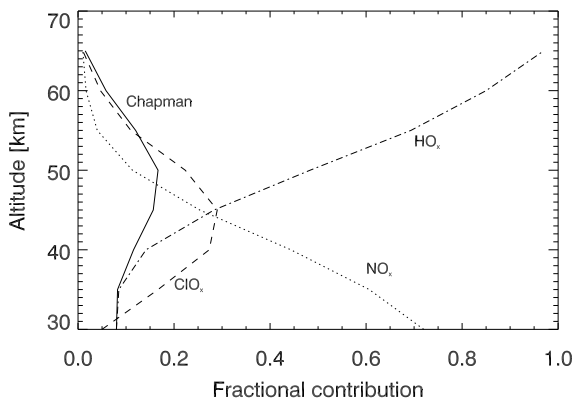
Figure 3.1: Fraction of the odd oxygen loss rate due to ozone reaction mechanisms (Wmo, 1986).

At higher altitudes, NO_x is quickly photolyzed or is lost through reaction with atomic nitrogen. Since the required short-wave radiation is already absorbed, NO_x at lower layers is protected against dissociative radiation. Additionally, the main source of NO_x, N_2O, is rare or is rapidly photolyzed to $O(^1D)$ and N_2. In contrast, the HO_x catalytic cycle becomes important at higher altitudes since HO_x is produced through reaction of CH_4 and H_2O with exited oxygen. The concentration of $O(^1D)$ as well as that of OH increases with altitude due to stronger photolysis. Additionally, the activation energies for the catalytic cycle processes are small and so almost temperature-independent, in contrast to the Chapman cycle reactions.[5] In sum, the impact of the HO_x catalytic cycle increases in the upper atmosphere and dominates the ozone chemistry.

While the diurnal variability of stratospheric ozone is negligible, ozone concentrations at, e.g., 70 km are up to 90 % smaller in the daytime than at night (see Figure 3.2).
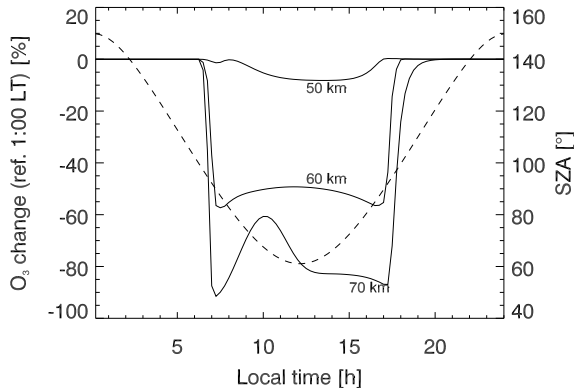
Figure 3.2: Single Layer Isentropic Model of Chemistry And Transport (SLIMCAT) (Chipperfield et al., 1996) three dimensional atmospheric chemical transport model simulation of the diurnal variability of ozone concentrations at 50 km, 60 km, and 70 km on 11 August 2002. Also shown is the solar zenith angle as a function of the local time. Data courtesy of M. Sinnhuber.

_____

5 The temperatures in the mesosphere decrease drastically towards higher altitudes.

The reason for this decrease and its difference in the mesosphere and stratosphere is due to effects of photolysis.

3.3 Spectroscopy of Ozone

The spectroscopy of the ozone molecule is quite complicated with many remaining puzzles as the effect of the multiple isomers and symmetries of the O_3 molecule (see Steinfeld et al., 1987, for a review of ozone spectroscopy). Since the quantum mechanical states of the products of the photodissociation of molecular oxygen (3.1) are well known, the exact threshold energies for the production of atomic and molecular oxygen are also known. The possible initial and final electronic states of oxygen are shown in the potential curve diagram Figure 3.3.
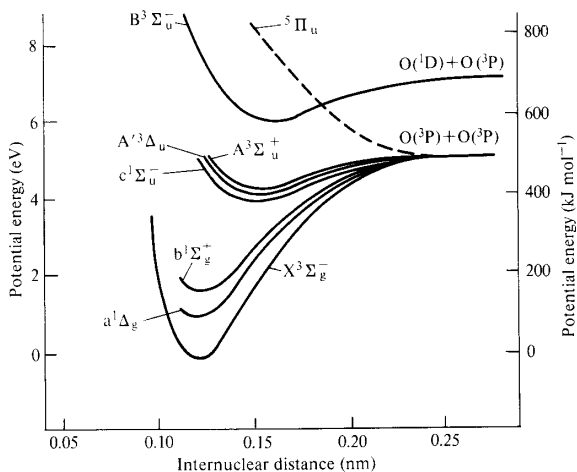
Figure 3.3: Potential energy curves for the ground state and several electronically excited states of molecular oxygen. The ground state is labeled X. A, B, C, ... denote the electronic states of same spin multiplicity, lower case letters denote electronic states with different spin multiplicity. The Greek capitals express the angular momentum. Vibrational and rotational states are not shown. Figure taken from Wayne (1987).

Table 3.1 indicates the wavelength thresholds for different products in ozone photolysis.

Table 3.1: Theoretical wavelength thresholds for different products of ozone photolysis (Baulch et al., 1980; Moore, 1971). Wavelengths are expressed as [nm].

	$O_2(X^3\Sigma_g^-)$	$O_2(^1\Delta_g)$	$O_2(b^1\Sigma_g^+)$	$O_2(A^3\Sigma_u^+)$	$O_2(X^3\Sigma_g^-)$
$O(^3P)$	1180	590	460	230	170
$O(^1D)$	410	310	260	167	150
$O(^1S)$	234	196	179	129	108

Considering the spin conservation, only ozone photodissociation with the same multiplicity are likely. The lowest energy singlet pair is $O(^1D)$ and $O_2(a^1\Delta_g)$, and the corresponding threshold wavelength 310 nm. For triplet states, the wavelengths have to be shorter than 1180 nm.

A transition between two states is caused by the absorption or emission of radiation, or collisional quenching. In the lower atmosphere, collisional quenching is more likely than in the mesosphere. At higher altitudes, the number of collisions decreases, and high intensity radiation from the Sun excites the atmospheric constituents which then emit radiation either by spontaneous or induced emission. Emissions are therefore generally more clearly observable in the upper atmosphere.

A prominent example of a strong emission and absorption feature in the atmosphere is the electronic transition $O_2(a^1\Delta_g \rightarrow X^3\Sigma_g^-)$ with a corresponding wavelength band at 1.27 μm, called the 'Infrared Atmospheric' band. Although the Infrared Atmospheric band transitions are strictly forbidden,[6] they are one of the strongest features in the atmospheric spectrum. A Sciamachy spectrum in this band is shown in Figure 3.4, where absorption at lower altitudes as well as emission at higher altitudes is observable.

The Infrared Atmospheric band corresponds to rotational transi-

---

6 Electric dipole rules, including the multiplicity, the total angular momentum, as well as the non-changing parity, are all broken!
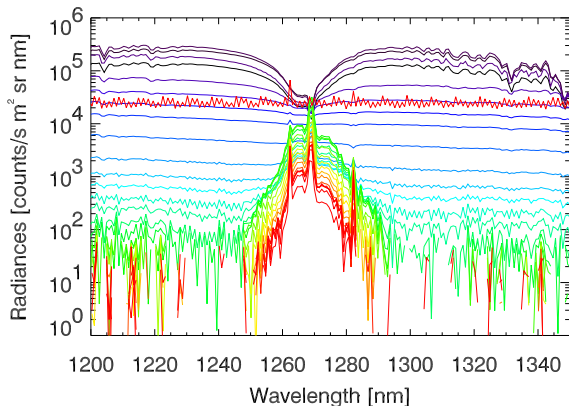
Figure 3.4: SCIAMACHY spectra of $O_2(a^1\Delta_g \rightarrow X^3\Sigma_g^-)$ at $1.27\,\mu m$ from the surface (top spectra) to about $100\,km$ (the bottom spectra). Absorption features are observable in the lower atmosphere, and emission features are observable in the upper atmosphere. The jagged line is a dark current calibration measurement.

tions between the vibrational states $\nu' = 0$ and $\nu'' = 0$.[7] Another intense emission is caused by the $(0, 1)$ transition band around $1.58\,\mu m$.[8]

3.4 Ozone Absorption Cross Sections

The absorption cross sections are a measure of the absorption of radiation at a specific wavelength.

Figure 3.5 shows the GOME flight model (FM) absorption cross sections of ozone in the ultraviolet and visible wavelength range for differ-

---

7 The transition between the vibrational states will be denoted as $(0, 0)$, where the first number corresponds to the higher vibrational state ν'.

8 While the absorption by the $(0, 0)$ transitions is quite strong in the lower atmosphere, the emission lines caused by the $(0, 1)$ transitions are not absorbed because the population in $\nu'' = 1$ is negligible. The $(0, 0)$ caused spectral feature is therefore only detectable by balloons, airplanes and satellites, in contrast to that feature caused by $(0, 1)$ transitions, which is observable by ground-based instruments.
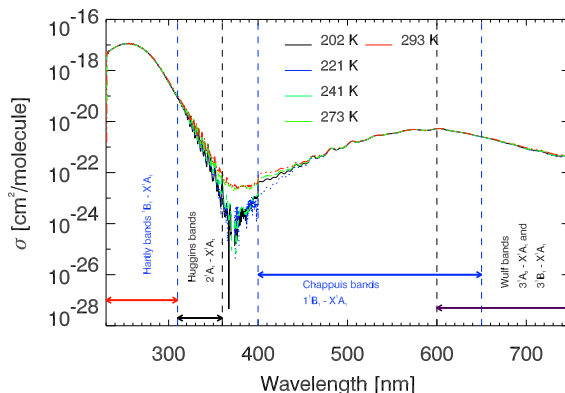
Figure 3.5: Gome Fm absorption cross sections in the ultraviolet and visible spectral range for different temperatures (Burrows et al., 1999a). Basically, the Wulf bands range up to 1000 nm.

ent temperatures. The absorption spectrum is commonly divided into four different absorption bands, but the boundaries are still disputed.

The Wulf bands from 650 nm to about 1000 nm are believed to be caused by the $3\,A_2 \leftarrow X^1A_1$ and the $3\,B_2 \leftarrow X^1A_1$ transitions (Steinfeld et al., 1987).[9]

The Chappuis absorption bands cover the 400 nm to 650 nm range with a maximum absorption cross section at 602.5 nm (Anderson and Mauersberger, 1992). The system corresponds to transitions from the X^1A_1 ground state to the $^1A_2$ and $^1B_1$ states in the $C_{2\nu}$ symmetry. Around the maxima, the cross sections are more temperature-independent, but towards the Huggins bands, they become highly temperature-dependent. Here, they display an oscillating curve shape. Thus, measurements of the cross sections in these spectral range have large uncertainties. The Huggins bands are caused by the $2^1A_1 \leftarrow X^1A_1$ transitions (Steinfeld et al., 1987).

The Hartley bands cover the 200 nm to 310 nm region and consist of a broad continuum with small diffuse overlying structures. They corre-

---

9 The first capitals (here X, 1, 2, . . .) denote the electronic states, and the second capital labels the symmetry race for the ozone molecule, whose symmetry is characterized by the $C_{2\nu}$ and C_s point groups.

spond to the $^1B_2 \leftarrow X^1B_1$ transitions of the ozone molecule. The cross sections peak at 255 nm, and are almost temperature-independent. For a change in temperature from 218 K to 295 K, the cross sections differ by about 1 % (Johnson and Kinsey, 1989).

Figure 3.6 shows absorption cross sections measured with the Gome (Burrows et al., 1999a) and Sciamachy Fm (Bogumil et al., 2003).
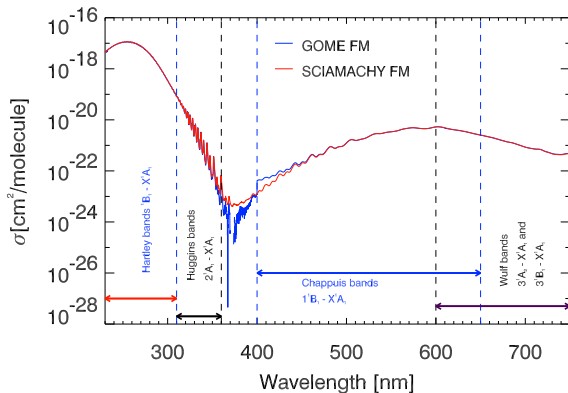
Figure 3.6: Absorption cross sections of ozone at 202 K measured by the Gome Fm (Burrows et al., 1999a) and Sciamachy Fm (Bogumil et al., 2003). They show large differences in the boundary region from the Huggins to the Chappuis bands.

The errors in the cross sections from Sciamachy Fm are specified by 2 % in the ultraviolet, but increase towards longer wavelengths. The uncertain cross sections in the temperature-dependent Huggins bands are usually avoided for ozone concentration measurements. Figure 3.7 shows the deviations of the Gome and Sciamachy Fm cross sections in the Hartley-Huggins bands. The differences reach only 3 %.[10]

For the retrieval presented in this thesis, Gome Fm cross sections have been applied. Retrievals with the Sciamachy Fm cross sections must be done in the future.

---

10 Comprehensive investigations of the deviations between Gome and Sciamachy Fm have been recently published by Orphal (2002).
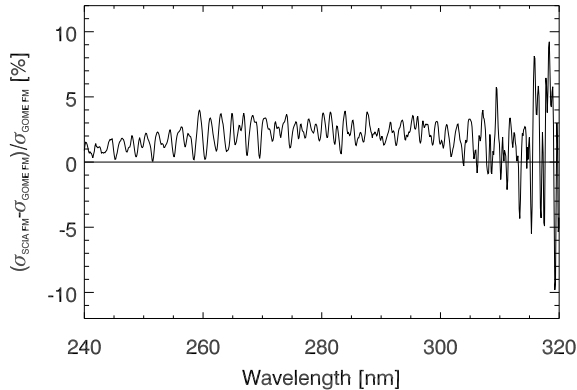
Figure 3.7: Differences of Sciamachy and Gome Fm absorption cross sections in the Hartley-Huggins bands at 202 K. In the Hartley bands deviations reach only 3 %.

3.5 Techniques to Retrieve Ozone Profiles

Although the first spectroscopic detection of atmospheric ozone occurred in the early 1880s (Chappuis, 1880), it was not until 1920 that quantitative ozone retrievals became possible. Fabry and Buisson (1921), who have since then been deemed the discoverers of the ozone layer, reported the determination of ozone from measurements in the Hartley-Huggins bands. Due to uncertain inversion methods[11] measurements at that time were in conflict with the theoretical work of Chapman (1929, 1930), who predicted an ozone layer lower than the measured 45 km. In the early 1930s the 'Umkehr'-method was refined and the altitude of the ozone maximum was found to be near 25 km, in better agreement with Chapman's predictions (Götz et al., 1934). After the Second World War, several measurement techniques were used to retrieve ozone concentrations. Beside various balloon-based ozonesondes, sophisticated rocket-borne spectrometers, ground-based, air-borne, and Space Shuttle borne instruments, satellites became im-

---

11 At that time inversion was called the 'Umkehr'-method. 'Inversion' denotes the inversion of a measurand to the wanted measure, here ozone concentrations.

portant for their global coverage, the long lifetime of the instruments, and the quality of the measurements.[12]

3.5.1 Emission Spectroscopy

The most common technique for mesospheric ozone profile retrievals uses molecular oxygen emissions, which arise in part from photolysis of ozone. Some of the prominent employed transitions are listed in Table 3.2. Each band has its own advantage. For instance, the

Table 3.2: Emissions in the visible and near infrared employed for upper atmospheric ozone profile retrievals.

Transition	Wavelength [μm]	Sample Publications
$O_2(b^1\Sigma_g^+ \rightarrow X^3\Sigma_g^-)\,(0,0)$	0.76	López-Gonzáles et al. (1992)
$O_2(b^1\Sigma_g^+ \rightarrow X^3\Sigma_g^-)\,(0,1)$	0.86	Noxon (1975)
$O_2(a^1\Delta_g \rightarrow X^3\Sigma_g^-)\,(0,0)$	1.27	Thomas et al. (1983)
$O_2(a^1\Delta_g \rightarrow X^3\Sigma_g^-)\,(0,1)$	1.58	Winick et al. (1985)

$O_2(a^1\Delta_g \rightarrow X^3\Sigma_g^-)\,(0,1)$ band at $1.58\,\mu m$ is easily modeled, but accurate measurements are difficult. In contrast, emissions from the $(0,0)$ Infrared Atmospheric band are quite difficult to model. An accurate determination of the population of the quantum mechanical states following the non-local thermodynamic equilibrium statistics is required, and the intensity and broadening of the particular emission lines cannot be derived by simple Boltzmann statistics.[13]

Emissions in the infrared and microwave region have also been used to infer ozone densities in the mesosphere from measurements with ground-based, (e.g., Wilson and Schwartz, 1981) and space borne in-

---

12 See the references as examples of the respective instrument bases (Hilsenrath, 1971; Friedl-Vallon et al., 2004; van Allen and Hopfield, 1948; Llewellyn and Witt, 1977; Evans and Llewellyn, 1970; Bremer et al., 2002; McPeters et al., 2000). A comprehensive review of satellite borne ozone measurements can be found in Krüger et al. (1980); Miller (1989).

13 An example of ozone profile retrievals in the Infrared Atmospheric band are Cryogenic Infrared Spectrometers and Telescopes for the Atmosphere (Crista) ozone retrievals (Kaufmann et al., 2003).

struments, e.g., the Microwave Limb Sounder (Mls) on the Upper Atmosphere Research Satellite (Uars) (Froidevaux, 1996). Even a rocket-borne mass spectrometer was used to determine the ozone concentrations (Trinks, 1975). For a comprehensive review of the common retrieval methods used for ozone retrievals from satellite data since 1980 see Miller (1989).

3.5.2 Absorption Spectroscopy

The common technique used to infer ozone densities at lower altitudes in the atmosphere is ultraviolet and visible absorption spectroscopy with the Sun, the Moon, or stars as sources of radiation. Currently the only published ozone profile retrievals from ultraviolet backscatter limb measurements are those from data from the Solar Mesosphere Explorer (Sme) (Thomas et al., 1983), from the Shuttle Ozone Limb Sounding Experiment (Solse) (McPeters et al., 2000), and from Sciamachy limb measurements (Rohen et al., 2005).

3.6 Earlier Investigations

3.6.1 Solar Mesosphere Explorer

Sme was the first space borne spectrometer operating in limb mode (Rusch et al., 1983; Thomas et al., 1983). Its operation period lasted from December 1981 to December 1989. The Sme spacecraft was placed into a circular Sun-synchronous orbit with an inclination angle of $97.8°$ at an altitude of $600\,km$. The equator crossing time was at about $15{:}00\,Lt$ on the day-side and at about $3{:}00\,Lt$ on the nightside. Sme measured the scattered limb radiances at tangent heights from $20\,km$ to $120\,km$ in $3.5\,km$ steps. The National Aeronautics and Space Administration (Nasa) satellite was designed to study the upper part of the Earth's ozone layer, its response to changes in solar activity and its relationship to the meteorology of the stratosphere and mesosphere.

The five instruments on board Sme were the 'ultraviolet ozone spec-

trometer' (0.2 μm to 0.33 μm), the 'visible NO_2 and airglow spectrometer' (0.295 μm to 0.59 μm), the 'near infrared airglow instrument' (0.6 μm to 2.0 μm), the 'solar ultraviolet spectrometer' (0.12 μm to 0.31 μm), and the 'four-channel spectrometer' (four channels in the far infrared). Important wavelength ranges for these instruments were taken into account, such as the hydrogen Lyman-α (0.1216 μm), the ozone Hartley bands from 250 nm to 320 nm, the near infrared emission at 1.27 μm, and several channels to measure water vapor, NO_2 and airglow emissions[14] in the near infrared. Atmospheric temperatures, O_3, and NO_2 profiles in the upper atmosphere have been successfully retrieved (Thomas et al., 1980). Ozone profiles have been retrieved from both the ultraviolet absorption (Rusch et al., 1984) as well as the $O_2(a^1\Delta_g \rightarrow X^3\Sigma_g^-)$ emissions (Thomas et al., 1983). In terms of the backscattered radiance inversions, they used the 265.0 nm and 296.4 nm radiances to derive ozone profiles over an altitude range between 50 km and 70 km. Unfortunately, no details of the sensitivity of their inversion algorithm nor of their selection of wavelengths have ever been published. It is doubtful that their inversion scheme had good sensitivity above 60 km.[15]

The ozone profile retrievals from the $O_2(a^1\Delta_g \rightarrow X^3\Sigma_g^-)$ emissions had an altitude coverage from 50 km to 90 km (Thomas et al., 1983).

3.6.2 Shuttle Ozone Limb Sounder Experiment and Limb Ozone Retrieval Experiment

The instrument pair SOLSE/LORE was flown by NASA as a proof-of-concept mission on a Space Shuttle in December 1997 and January 2003. It operated in the 260 nm to 350 nm spectral region with a resolution of 0.5 nm, and also included filters at 345, 525, 603, 677, and 1000 nm. For ozone profile retrievals eleven discrete wavelengths in the Huggins bands above 310 nm have been used (McPeters et al.,

---

14 Air-glow is caused by Sun-driven excitations of meta-stable species.

15 It will be shown later that the 265.0 nm radiances show only a small sensitivity above 60 km and that they have only been in part an applicable choice due to disturbing emissions from NO.

2000). This was more of a compromise, because the limb radiances below 310 nm had not been accurately detected due to the low absolute intensity. Several ozone profiles between 15 km and 50 km altitude from Solse/Lore's measurements have been retrieved and validated successfully (McPeters et al., 2000). In order to compensate for multiplicative noise and error effects, all radiances are divided by those at a reference tangent height and are used in pairs or triplets of strong and weak ozone absorptions (Flittner et al., 2000). This normalization technique will also be employed in the inversion presented in this thesis.

4 Radiative Transfer

In this chapter the radiative transfer model SCIARAYS is introduced. This module is used for the inversion of the radiance profiles as measured by SCIAMACHY in limb geometry to an ozone concentration profile. In this context the main physical processes implemented in SCIARAYS are explained, especially the Rayleigh scattering. A more detailed description of SCIARAYS can be found in Kaiser (2001).

4.1 Physical Processes in the Atmosphere

4.1.1 Rayleigh Scattering

Atmospheric scattering was already investigated and documented during the 15th century by Leonardo da Vinci and later by Isaac Newton (Richter, 1970). Elastic scattering of light by molecules or particles, whose size is small compared to the incident wavelength, is called Rayleigh scattering. Sometimes Rayleigh scattering is also called molecular scattering or Cabannes scattering, in honor of Lord Rayleigh's student, Jean Cabannes. In contrast to inelastic Raman scattering, the wavelengths of the incident and the scattered light are the same for Rayleigh scattering. The incident and scattered radiation is not phase-correlated. The intensity as well as the angular distribution of the scattered light can be derived accurately (Strutt, 1871)[1]. The radiation is scattered in all directions, but the main contribution of the radiation is scattered in direction of the incident photons and in the opposite direction. The rotational Raman cross sections in the ultraviolet correspond to only a few percent of the Rayleigh cross sec-

---

1 John William Strutt, who became later Lord Rayleigh.

tions in the atmosphere. The contribution of Raman scattering to the total radiance at $310\,\mathrm{nm}$ measured by the Solar Backscatter Ultra-Violet (Sbuv) satellite (Fleig et al., 1990) in related models has been estimated at less than $2\,\%$ thus the impact of Raman scattering to retrievals of ozone profiles from backscatter limb measurements has been viewed as negligible (Joiner et al., 1995).

The Rayleigh scattering cross sections of a species X are given by

$$\sigma_r(X) = \frac{8\pi^3}{3N_\mathrm{A}^2} \frac{\left(n^2(X) - 1\right)^2}{\lambda^4} F_\mathrm{King}(X) \tag{4.1}$$

(Dalgarno and Williams, 1962). N_A is the Avogadro number, and $n(X)$ is the refractive index of species X. The λ^{-4} dependence expresses the strongly increasing intensity of the Rayleigh scattered light with decreasing wavelength, which is the cause for the blue color of the atmosphere during the day. The King factor F_King is expressed as a function of the empirical depolarization factor $d(X)$ of species X (King, 1923)

$$F_\mathrm{King}(X) = \frac{6 + 3\,d(X)}{6 - 7\,d(X)}\,. \tag{4.2}$$

An effective King factor $F_\mathrm{King}^\mathrm{air}$ for the atmospheric air composition can either be calculated by interpolating tabulated values (e.g., Bates, 1984) or by evaluating Equation (4.2) (Young, 1980). For calculations in Sciarays a dimensionless value of $d = 0.0295$ is used. Sometimes expression (4.1) is additionally modified by an approximation for the refractive index

$$n^2 - 1 \approx 2\,(n - 1) \tag{4.3}$$

which is valid for $n \approx 1$. Sciarays eventually derives the intensity of the Rayleigh scattering by an approximating formula (Rozanov et al., 1997),

$$\sigma_r = \frac{32\pi^3}{3} \left(\frac{n - 1}{N_\mathrm{A}}\right)^2 \frac{F_\mathrm{King}^\mathrm{air}}{\lambda^4}. \tag{4.4}$$

The Rayleigh scattering coefficient Ξ_r is obtained by multiplication

of σ_r with the neutral molecule number density ρ,

$$\Xi_r = \sigma_r\,\rho \tag{4.5}$$

and

$$\rho = \frac{p}{k_{\mathrm{B}}\,T}\,, \tag{4.6}$$

where p is the pressure, T the temperature, and k_{B} the Boltzmann constant. The total scattering coefficient $\sigma(\vec{r})$ is the sum of the scattering coefficients of all scattering processes i,

$$\sigma(\vec{r}) = \sum_i \sigma_i(\vec{r})\,. \tag{4.7}$$

The angular distribution of the scattered light is described by the Rayleigh scattering phase function (Lenoble, 1993)

$$\Phi(\gamma) = \frac{3}{8\pi}\frac{1}{2+d}\left((1-d)+(1-d)\cos^2\gamma\right) \tag{4.8}$$

where γ is the angle of the scattered photon with respect to the direction of the incident photon. The phase functions can be normalized to unity

$$\oint \Phi(\vec{r},\gamma)\,\mathrm{d}\gamma = 1\,. \tag{4.9}$$

The absorption by atoms and molecules is strongly wavelength dependent and varies with temperature and pressure. Molecular absorption cross sections are available from many calculated and measured databases.

4.1.2 Aerosol Extinction

Aerosols scatter and absorb light too, with the scattering usually approximated by the Mie theory. Extinction coefficients and angular distributions are deduced in Appendix B. We will later show in Section 7.3 that scattering from aerosols has a negligible contribution to the measurements in the upper atmosphere. This is due to their very small abundance in the upper stratosphere and lower mesosphere.

4.1.3 Surface Reflection

In addition to the scattering by gases and aerosols, surface reflection must also be considered in the radiative transfer, especially for lower atmospheric layers and for wavelengths greater than 310 nm.

Surface reflection is expressed through the albedo A, which is defined as the fraction of the reflected to the incident radiative flux. In SCIARAYS, Lambertian surface reflection with isotropic redistribution of the reflected light is assumed. It will be shown later that in the lower mesosphere the radiation in the ultraviolet has almost no contributions from ground reflections.

4.1.4 Refraction

The refractive index n in the expression for of the Rayleigh scattering cross sections (4.4) depends on the temperature T, pressure p, and wavelength λ. Refraction causes changes in the path lengths as derived by SCIARAYS.

The atmospheric refractive index n is usually derived with an approximative formula (Edlén, 1966),

$$(n - 1) \times 10^{-8} = \frac{0.00138823 \times p}{1 + 0.003671 \times T} \times 8342.13$$
$$+ \frac{2406030}{130 - \lambda^{-2}} + \frac{15997}{38.9 - \lambda^{-2}} \quad (4.10)$$

where λ is in micrometers. Updates to this formula have been given (Peck and Reeder, 1972), but the differences from the original formula (4.10) are quite small. Since the differences of tabulated values from Equation (4.10) are quite small, too, empirically determined refractive indices are read from tables (Bates, 1984).

4.2 Radiative Transfer Equation

The radiative transfer equation is the atmospheric radiation equation of motion that has to be fulfilled by every solution of an inversion. The general form of the atmospheric radiative transfer equation is

$$\frac{\mathrm{d}R_\lambda(s,\Omega)}{\mathrm{d}s} = \kappa(s)\left(J_\lambda(s,\Omega) - R_\lambda\right). \tag{4.11}$$

s is the path coordinate. $R_\lambda(s,\Omega)$ is the specific radiance, i.e., the energy flux per unit area, per unit solid angle and per unit wavelength interval through an area located at $\vec{r}$, and oriented perpendicularly to the direction Ω. $\kappa(s)$ is the extinction coefficient for all scattering and absorption processes.

$J_\lambda(s,\Omega)$ is the so called source function that expresses the additional radiation due to scattering and emission processes, as well as solar illumination,

$$J_\lambda(s,\Omega) = \frac{\omega_0}{4\pi} \oint \Phi(\vec{r},\Omega,\Omega')\, R_\lambda(\vec{r},\Omega')\, \mathrm{d}\Omega'$$
$$+ \frac{\omega_0}{4\pi}\, I_0\, \Phi(\vec{r},\Omega,\Omega')\, \mathrm{e}^{-\tau(s)}. \tag{4.12}$$

ω_0 is the single scattering albedo

$$\omega_0 = \frac{\sigma(\vec{r})}{\kappa(\vec{r})} \tag{4.13}$$

that describes the contribution of scattering to the total extinction. $\tau(s)$ is the optical depth, defined as

$$\tau(s) = \int \kappa(s)\,\mathrm{d}s \tag{4.14}$$

and expresses the optical thickness.[2] I_0 is the solar irradiance. The first term in the source function (4.12) is the contribution of the diffuse radiation; the second term is the solar contribution of the radiance.

We omit a further description of the radiative transfer equation at this place and refer to Lenoble (1993). It should be mentioned that

---

2 The atmosphere is called 'optically thick' (or opaque) if $\tau(s) > 1$ and 'optically thin' for optical depths below 1. An optically thin medium is one in which the average photon can traverse the medium without being absorbed.

a special integral form of the radiative transfer equation is used in
Sciarays, where thermal atmospheric emissions and inelastic scat-
tering are neglected. Further, the Sun-normalized radiance

$$R_I(\vec{r}, \Omega) = \frac{R_\lambda(\vec{r}, \Omega)}{I_0} \tag{4.15}$$

is used instead of the radiance R_λ.[3]

The integral form of the radiative transfer equation as used in Scia-
rays can therefore be expressed as

$$R_I(s_a, \Omega) = R_I(s_b, \Omega) \, e^{-\tau(s_b)} + \int_{s_b}^{s_a} \kappa(s) \, J_\lambda(s, \Omega) \, e^{-\tau(s)} \, ds \,. \tag{4.16}$$

The nomenclature for the used parameters is explained in Figure 4.1.
s_a and s_b are the path coordinates where the line of sight (Los) of the
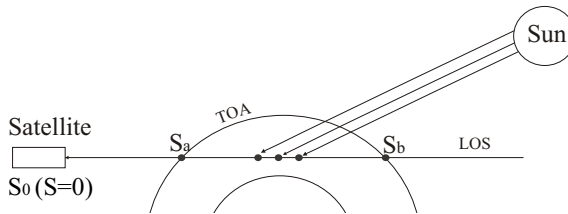
Figure 4.1: Nomenclature used for the parameters for the evaluation of the
discretization in Sciarays. toa denotes the top of the atmosphere.

satellite enters at the top of the atmosphere. The first summand in
the integral form (4.16) represents the Sun-normalized radiances that
have been transmitted directly from the Sun to the satellite and is only
non-zero in the occultation viewing mode. The second summand mod-
els the diffuse radiation between s_b and s_a. The integral form (4.16)
reduces the general form of the radiative transfer equation (4.11) to a
linear summation problem.

———————

3 $R_I(\vec{r}, \Omega)$ has the unit $[\mathrm{sr}^{-1}]$.

4.3 Radiative Transfer Model SCIARAYS

The radiative transfer model SCIARAYS (Kaiser, 2001) employs the integral form (4.16) of the radiative transfer equation by integrating the radiances for all possible paths through the atmosphere. A total of six types of path are considered (see Figure 4.2).
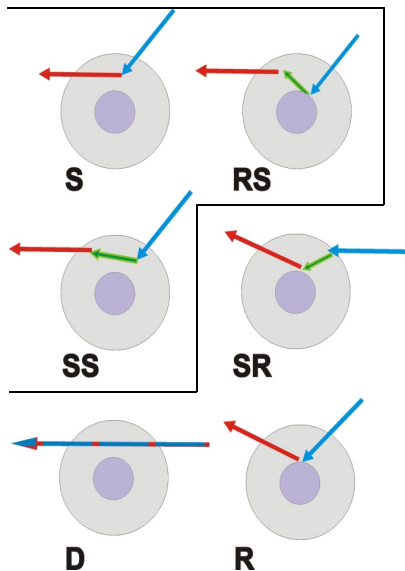
Figure 4.2: Ray paths through the atmosphere as modeled by SCIARAYS. S denotes the path including one scattering event, SS denotes paths with double scattering events, RS denotes paths with first reflected and then singly scattered events, and SR denotes events of initial single scattering and subsequent reflection. D denotes paths in occultation mode and R paths only have reflection. In limb viewing geometry, only the paths S, RS, and SS are considered in SCIARAYS.

In limb viewing geometry only radiation which is scattered directly into the spectrometer slit, contributes to the signal, i.e., S, RS and SS. Figure 4.3 shows the contributions of these relevant paths to the total signal measured in limb viewing geometry in both the ultraviolet and visible for a ground albedo of 0.5 at 60 km tangent height. Only absorption by ozone was considered for this study.
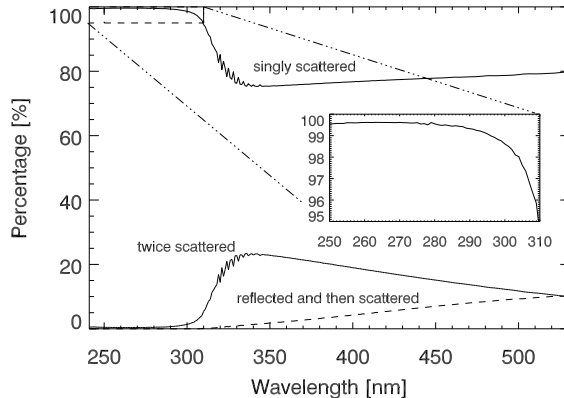
Figure 4.3: Contributions of the relevant paths to the total signal at 60 km tangent height modeled with SCIARAYS. Albedo A is set to 0.5 and only absorption by ozone is considered. The contribution from the path that includes only single scattering events is dominant below 310 nm due to the strong absorption by ozone in the Hartley bands.

Below 310 nm nearly the entire signal is composed of singly scat-tered light, this is due to the strong absorption of radiation by ozone. In the Huggins bands at 330 nm twice scattered light contributes about 25 % to the total radiance measurement. The reflection from the sur-face is almost negligible and has no contribution below 310 nm. In the Hartley bands, SCIARAYS can therefore operate in the single scattering mode what is computationally very efficient.

Before the discretization is described some conventions of the no-tation are given. All quantities with a $\star$ denote line-of-Sun variables, i.e., the quantities related to that part of the path from the Sun to the line of sight.[4] A $\bullet$ denotes the parameters along the line of sight to s_a.[5] The total radiance can then be described as an integral along all path coordinates s by

$$I(s_a, \Omega) = \int_{s_a}^{s_b} \sigma(s)\, \Phi(s, \Omega, \Omega')\, I_D(s, \Omega)\, e^{-\tau^{\bullet}(s)}\, ds\,, \qquad (4.17)$$

where $I_D(s, \Omega)$ denotes the directly transmitted solar radiances at the

───────────

4 See the blue path in Figure 4.2.

5 Along the red solid line in Figure 4.2.

paths coordinates s and the angle of the incident solar radiance Ω. $\tau(s)^\bullet$ describes the optical depth at the path coordinate s along the line of sight. The solar irradiance is expressed by a δ function. Thus Equation (4.17) can be written as

$$I(s_a, \Omega) = \int_{s_a}^{s_b} \sigma(s)\, \Phi(s, \Omega, \Omega^\star)\, e^{-\tau^\bullet(s) - \tau^\star(s)}\, ds\,. \qquad (4.18)$$

$\Omega^\star$ denotes the direction of the direct solar radiation and $\tau^\star$ the optical depth from the Sun to s.

The values of the optical depths and the scattering coefficient σ for each altitude level need only be calculated once and are stored, this minimizes the computational cost.

The optical depth τ is the sum of the extinction coefficients along each partial path Δl_i (see Equation (4.14)), i.e.,

$$\tau = \int \kappa(s')\, ds' = \sum_i \kappa_i\, \Delta l_i\,. \qquad (4.19)$$

With $\Delta L_{i,j}$ as the total length through the discrete points along the total ray path,

$$\Delta L_{i,j} = \Delta l_{i,j}^\bullet + \Delta l_{i,j}^\star\,, \qquad (4.20)$$

the discretized integral form of the radiative transfer equation for one scattering event is

$$I(s_a, \Omega) = \sum_j \Phi\Big(s\big(z(j)\big), \Omega^\star, \Omega\Big)\, \sigma\big(z(j)\big)\, \exp\big(\textstyle\sum_i \kappa_i\, \Delta L_{i,j}\big)\,. \tag{4.21}$$

The summation over j denotes the summation over all altitudes, and i denotes the summation over all partial paths Δl_i.

The discretization for all other possible paths as indicated in Figure 4.2 can be found in Kaiser (2001).

SCIARAYS derives the Rayleigh scattering, aerosol scattering, refractive bending, trace gas absorption using tabulated temperature-dependent cross sections, and Lambertian surface reflection in a fully spherical geometry. Currently, aerosol absorption, clouds, and thermal emissions are not included in SCIARAYS.

Weighting functions (Rodgers, 2000) are derived analytically in Sciarays through the derivation of the radiance with respect to the ozone gas concentrations. This will be explained in detail in the next section. Expressions of the specific weighting functions with respect to albedo, trace gas concentrations, temperature, pressure, albedo and aerosols can also be derived.

5 Inversion

In this chapter, the mathematical formalism of the inversion of a measurement to an atmospheric parameter is introduced. A more comprehensive description of the inversion formalism can be found in Rodgers (2000).

5.1 Conceptual Formulation

A set of measurements is described by a vector $\vec{y}$ through

$$\vec{y} = [y_1, y_2, \ldots, y_m]^{\mathrm{T}}. \tag{5.1}$$

$\vec{x}$ may be an atmospheric state vector,

$$\vec{x} = [x_1, x_2, \ldots, x_n]^{\mathrm{T}}. \tag{5.2}$$

The relationship between $\vec{y}$ and $\vec{x}$ is given by a forward model function $\boldsymbol{F}$ by

$$\vec{y} = \boldsymbol{F}(\vec{x}, \vec{b}) + \vec{\epsilon}. \tag{5.3}$$

$\vec{b}$ denotes a model parameter vector and $\vec{\epsilon}$ the model error.[1]

The derivation of the measurement $\vec{y}$ based on a known atmospheric state is called forward calculation, while the derivation of $\vec{x}$ based on a known measurement vector is called inversion.

---

1 For the inversion presented in this thesis the forward model $\boldsymbol{F}$ is represented by the radiative transfer model in SCIARAYS. The model parameter vectors are the given absorption cross sections, the temperature climatology, etc., which have to be adapted to a given physical environment.

5.2 Inversion of Linear Problems

The simplest way to describe a relation between atmospheric states
and measured values is with a linear model. It is easy to calculate
by solving a system of linear equations. If two states are not too far
apart, then a linear description is an appropriate way to determine the
unknown atmospheric state from the known. In this case the forward
model $\boldsymbol{F}$ is linear, and a $(m \times n)$ matrix $\boldsymbol{K}$ can be defined by

$$\vec{y} = \boldsymbol{K}\vec{x} + \vec{\epsilon}. \tag{5.4}$$

$\boldsymbol{K}$ is called the weighting function matrix, which can be derived from
the forward model functions $\boldsymbol{F}$ by

$$\boldsymbol{K}_i = \nabla_{\vec{x}} \boldsymbol{F}(\vec{x})|_{\vec{x}_i} \tag{5.5}$$

with the elements

$$\boldsymbol{K}_{i,kl} = \left.\frac{\partial F_k}{\partial x_l}\right|_{\vec{x}_i}. \tag{5.6}$$

A linear equation system may now be given by

$$\vec{y} = \boldsymbol{K}\vec{x} \quad \text{with } \vec{y} \in \mathbb{R}^m, \vec{x} \in \mathbb{R}^n, \boldsymbol{K} \in \mathbb{R}^{m \times n}. \tag{5.7}$$

This system of equations is quite easy to solve, if $m = n = r$, where r is
the rank[2] of the matrix. The matrix $\boldsymbol{K}$ is regular and thus invertible,
and a unique solution of the inverse problem can be found by

$$\vec{x} = \boldsymbol{K}^{-1}\vec{y}. \tag{5.8}$$

Usually an exact solution of a linear equation system does not exist
if the number of equations and the dimension of $\vec{y}$ and $\vec{x}$ are not
equal. This problem is called ill-conditioned: for $m > n$ this problem
is over-constrained, and under-constrained for $m < n$. Minimizing the
residuals between $\boldsymbol{K}\vec{x}$ and $\vec{y}$ can only yield an estimate. A common
method is the Least Square fitting, where the minimum of the mean
square of the difference is searched,

$$\|\boldsymbol{K}\vec{x} - \vec{y}\| \rightarrow \min. \tag{5.9}$$

The best fit can be found readily by iteration (Rodgers, 2000)

$$\vec{\hat{x}} = \left(\boldsymbol{K}^{\mathrm{T}}\boldsymbol{K}\right)^{-1}\boldsymbol{K}^{\mathrm{T}}\vec{y}. \tag{5.10}$$

---

2 The rank of a matrix is the number of linear independent equations.

5.3 Regularization

For most of the inversions a solution is difficult to find as the Least
Square fit diverges. Therefore, an additional parameter correlated reg-
ularization matrix $\boldsymbol{H}$, weighted by a regularization parameter γ, is
introduced (Twomey, 1977).[3]

$$(\boldsymbol{K}\vec{x} - \vec{y})^{\mathrm{T}} (\boldsymbol{K}\vec{x} - \vec{y}) + \gamma\,\vec{x}^{\mathrm{T}}\boldsymbol{H}\vec{x} \equiv \min .\qquad(5.11)$$

A solution of Equation (5.11) is given by

$$\vec{\hat{x}} = \left(\boldsymbol{K}^{\mathrm{T}}\boldsymbol{K} + \gamma\boldsymbol{H}\right)^{-1}\boldsymbol{K}^{\mathrm{T}}\vec{y}.\qquad(5.12)$$

γ can be determined analytically, but usually γ is adapted to the
inversion problem empirically.

5.4 Optimal Estimation

A more problem specific regularization is the introduction of so called
a priori knowledge. Instead of the regularization parameter γ, a known
climatology, e.g., of ozone, is used to constrain the conditional equa-
tion in such a way that large deviations between the solution and the
a priori climatology are considered unlikely and small deviations are
more likely. This regularization is expressed by a matrix $\boldsymbol{S}_a$ whose
diagonal elements $S_{a,ii}$ contain the variances of the climatology.

A common covariance matrix, the one used for the inversions in
this thesis, is the following (Rodgers, 2000). The off-diagonal elements
of the covariance matrix contain the covariances with respect to the
climatology elements $x_{a,i}$ and $x_{a,j}$,

$$S_{a,ij} = \sigma_{a,ii}^2 \,\exp\!\left(-\frac{z(i) - z(j)}{h}\right).\qquad(5.13)$$

$(\boldsymbol{\sigma}_{a,ij})$ is the covariance of the climatology, $z(i)$ and $z(j)$ are the corre-
sponding altitudes, and h is a length scale, which is usually determined
empirically. The relationship between two covariances is therefore de-
scribed by their distance in an exponential way.

---

3 The employed formalism is similar to the Lagrangian multiplier method.

An additional regularization is given by an estimate of the measurement error. The measurement covariance matrix $\boldsymbol{S}_y$ contains the measurement covariances and is usually a diagonal matrix. The diagonality expresses the independence of the measurement errors.

With the problem related regularization by these defined covariance matrices, the minimization problem can be expressed as

$$(\boldsymbol{K}\vec{x} - \vec{y})^{\mathrm{T}} \boldsymbol{S}_y^{-1} (\boldsymbol{K}\vec{x} - \vec{y}) + (\vec{x} - \vec{x}_a)^{\mathrm{T}} \boldsymbol{S}_a^{-1} (\vec{x} - \vec{x}_a) \equiv \min . \quad (5.14)$$

A solution of the minimization problem (5.14) is given by

$$\hat{\vec{x}} = \vec{x}_a + \left(\boldsymbol{K}^{\mathrm{T}} \boldsymbol{S}_y^{-1} \boldsymbol{K} + \boldsymbol{S}_a^{-1}\right)^{-1} \boldsymbol{K}^{\mathrm{T}} \boldsymbol{S}_y^{-1} (\vec{y} - \boldsymbol{K}\vec{x}_a) \qquad (5.15)$$

(Rodgers, 2000) with the a posteri covariance matrix

$$\hat{\boldsymbol{S}} = \left(\boldsymbol{K}^{\mathrm{T}} \boldsymbol{S}_y^{-1} \boldsymbol{K} + \boldsymbol{S}_a^{-1}\right)^{-1} . \qquad (5.16)$$

5.5 Contribution Functions and Averaging Kernels

Theoretically, the retrieved state $\hat{\vec{x}}$ can be expressed as a function of the true state $\vec{x}$ by

$$\hat{\vec{x}} = \boldsymbol{A} (\vec{x} - \vec{x}_a) + \vec{x}_a + \hat{\boldsymbol{S}} \boldsymbol{K}^{\mathrm{T}} \boldsymbol{S}_y^{-1} \boldsymbol{\epsilon} \qquad (5.17)$$

(Rodgers, 2000, (2.45, 2.58)) with

$$\boldsymbol{A} = \hat{\boldsymbol{S}} \boldsymbol{K}^{\mathrm{T}} \boldsymbol{S}_y^{-1} \boldsymbol{K} \qquad (5.18)$$
$$= \boldsymbol{D} \boldsymbol{K} , \qquad (5.19)$$

where the averaging kernel matrix $\boldsymbol{A}$ is the Jacobian of the retrieved state $\hat{\vec{x}}$ with respect to the true state,

$$\boldsymbol{A} = \frac{\partial \hat{\vec{x}}}{\partial \vec{x}} . \qquad (5.20)$$

$\boldsymbol{D}$ is called the contribution function, i.e., the change of the retrieved state with respect to the measurement. The averaging kernel matrix $\boldsymbol{A}$

characterizes the particular retrieval. If the last error term $\hat{\boldsymbol{S}} \, \boldsymbol{K}^{\mathrm{T}} \, \boldsymbol{S}_y^{-1} \, \boldsymbol{\epsilon}$ is neglected, then the retrieved state can be expressed by the sum of the *a priori* and the averaging kernel weighted difference of the true state and the *a priori*. If $\boldsymbol{A}$ is a unity matrix, then the retrieved state $\hat{\vec{x}}$ is the true state, an ideal case. For a vanishing averaging kernel, the retrieval vector $\vec{x}$ is the *a priori*. In this case the retrieval contains no information from the measurement.

In an ideal case the averaging kernels are δ functions. But in practical applications, they are broadened over an altitude region, expressed by the off-diagonal elements in $\boldsymbol{A}$. This is taken as a measure of the vertical resolution, quantitatively expressed by the Full Width at Half Maximum (FWHM).

5.6 Non-linear Problem and Newton Iteration Scheme

Inversion problems for atmospheric trace gas profiles are mostly non-linear problems. The retrieval of atmospheric trace gases is sometimes a moderately non-linear problem, i.e., a problem for which linearization is adequate for the error analysis, but not for obtaining a solution (Rodgers, 2000). A solution for this equation system can be evaluated from the linear problem, but ultimately requires an iterative process for solution, e.g., a Newton Iteration method can be applied. This approach is based on the Taylor expansion of the forward model $\boldsymbol{F}$ around a profile $\vec{x}_n$,

$$\vec{y} = \boldsymbol{F}(\vec{x}) \approx \boldsymbol{F}(\vec{x}_n) + \frac{\partial \boldsymbol{F}(\vec{x}_n)}{\partial \vec{x}} (\vec{x} - \vec{x}_n) \,. \tag{5.21}$$

A solution is given by

$$\vec{x}_{i+1} = \vec{x}_i + \hat{\boldsymbol{S}}_{i+1} \left(\boldsymbol{K}_i^{\mathrm{T}} \, \boldsymbol{S}_y^{-1} \, (\vec{y} - \vec{y}_i) + \boldsymbol{S}_a^{-1} \, (\vec{x}_a - \vec{x}_i) \right) , \tag{5.22}$$

where

$$\boldsymbol{K}_i = \left. \frac{\partial \boldsymbol{F}(\vec{x})}{\partial \vec{x}} \right|_{x_i} \tag{5.23}$$

is the weighting function matrix of the non-linear forward model $\boldsymbol{F}$ for the i-th iteration, and

$$\hat{\boldsymbol{S}}_{i+1} = \left(\boldsymbol{K}_i^{\mathrm{T}} \, \boldsymbol{S}_y^{-1} \, \boldsymbol{K}_i + \boldsymbol{S}_a^{-1}\right)^{-1} \tag{5.24}$$

the retrieved state covariance matrix. SCIARAYS derives the weighting functions (5.23) analytically.

The calculations are repeated at the new linearization point $\vec{x}_{i+1} = \hat{\vec{x}}_{i+1}$. An empirical convergence criterion has to be chosen to stop the iteration. One possible truncation is the χ^2 criterion. Using this method, a minimum in the function

$$\chi^2 = \chi_x^2 + \chi_y^2 , \tag{5.25}$$

within a predefined threshold is searched, where

$$\chi_y^2 = \left(\vec{y} - \boldsymbol{F}(\vec{x})\right)^{\mathrm{T}} \boldsymbol{S}_y \left(\vec{y} - \boldsymbol{F}(\vec{x})\right) \tag{5.26}$$

and

$$\chi_x^2 = (\vec{x} - \vec{x}_a)^{\mathrm{T}} \boldsymbol{S}_a \left(\vec{x} - \vec{x}_a\right) . \tag{5.27}$$

This corresponds to the minimization problem (5.14). Since χ^2 is weighted by the covariance matrices, it provides an adequate way to involve the measurement properties and the *a priori*.

Part II

The Inversion Algorithm

6 Methodology

In this chapter, an introduction to the methodology for the retrieval of ozone profiles from limb scatter measurements is given. Results from the retrieval are described, and sensitivity studies and validations presented.

6.1 Characteristics of Ultraviolet Limb Radiance Profiles

The SCIAMACHY limb radiances originate from transmitted, reflected, and scattered sunlight. Their quantity depends on the solar zenith angle, the tangent height, the wavelength, and usually on further parameters such as albedo, cloudiness and aerosol loading. Additionally, atmospheric emissions and external stray light from outside of the field of view contribute to the signal.

As ozone is the dominant absorber in the Hartley bands (Buchwitz, 2000), other trace gases can be neglected. Also, the effect of aerosols need not be taken into account.[1]

Figure 6.1 shows modeled limb radiance spectra in the ultraviolet and visible regions for different tangent heights between 2 km to 90 km. The limb radiance decreases with increasing wavelength and tangent height, except in the Hartley bands. The ozone absorption in the Chappuis and in the Hartley bands cause a strong decrease in the spectra. The absorption in the Chappuis bands is only apparent at lower altitudes, whereas the absorption in the Hartley bands is ap-

---

1 It will be shown later, e.g., that aerosol scattering below 300 nm is smaller than 2 % in relation to the total backscattered signal. See also von Savigny (2002).
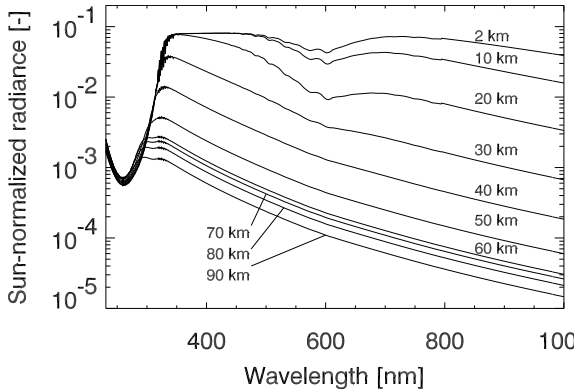
Figure 6.1: Modeled Sciamachy limb spectra in the ultraviolet and visible at different tangent heights. Aerosols and other trace gases except for ozone have been neglected in the model.

parent at higher altitudes. Thus, ozone absorbs radiation at different wavelengths at different altitudes.[2]

Figure 6.2 shows sample ultraviolet limb radiance profiles as a function of the tangent height.

At high tangent heights, only few photons are scattered into the spectrometer while at lower altitudes, no additional photons reach the instrument from the far field. This is due to the increase in path length along the line of sight so that additional Rayleigh scattering and ozone absorption cause a maximum in the radiances. This reversal point is called 'knee' because of its similarity to a human knee. The altitude of this knee depends only on the optical depth, which increases with solar zenith angle (von Savigny, 2002). Figure 6.3 shows the weighting functions for two sample inversions of radiance measurements at different solar zenith angles. These weighting functions indicate a larger sensitivity to ozone at measurements at higher altitude and larger solar zenith angle.

Ozone absorption and Rayleigh scattering contribute to the radiance to a different extent. The 'tightened knee', e.g., at 260 nm,

----

2 This is the reason for the determination of stratospheric ozone densities using the Chappuis wavelengths, and upper atmospheric ozone using the Hartley bands.
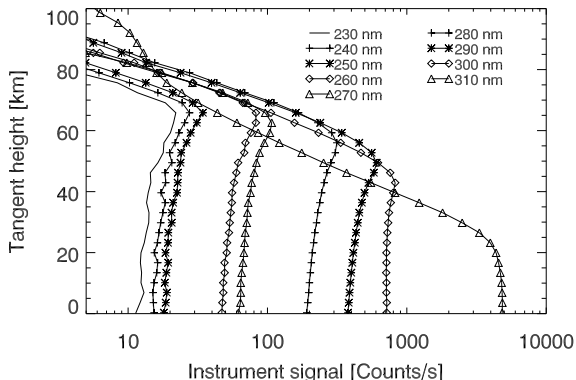
Figure 6.2: Sample SCIAMACHY limb radiance profiles at different wavelengths between 230 nm and 310 nm. The measurement was performed on 12 March 2003. A specific measurement will be denoted by date, orbit, number, and state, i.e., (20030312, 05387, 1244, 7).
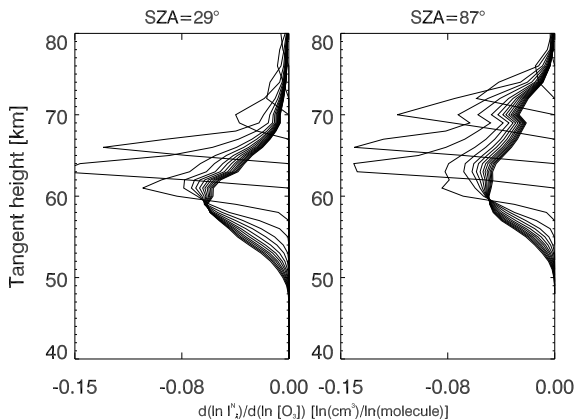
Figure 6.3: Weighting functions from two inversions of SCIAMACHY measurements at 264 nm at different solar zenith angles. At high altitudes, the optical depth at the larger solar zenith angle is larger than at a small solar zenith angle. Sample measurements were taken on 24 September 2004 (08188, 2849, 1), and (08188, 2844, 1).

is called the 'ozone absorption knee' while the 'spread knee', e.g., at 310 nm, is called 'Rayleigh knee' due to the comparatively larger contribution from scattering than from absorption.

The knee can be employed for precise altitude retrievals. The first retrievals of the tangent heights were performed from data of the Rayleigh Scattering Altitude Sensor (Rsas) (Janz et al., 1996). The same method was employed for measurements from the Solse/Lore instruments (McPeters et al., 2000) and from the Optical Spectrograph and Infra-Red Imaging System (Osiris) (Sioris et al., 2003). The Tangent height Retrieval by Ultraviolet-B Exploitation (True) (Kaiser et al., 2004) has been used to improve the Sciamachy tangent height information. True Version 1.4 uses Sciamachy limb scatter measurements between 295 nm and 305 nm at tangent heights between 35 km to 50 km and ozone profiles from a climatology. An Optimal Estimation scheme and Sciarays are used to fit the stratospheric ozone concentrations in tropic regions, which are known to have only a small variability.

Monthly averaged offsets of Sciamachy tangent heights as retrieved by True are shown in Figure 6.4. The reason for the large offsets before December 2003 was an inconsistent coordinate system for the on-board and on-ground program codes. After the improvement
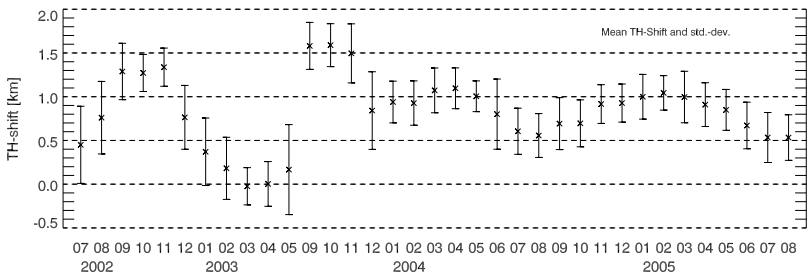
Figure 6.4: Monthly mean tangent height offsets of Sciamachy limb measurements and respective standard deviations as derived by the tangent height retrieval True (von Savigny et al., 2005a). The seasonal variation is significant. The amplitudes are smaller after the update of the Envisat propagator model in December 2003.

with True, offsets of up to 2 km are still observable and a seasonal dependence can be seen (von Savigny et al., 2004). In the inversion presented in this work, tabulated tangent height offsets from True Version 1.4 are used, these lead to an estimated maximum error of between 300 m and 500 m.

Noctilucent Clouds

Noctilucent clouds make up a several kilometer wide thin layer of macroscopic ice particles smaller than 100 nm. They occur only at polar latitudes in the southern hemisphere between December and February and in the northern hemisphere between June and August. Their altitude is near the mesopause, at about 83 km, where low temperatures allow particle formation. Noctilucent clouds are observable from the ground only during twilight, when the observer is in darkness and the clouds themselves remain sunlit. Leslie (1885) is supposed to have been the first observer of noctilucent clouds.

Many of the properties of noctilucent clouds are still unknown as are their scattering properties, which are frequently but only approximately described by Mie theory.[3]

Figure 6.5 shows how noctilucent clouds affect Sciamachy limb radiance profiles, this indicates that the limb radiance may increase by one order of magnitude if noctilucent clouds are present.

Noctilucent clouds affect Sciamachy observations because every limb measurement makes also measurements in the mesopause region. Sometimes every second Sciamachy measurement is unusable for a profile retrieval. Therefore an upstream cloud detector algorithm was implemented, this rejects all unusable measurements before the inversion module.

---

3 The Mie theory is strictly speaking only valid for spherical and di-electrical particles. This approach is only approximately fulfilled for the particles of noctilucent clouds. For a comprehensive review of noctilucent clouds observations and related observation techniques see Avaste et al. (1980) and for the microphysical and scattering properties Kokhanovsky (2005).
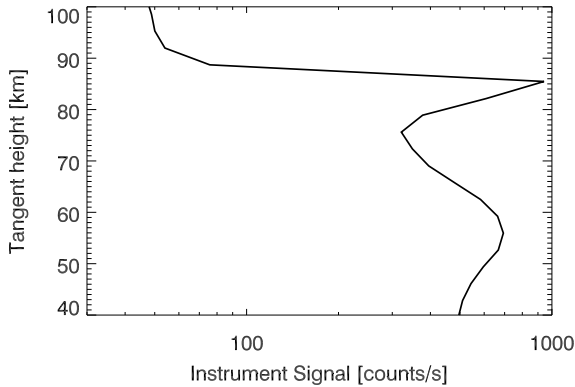
Figure 6.5: SCIAMACHY limb radiance profile at 290 nm measured on 2 August 2002 (76.6° N, 117° W) which indicates the presence of noctilucent clouds. The solar zenith angle at the measurement was 71.5°.

6.2 Highest Possible Altitude for Ozone Profile Retrievals in the Hartley Bands

Information about scattering and absorption by ozone is provided at and above the knees of the radiance profiles; in the Hartley bands ozone is almost exclusively the source for all of the information. The knee in the limb radiance profiles is located at the highest possible altitude when the absorption and scattering are strongest, i.e., where the ozone cross sections exhibit a maximum, approximately 255 nm. The radiance knees at wavelengths beyond the maximum of the ozone cross sections are located at lower altitudes.

Thus the limb radiance profiles at wavelengths between 250 nm and 310 nm (Figure 6.2) indicate that they can basically be used to deduce ozone concentrations at altitudes above 35 km. The precise extent of the retrieval sensitivity can be determined from the derivation of the specific weighting functions that show the change of the radiances at certain wavelengths and altitudes with respect to the ozone concentration. The initial weighting functions presented in Figure 6.3 indicate the sensitivity of this retrieval methodology at altitudes up to 70 km.

6.3 Wavelength Selection

To the present, no reasons for wavelength selection have been given in documentations of previous ozone profile retrievals from ultraviolet limb scatter measurements. The ozone profile retrievals from Sme measurements (Rusch et al., 1983), to date the only successful ozone retrieval from satellite borne ultraviolet limb backscatter observations, exploits radiances at 265 nm and 296.4 nm, but without giving reasons for that choice. Ozone profile retrievals with measured radiances at wavelengths in the Hartley bands from Solse observations failed due to the bad signal-to-noise ratio of the instrument, and even in the corresponding theoretical elaboration (Flittner et al., 2000), no reasons for a specific wavelength selection were mentioned.

A continuous sample of wavelengths is excluded as strong emissions from atmospheric constituents contribute to the measurements that are not modeled by Sciarays. However, this section discusses the selection of an applicable set of wavelengths that ensure a reliable inversion of Sciamachy limb measurements to ozone profiles.

6.3.1 Fraunhofer Lines and Emission Lines

A selection of thirteen wavelengths was made for an analysis of the Fraunhofer lines in which the wings of the Fraunhofer lines are avoided. The sampled radiances are integrated over a spectral range of 2 nm.

Possible emissions are either the airglow from atmospheric trace gases, or originate from metals, which enter the atmosphere through space debris (Huffman, 1992).

Figure 6.6 shows the most prominent airglow emissions in satellite borne limb measurements in the ultraviolet, visible, and infrared (López-Puertas, 2000).

1. 'NO-γ': These are the most prominent emission features in the ultraviolet. They originate from the vibrational transitions in $X^2\Pi \leftarrow A^2\Sigma$ electronic transition. The brightness of the NO-γ bands in the day glow and in the twilight depends on the incident radiation. They have a significant impact on the measurements due to the
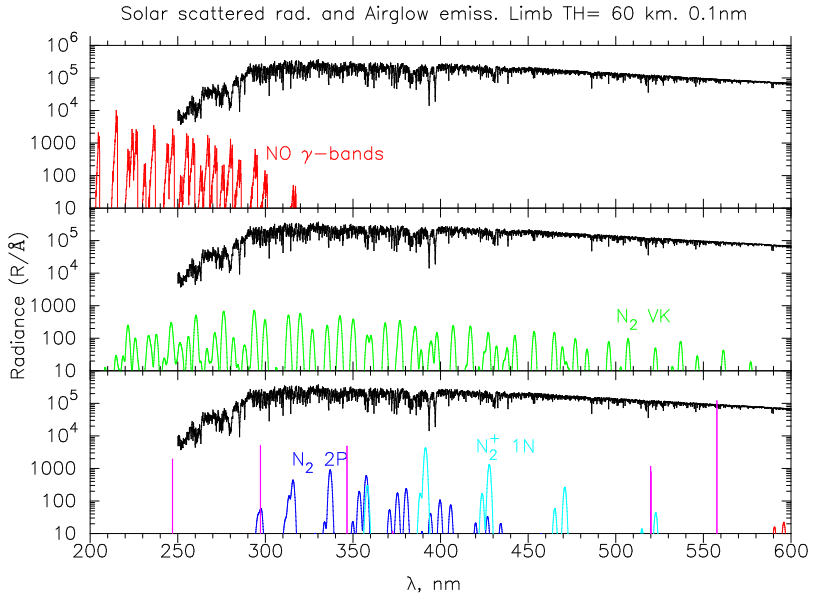
Figure 6.6: Modeled airglow emissions in limb viewing mode in the ultra-violet at 60 km tangent height. Also depicted are the modeled total limb radiances. In some cases the intensity of modeled emissions reaches the ambient limb radiances. Figure courtesy of López-Puertas (2000).

increase of NO at higher altitudes. Their contribution to the total limb radiances, e.g., at 80 km reaches 20 % at 255 nm and up to 40 % at 220 nm. Below 220 nm the NO-γ emissions are as strong as the ambient radiation.

2. N_2 'Vegard-Kaplan' (Vk): These originate from the forbidden sin-glet and triplet $(X^1\Sigma_g^+ \leftarrow A^3\Sigma_u^+)$ transitions, and overlay the whole ultraviolet and visible spectral range from 200 nm to 600 nm. Usu-ally they contribute less than 1 % .

3. N_2 'Second Positive' (2 Pg): These are day glow features in the near ultraviolet and visible caused by the transition $X^1\Sigma_g^+ \leftarrow B^2\Sigma_u^+$ and can be neglected due to their low intensity.

4. Atomic oxygen lines: Three oxygen lines can be identified in the ultraviolet: Two lines at 247.0 nm and 247.1 nm $(^2P - {}^4S)$, and one line at 297.2 nm $(^1S - {}^3P)$ (Rees, 1989).

6.3.2 Metal Emissions

Many types of space debris enter the Earth's atmosphere, e.g., meteorites, comets, or asteroids.[4] The debris consists of chemical elements like carbon, silicon, metals, and other trace elements. Some of this debris can reach the middle atmosphere and emit radiation.

In addition to the permanent layers of magnesium, sodium, calcium, iron, and silicate ions and neutrals (Fritzenwallner and Kopp, 1998) thin sporadic layers at altitudes above 90 km have been discovered, (e.g., Clemesha, 1995). The amounts of the precipitating elements increase after meteor showers but small meteorites penetrate the Earth's atmosphere continually. These layers therefore exist permanently but not to the same extent as during strong meteorite showers.

A prominent meteor shower is caused by the Tempel-Tuttle comet, namely the Leonid meteorites. The diameter of the comet is about 3.5 km, with an orbit time around the Sun of 33 years, the Earth crosses this orbit every year, around the 14th of November (see, e.g., Carbary et al., 2003).

Attempts to identify the emissions caused by the Leonid were made in a Sun-normalized Sciamachy spectrum six weeks after the Leonid meteorite in an effort to estimate the contribution of these emissions to limb measurements (Figure 6.7). The tangent height of the presented measurements is 92 km. The wavelengths of the expected NO-γ and metal emissions have been marked in the figure.

Figure 6.7 also shows modeled NO-γ emissions for several vibrational transitions. The NO-γ emissions dominate. Other emissions are barely detectable except the magnesium lines at 280 nm and 286 nm.

6.3.3 Adjustment by Residuals

Thirteen wavelengths have been selected, avoiding the Fraunhofer lines and emissions from the airglow and metals. The chosen wavelengths have been adjusted by comparing the residuals of the fit algo-

---

4 Meteorites are only some millimeter large, whereas comets possess a size of a few kilometers. The size of asteroids reaches hundreds of kilometers.

Figure 6.7: Sciamachy Sun-normalized limb spectrum from 1 January 2004 at 92 km tangent height. A corresponding NO-γ emission model is over-plotted (blue, thick line) where vibrational transitions are denoted. Data have been averaged over a complete orbit including 31 measurements (20040101, 00907, 2746). The NO-γ model was provided by E. J. Llewellyn.

rithm; the appropriate wavelengths have been found at 250, 252, 254, 264, 267.5, 273.5, 283, 286.5, 290, 295.5, 301, 307, and 310 nm.

6.4 Normalization of the Tangent Heights

The limb radiance profiles (I_{ik}) at the selected wavelengths λ_i are normalized with respect to the limb radiances at a wavelength dependent reference tangent height $I_{i\,\mathrm{ref}}$,

$$I_{ik}^{\mathrm{norm}} = \frac{I_{ik}}{I_{i\,\mathrm{ref}}}, \tag{6.1}$$

$i = 1, \ldots, 13$ being the wavelength index and $k = 1, \ldots, 21$ being the tangent height index.

Generally, the normalization heights are chosen at the center of the respective sensitivity area. The normalization reduces the systematic errors[5] and removes the need for the calibration of the instrument, at least in part.

---

5 The normalization reduces at least the multiplicative errors entirely.

6.5 Program Structure and Settings

After reading in the measurement data, the retrieval vector $\vec{y}$ is built by taking all thirteen normalized limb radiance profiles into one vector. The vector is converted to a logarithm to ensure a better convergence of the inversion as the retrieval vector is always positive (Flittner et al., 2000). Only measurements at tangent heights between 20 km and 80 km are used for the profile retrieval as comparisons with model calculations showed that the atmosphere below 20 km and above 80 km has no impact on the profile retrieval.

The first guess $\vec{y}_a$ is derived through the forward model $\boldsymbol{F}(\vec{x}_a)$. The *a priori* profile $\vec{x}_a$ is provided by the United Kingdom Universities Global Atmospheric Modelling Programme (UGAMP) five-years climatology of observational data sets, i.e., from SME, SBUV, Stratospheric Aerosol and Gas Experiment (SAGE II), and several ozone sonde measurements. SME observations have been used exclusively for the climatology in the mesosphere, in the upper stratosphere mainly SAGE II and SBUV observations have been employed. The UGAMP climatology is resolved monthly and provided on a 5° latitudinal and longitudinal grid.

Air densities are generated from a chemical transport model (McLinden et al., 2000) as a function of latitude and month with temperatures and ozone columns from a combination of several models and measurements (Nagatani and Rosenfield, 1993; McPeters, 1993). Aerosols have not been taken into account in the profile retrieval. The albedo is set to 0.5, as this parameter has almost no influence on the retrieval.

The measurement covariance matrix is a diagonal matrix with covariances of 10 %, and the covariance of the *a priori* climatology is estimated at 65 %.[6] The total covariance matrices $\hat{\boldsymbol{S}}_{i+1}$ are derived iteratively (Equation (5.24)).

---

6 See also the assignment of the *a priori* covariance matrix through Equation (5.13).

The initial weighting functions $\boldsymbol{K}_0$ are derived analytically (Equation (5.5)) and the initial fit is given by

$$\vec{\hat{x}}_1 = \vec{x}_a + \hat{\boldsymbol{S}}_1\,\boldsymbol{K}_0^{\mathrm{T}}\,\boldsymbol{S}_y^{-1}\left(\vec{y} - \vec{y}_a\right) + \boldsymbol{S}_a^{-1}\left(\vec{x}_a - \vec{x}_a\right).\qquad(6.2)$$

The Newton iteration scheme (5.22) proceeds, until the χ^2 criterion (5.25) terminates the iteration. Usually, the algorithm stops after three or four iteration steps, but this depends on the predefined value of the required fit accuracy.

6.6 Results

6.6.1 Weighting Functions

Figure 6.8 shows the weighting functions at each wavelength from a sample profile retrieval. The weighting functions at short wavelength
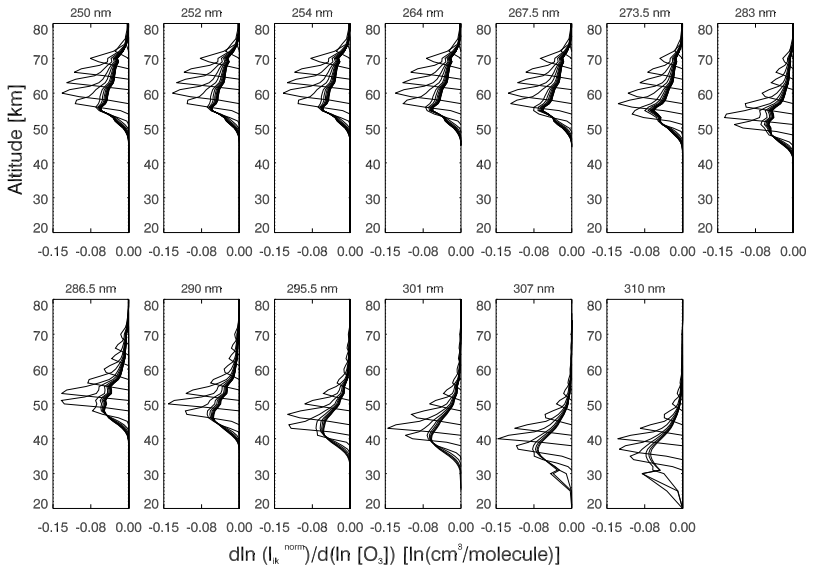
Figure 6.8: Weighting functions at every wavelength from a sample profile retrieval (20030312, 05387, 1244, 7). They show the sensitivity to ozone between 30 km and 70 km with continuous coverage.

indicate a larger sensitivity at higher altitudes, whereas the radiances at longer wavelengths are more sensitive to ozone at lower altitudes. The sensitivity range covers altitudes between 30 km and 70 km, and the coverage is almost evenly distributed.

Most of the information originates from altitudes above the knee.[7] The information content below the respective profile knee decreases rapidly with decreasing altitudes, whereas the information content above the knee decreases more slowly towards higher altitudes.

The respective weighting functions are eventually used for the final adjustment of the normalization altitudes for the respective limb radiance profiles.

6.6.2 Fits and Residuals

Figure 6.9 shows fits of modeled and measured limb radiance profiles for each wavelength from a sample profile retrieval.

The respective residuals are also shown. Most of the radiance profiles agree within 5 % of the model. Only the radiance profile at 250 nm is not matched well by the model, in contrast to the 267.5 nm radiance profile. The left figure in 6.11 shows the averaged residuals for the same profile retrieval. The displayed residuals are not weighted by the sensitivity, but the mean residual of less than 1 % is a good result for modeling backscattered radiation in the atmosphere.

Other sample retrievals show quite different fits to their respective radiance profiles, but on the average show a good match between model and measurement.

Figure 6.10 shows residuals as expressed by χ_x^2, χ_y^2, and χ^2 from a sample profile fit. While χ_y^2 and χ_x^2 exhibit some oscillations, χ^2 converges continuously.[8]

---

7 The limb radiance profiles and the location of the respective knees are displayed on page 74.

8 χ^2 is the determining truncation criteria for the iteration scheme.
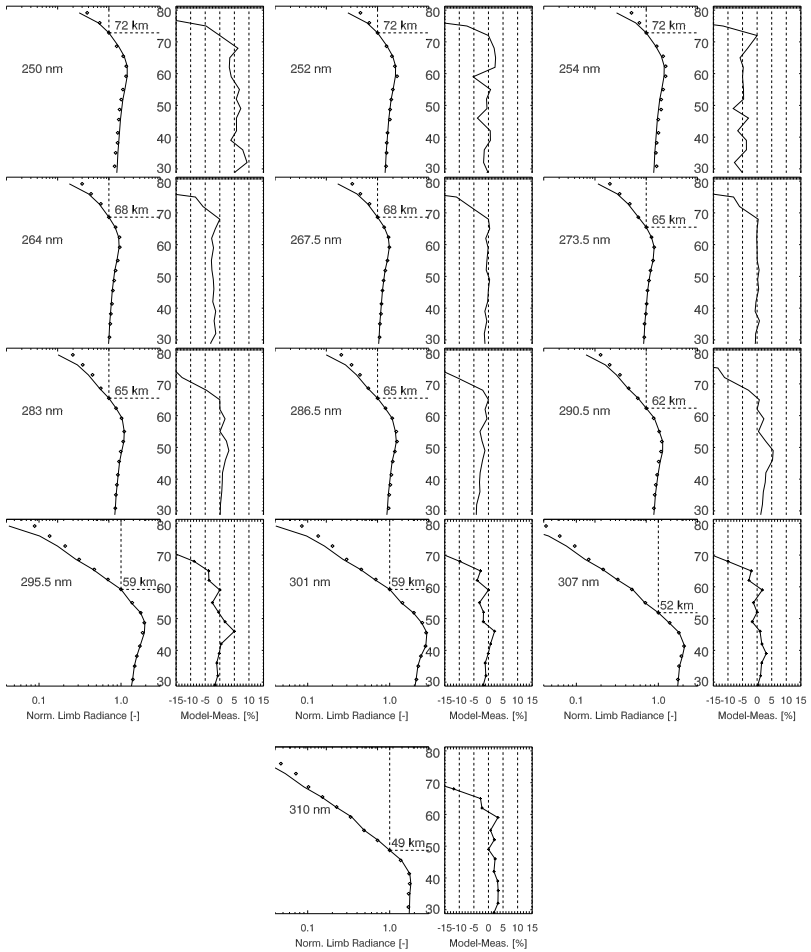
Figure 6.9: Fits of modeled and measured limb radiance profiles for each of the thirteen wavelengths, taken from a sample profile retrieval (20030312, 10945, 1521, 3). The dots denote the measurement and the solid lines the model. The limb radiances are normalized by radiances at a certain altitude, this is denoted by a dashed line and by an altitude specification in the respective figure. In the right panel of the figures the respective residuals are shown.
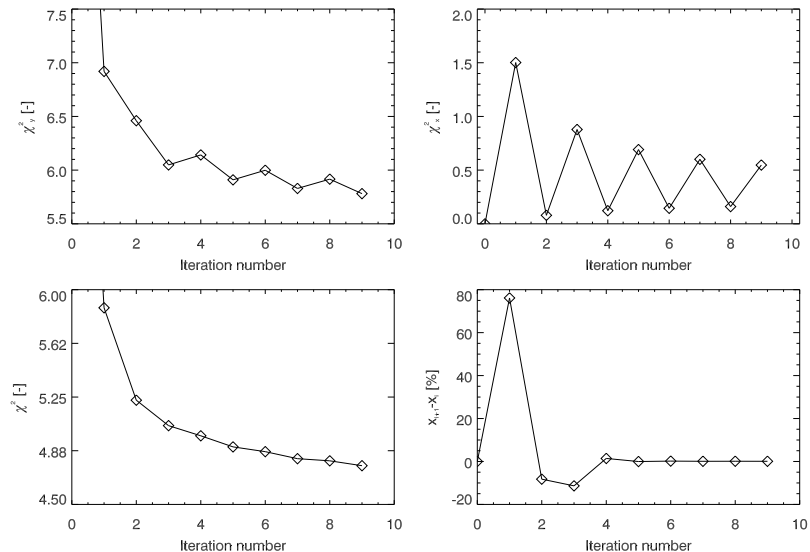
Figure 6.10: χ_y^2, χ_x^2, and χ^2 from a sample profile retrieval (20040303, 10492, 0113, 16). Bottom left: Deviation of two consecutive profiles during the iteration process as a function of the iteration number. The figures show a rapid convergence with only a few iteration steps.

6.6.3 Averaging Kernels

The right panel in Figure 6.11 shows the averaging kernels for a sample profile retrieval. The vertical resolution as given by the FWHM[9] is also shown.

The averaging kernels do not peak at the abscissa with value one. This is due to the fact that the radiative transfer model uses a smaller altitude resolution than the measurement sampling, which is about 3.5 km in contrast to the predefined model grid of 1 km.

Below 40 km and above 70 km, measurements have only a partial or small impact on the profile retrieval. This indicates the limits of the retrieval technique. The vertical resolution as given by the FWHM is about 3 km to 4 km.

---

9 See Section 5.5 for the definition of the FWHM.
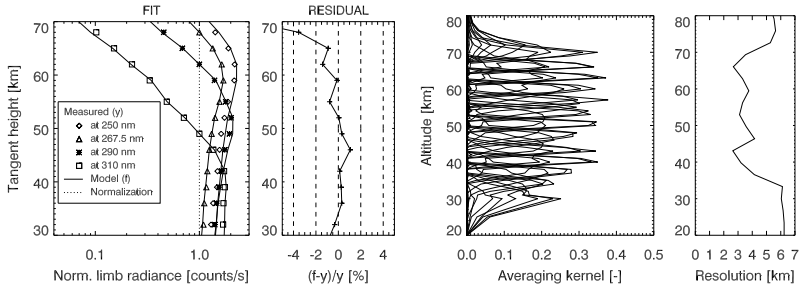
Figure 6.11: Left: Fit of the modeled to the measured radiances for four wavelengths. Data were taken from a profile retrieval from a measurement on 3 March 2004 (10492, 0113, 16). The residual is averaged over all wavelengths. Right: Averaging kernel functions of a sample profile retrieval (20030312, 05387, 1244, 7). Also shown is the vertical resolution of the retrieved profile as given by the Fwhm.

6.6.4 Profiles

Figure 6.12 shows four sample ozone profiles and the respective *a priori* profiles. Below 35 km, the retrieved profiles converge to the *a priori* profiles, which is not the case around 80 km. This is probably due to variable ozone concentrations around 90 km that are difficult to fit. The technique has no sensitivity above the third ozone maximum, and the retrieved and *a priori* profiles converge again.
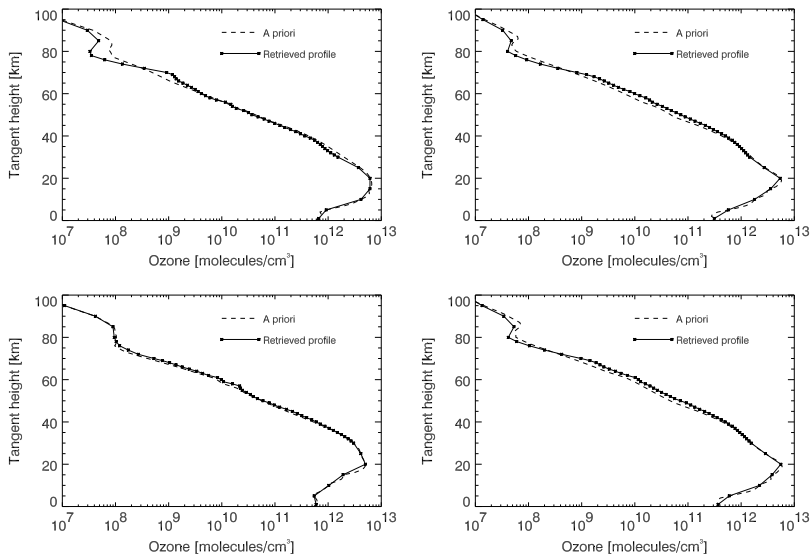
Figure 6.12: Four sample ozone profiles from 12 March 2003 (05387, 1244, 7) (left top), 1 February 2004 (10058, 4644, 25) (right top), and 2 February 2004 (10062, 1586, 22 and 10068, 4682, 22) (bottom left and right). The dashed line represents the employed *a priori* profile. It will be shown later in Chapter 7 that the *a priori* profile has almost no influence on the retrieval.

7 Sensitivity Studies

This section discusses the most important error sources in the evaluated inversion. The true statistical error may be smaller in general as the presented studies treat only worst case scenarios. Thus the results of this section must not be confused with overall statistical errors. The underlying version of the profile retrieval employed for these sensitivity studies is VERSION 2.25.

7.1 Albedo

The contribution of the reflected photons to limb measurements below 310 nm is less than 1 % (see Figure 4.3). Thus no significant impact of the albedo on the profile retrieval is expected.

SCIAMACHY measurements at the smallest possible solar zenith angle, about 30°, display the worst case scenario and are therefore used for this first brief study. The left panel of Figure 7.1 shows the difference between two retrieved ozone profiles with total and no surface reflection.[1] The solar zenith angle of the sample SCIAMACHY measurement is 35°. The largest differences are about 2.5 % at an altitude of 35 km and tend to zero at higher altitudes. The retrieved profile converges to the *a priori* below an altitude of 35 km. The differences below 35 km and above 50 km altitude are negligible.

The error of the inversion introduced by an incorrect albedo can therefore be assumed to be maximum at 35 km and in general less

---

1 These are pre-adjusted in the radiative transfer model, respectively.

than 2.5 %. This value agrees with results of von Savigny (2002) who determined maximum errors of about 2 % for altitudes above 30 km.[2]

7.2 Scattering Modes

The contribution of twice scattered and surface reflected photons to the total ultraviolet limb radiances at 60 km altitude was already estimated to be of only 5 % (see Figure 4.3 on page 50). The small contribution is due to the strong absorption of radiation by ozone in the Hartley bands. Additionally, multiple scattering in the upper atmosphere decreases due to the strong absorption.

To estimate the impact of neglecting multiple scattering on the results of the profile retrieval technique, two profile retrievals of the same SCIAMACHY measurement were performed with and without double scattering.[3] The right panel in Figure 7.1 shows the differences in the retrieved profiles.

The maximum difference reaches 3 % at 35 km, but the differences almost vanish at 45 km. Errors below 35 km decrease again due to small sensitivity of the retrieval technique.

7.3 Aerosols

Von Savigny (2002) carried out an analysis of the impact of aerosols on ozone profile retrievals between 15 km and 40 km from OSIRIS limb measurements. Different multiples of the employed Polar Ozone and Aerosol Experiment (POAM III) aerosol extinction profiles (Lucke et al., 1999) were assumed in their study. Von Savigny (2002) states that the impact of the aerosols on the retrieved ozone profiles above 30 km vanishes and that errors introduced by a five times overestimate of the aerosol climatology profiles are less than 5 % at this altitude.

---

2 Sensitivity studies of a stratospheric ozone profile retrieval from limb scatter measurements from the OSIRIS instrument
3 Pre-adjusted in the radiative transfer model
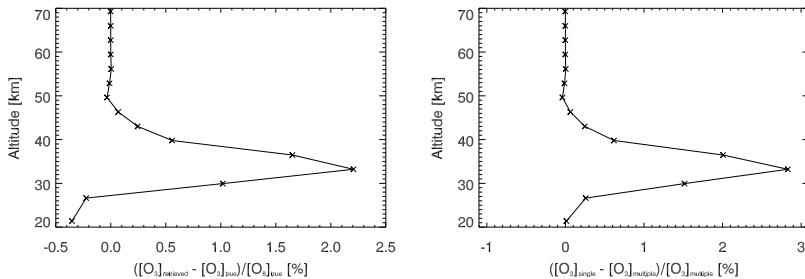
Figure 7.1: Left: Change of a sample profile retrieval of a measurement at a solar zenith angle of 35° (20030312, 05387, 1244, 7) due to a change of the albedo from $A = 0$ to 1. For this study, multiple scattering and reflection were used in the radiative transfer model, this is not the case for the commonly presented profile retrieval. Right: Differences of two profile retrievals of the same measurement caused by neglecting multiple scattering and reflection. The measurement is the same as that used in the study of the impact of the albedo, and the solar zenith angle is again 35°. Maximum differences occur at about 35 km. Below 35 km, differences decrease due to the decreased sensitivity of the inversion.

The POAM III observations of aerosol extinction profiles exhibit a strong exponential decrease with increasing altitude. Thus an enhanced aerosol abundance in the upper atmosphere can be excluded. However, comparisons of retrieved profiles both with and without aerosols in the radiative transfer model indicate that there is no impact of aerosols on the inversion.[4]

7.4 *A Priori* Ozone Profiles

A priori profiles are used for regularization of the inversion. If the *a priori* is far away from the true ozone profile, the iterative fit of the inversion converges slowly or may even diverge. If the regularization on the other hand is too strong, i.e., the *a priori* covariances are too

4 The tiny ice crystals of the noctilucent clouds are also aerosols, and they are a large source of aerosols in the mesosphere (see Section 6.1). Due to the massive scattering properties of ice crystals, the measurements show strong perturbations and are not suitable for a profile inversion.

small, then the information from the measurements is not considered
in an appropriate way and the retrieved profiles contain too much
information from the *a priori* climatology (Section 5.3).

A brief study was carried out to estimate the impact of the applied
a priori profile on the profile retrieval.
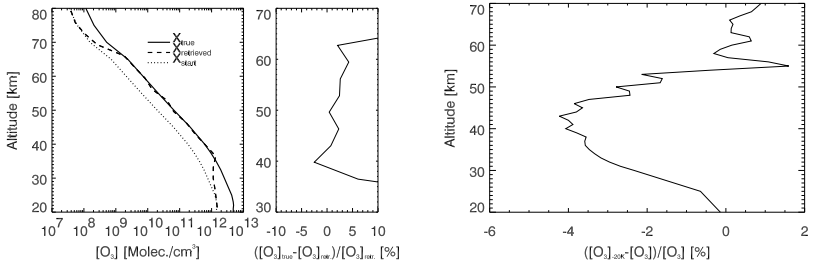
Figure 7.2: Left: For a given ozone profile $\vec{x}_{\text{true}}$, modeled radiances were
used for the retrieval of an ozone profile $\vec{x}_{\text{retrieved}}$ with the *a priori* profile
$\vec{x}_{\text{start}}$. This *a priori* profile is 50 % lower than the true profile $\vec{x}_{\text{true}}$. In the
right panel the deviation of the retrieved and the true profile $\vec{x}_{\text{true}}$ are shown
(in percent) for an *a priori* profile that is 50 % lower than the true profile.
The inversion converges to the true profile, i.e., the climatology, with an
accuracy below 4 %. Right: Deviation of a retrieved profile caused by the
use of cross sections that have been measured at 273 K rather than 293 K.

The left panel of Figure 7.2 shows the differences between two pro-
files that have been retrieved from the same SCIAMACHY measurement
but with a different *a priori* profile. The retrieved results indicate that
the inversion is almost independent of the *a priori* profile, even if the
a priori profile differs by 50 % from the true profile. To quantify the
impact of the *a priori* profiles, a maximum variability of 50 % of the
ozone climatology was assumed in the study. The right side in the
left Figure 7.2 shows an induced variability in the retrieved results of
less than 4 %. The curve progression is similar to that of the curves
obtained from the sensitivity studies with respect to albedo and the
neglect of multiple scattering.

7.5 Temperature and Background Density

Temperature changes in the atmosphere are caused by direct heating by the Sun through absorption of mainly infrared radiation, chemical heating, e.g., by ozone absorption, and by transport of air masses. The temperature variability in the upper atmosphere caused by the 11 year solar cycle was estimated to be less than 3 K (McCormack and Hood, 1996), and seasonal temperature variability at 50 km are in the range of 30 K (Nagatani and Rosenfield, 1993). The mean latitudinal variability is less than 20 K, and diurnal changes are between 5 K to 9 K at 60 km (Hoxit and Henry, 1973). Thus the maximum variability of the temperature used for the following sensitivity study was set to 20 K.

The temperature[5] affects the inversion in two ways. The first is due to the temperature sensitivity of the ozone cross sections (see Section 3.4). The second effect is through the derivation of the air densities from the ideal gas law.

The applied GOME FM cross sections are tabulated for temperatures from 202 K to a maximum of 323 K in steps of 20 K. The right panel of Figure 7.2 shows the differences in retrieved profiles caused by using a different table of cross sections. At higher altitudes, no large impact of the temperature specification is observable, whereas at lower altitudes deviations of up to 4 % are apparent. This is due to the fact that the atmosphere at lower altitudes receives more radiation at lower wavelengths, and the corresponding ozone cross sections at these wavelengths exhibit a stronger temperature dependence. In contrast, the weaker dependence of the cross sections at shorter wavelengths causes a relatively weaker sensitivity of the inversion at higher altitudes. The deviations also decrease at altitudes below 40 km, where the inversion becomes less sensitive due to the lack of measurement information.

To estimate the temperature dependence due to air density variability, the accuracy of the densities was estimated at 5 %. The effect

---

5 The temperature climatology employed in the evaluated inversion is provided by a compilation from several monthly and latitudinal resolved models and observations (Nagatani and Rosenfield, 1993).

caused by a decrease of the air density is illustrated in the left panel
of Figure 7.3.
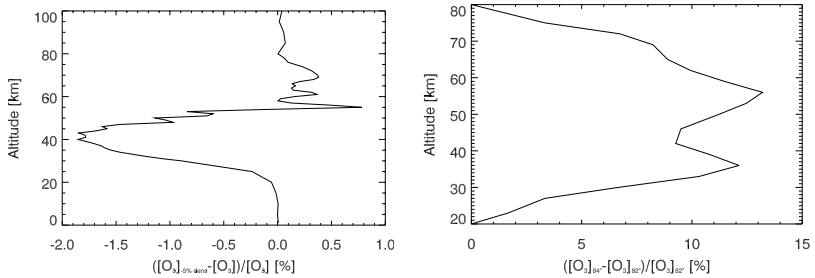
Figure 7.3: Left: Deviations due to a decrease of the air density of 5 %. Right:
Deviation of a retrieved sample profile caused by changing the measurement
specification of the solar zenith angle at 84° by 2°.

The errors due to inaccurate specified densities are quite small.
They reach only 2 % at 40 km and decrease towards lower and higher
altitudes, again due to the decreasing sensitivity of the profile retrieval.

7.6 Pointing Errors

One of the largest error sources for Sciamachy measurements are tan-
gent height errors. The design of the Sciamachy instrument provides
an accuracy of 0.061° for the elevation angle (Schwab et al., 1996),
this corresponds to about 3.4 km at the tangent point.[6] Thus the com-
monly noted uncertainty of the tangent height is within the designed
and expected error specification and the tangent height problem is a
problem of the instrument design. The instrument itself works within
the expected errors. However, some additional problems caused by
an inaccurate orbit propagator model of the spacecraft Envisat (see

---

6 All instruments on board Envisat are affected by the inaccuracy of Envisat's
  attitude. For every instrument an own tangent height retrieval is performed,
  e.g., in terms of Gomos, where this altitude is deducted from the location of the
  stars. Mipas measurements are also affected by incorrect tangent heights, but
  with an opposite sign than Sciamachy. They employ retrieved pressure profiles
  to fit the correct tangent heights (von Clarmann et al., 2003).

Section 6.1) have been solved, e.g., an inconsistent coordinate system for the on-board and on-ground program codes. Other problems are known, but not yet solved. Compared to other instruments, e.g., OSIRIS, SCIAMACHY's tangent height inaccuracy is quite large. Von Savigny (2002) quantified the error in the tangent height attitude of the OSIRIS instrument to be less than 200 m and concluded that the induced error in the retrieved ozone profiles is negligible.[7]

It has already been shown, that the background density does not have a large impact on the retrieved profiles. Therefore, the tangent height error should only cause a vertical shift of the ozone profiles. Sample profile retrievals showed that the inversion algorithm sometimes diverges due to a large tangent height error. Therefore this error is difficult to estimate and may lead to unrealistic ozone profiles.

A sensitivity study at a sample profile retrieval was carried out by comparing profiles retrieved from measurements that are adjusted with a tangent height error of 2.5 km (left panel in Figure 7.4) and 0.5 km (right panel in Figure 7.4). A tangent height change, e.g., of 2.5 km, causes an error in the retrieved profiles of about 80 % between 45 km and 55 km altitude.
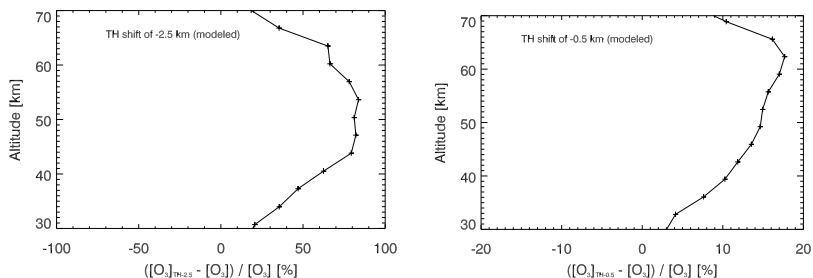
Figure 7.4: Modeled errors due to a tangent height shift of -2.5 km (left) and 0.5 km (right)

---

7 These errors are now known to be about 1 km (private communications with C. von Savigny).

The increasing error at higher altitudes is due to a decreasing ozone scale height at higher altitudes. When TRUE is applied, the tangent heights can be determined to within 0.5 km, usually with a precision of 0.3 km (von Savigny et al., 2004). A residual error of 0.5 km leads to errors in the retrieved profiles up to 20 % above 60 km, and is still the largest error source.

7.7 Solar Zenith Angles

A complete SCIAMACHY limb measurement consists of a vertical and a horizontal scan. This horizontal scan lasts about 1.5 s and covers 960 km horizontally at the tangent point.[8] The angles at the tangent point in the SCIAMACHY measurement data are stated for the left side, for the right side, and for the center of the swath. The center angle specification in the SCIAMACHY measurement data is taken for the inversion.

The solar zenith angle, as well as the solar azimuth angle, varies by about 2° along the swath. The solar zenith angle has a significant impact on the retrieved ozone concentrations, in contrast to the solar azimuth angle. The different impact of both angles is due to the fact that air masses only vary strongly with the solar zenith angle, but not with the solar azimuth angle.[9]

The induced differences of the retrieved profiles from measurements at a solar zenith angle of 50° (Figure 7.3) are less than 0.7 %, and the differences for measurements at 84° are between 9 % and 14 %, depending on the altitude. A solar zenith angle of 84° for the study is chosen because it represents a worst case scenario.

---

8 See Section 2.2 for the geometry at SCIAMACHY limb measurements.

9 The small impact of the solar azimuth angle variability of 2° has been demonstrated, e.g., in inversions of stratospheric ozone profiles (von Savigny, 2002).

7.8 Spatial Stray Light

Van Soest (2005) investigated stray light at tangent heights above 65 km that originates from outside SCIAMACHY's field of view.[10] This effect was already observed in measurements with OSIRIS where the contribution of the spatial stray light to the expected radiances reaches 440 % at 70 km tangent height and 700 nm wavelength (Llewellyn and Gattinger, 1998). Llewellyn and Gattinger (1998) found the observed stray light contribution to the in-field signal at 400 nm to be 18 % at 40 km tangent height and 65 % at 70 km tangent height.

For an estimate of the stray light contribution at SCIAMACHY measurements, van Soest (2005) assumed the stray light to be due to scattered light from outside the field of view. Actually, they neglected emissions as a possible source. Van Soest (2005) demonstrates that radiances at longer wavelengths also exhibit larger stray light contributions and concludes that the presume of spectral fingerprints in the stray light indicates that it originates partly from the lower part of limbs of the atmosphere. There was no indication that the stray light is due to holes in the instrument. However, the first channel of SCIAMACHY was not supposed to be affected as strongly as other channels. The second channel, at 70 km tangent height, exhibits stray light contributions approximately five to ten times larger than the expected signal.

In this section, the effect of SCIAMACHY's stray light on the inversion is investigated. As a first step, the contribution of stray light to the expected radiance determined from the radiative transfer model SCIARAYS, on basis of a sample measurement, is estimated. The stray light at 310 nm is shown in the left panel of Figure 7.5. The stray light contribution at 78 km reaches 120 %. Stray light contributions at other wavelengths that are employed in the inversion can be seen in Figure 6.9 on page 74. The right panel of Figure 7.5 shows the induced deviation of retrieved profiles due to these increased radiances.

Although the contribution of the stray light is quite significant, i.e., 120 % or more of the in-field signal, the impact of this addition

---

10 This stray light is sometimes named 'baffle scattering'.
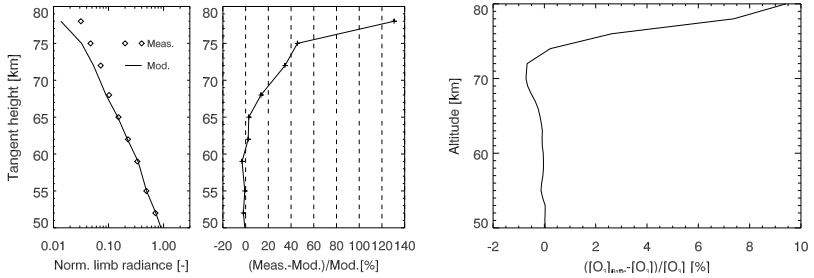
Figure 7.5: Left: Simulated and measured radiances at 310 nm which indicate a significant contribution of the stray light above 65 km. The stray light is assumed to be the difference of the measured and the modeled radiances. Right: Induced differences of retrieved ozone profiles due to the estimated stray light.

scattering on the profile retrieval is quite small due to the decreasing sensitivity of the inversion technique. The induced errors never exceed 1 %, at least at altitudes below 75 km. Above 75 km, the impact of the large stray light contributions is significant, but the decreasing sensitivity prohibits a diverging fit. In sum, it can be stated that stray light has no large impact on the inversion below 65 km. Above 65 km, the impact is quite large but is not important for the inversion used here, thanks to the strongly decreasing sensitivity of the retrieval technique.

7.9 Summary

Table 7.1 presents an overview of the results from the sensitivity studies. As already mentioned in the introduction to this chapter, the stated specifications are not statistical errors. They are rather a calculated estimate.

Albedo, multiple scattering, and the choice of the *a priori* profile are not important for the inversion. Since cross sections and the background densities are temperature dependent, their inaccurate specification leads to errors of less than 4 %. Due to their wavelength dependence in general this error decreases towards higher altitudes. In particular, the small impact of the *a priori* is a satisfactory proof of the capability of the evaluated methodology.

Table 7.1: Summary of the sensitivity studies in %

Altitude [km]	35	39	45	51	57	65
Albedo[a]	2.0	1.0	0.1	<0.01	<0.01	<0.01
Scattering modes[b]	2.3	0.8	0.2	<0.02	<0.02	<0.02
A priori[c]	5.0	1.0	3.0	2.5	3.0	7.0
Cross sections[d]	4.0	5.1	4.0	2.5	0.2	0.1
Background density[e]	1.6	1.9	1.8	0.9	0.1	0.2
Pointing errors[f]	5.0	9.6	15.5	13.5	16.5	19.0
Solar zenith angle[g]	14.0	11.0	10.5	12.5	13.2	9.0
Total Error (1σ)	16.5	15.7	19.5	18.8	21.3	22.2

[a] $A=0 \rightarrow A=1$ [b] Negl. twice scatt.   [c] 50 %   [d] 20 K   [e] 5 %   [f] 0.5 km   [g] $84° \rightarrow 86°$

8 Validation

In this section, comparisons of the retrieved ozone profiles with ozone profiles from MIPAS, HALOE, and the Radiometer for Atmospheric Measurements (RAM) observations are presented.

MIPAS profiles for the year 2003 are used to validate the retrieved ozone profiles up to 50 km. In general, collocated profiles agree within 10 % to 15 %, with the tendency of being to overestimate at altitudes between 40 km and 50 km, and there is a small systematic overestimation at 46 km in the tropics and mid-latitudes. The origin of the deviations is most likely due to the tangent height misregistration of the SCIAMACHY measurements.

HALOE profiles had to be photochemically corrected to match the conditions at the corresponding SCIAMACHY measurement. A statistical report of the error propagation due to the modeling is given. Monthly averaged comparisons between HALOE and SCIAMACHY profiles in 2004 show a slight overestimate between 40 km and 50 km. Above 50 km collocated profiles agree fairly well with each other, although recent published findings show that the HALOE VERSION 1.9 overestimates the true ozone concentration above 50 km.

Ozone profile measurements with the ground-based instrument RAM are used to make a statistical study of coincident profiles between 35 km and 55 km above Spitsbergen. A disadvantage of ozone profiles from the RAM instrument is their relatively poor vertical resolution, but the comparisons agree quite well. It was also determined that there is a slight overestimate between 40 km and 50 km altitude, but the effect is less than 10 %.

These first validation results show that the profiles retrieved from SCIAMACHY agree quite well but there is a tending to be too high, by about 10 % to 15 %, in the altitude range between 40 km and 50 km.

More validations are needed to draw a reliable conclusion about the profile quality above 50 km as the comparisons with HALOE profiles are strongly affected by the correction of the HALOE ozone concentration to the local time of the corresponding SCIAMACHY measurements.

8.1 Validation with MIPAS Profiles

The ozone profiles used for the first comparison were retrieved from measurements with the MIPAS instrument,[1] and that were processed at the Institut für Meteorologie und Klimaforschung (IMK) (von Clarmann et al., 2001, 2003, and references therein). For this profile retrieval from mid-infrared measurements, an analysis is made with a set of confined spectral regions, so called micro windows, between 8.6 μm and 14 μm. The selection of the micro windows depends on the altitude, the location, and meteorological conditions. Least Square fits were applied to match up to ten emission lines (Glatthor et al., 2005).

The current MIPAS (IMK) ozone profiles provide an altitude coverage from 20 km to 68 km and have been compared to stratospheric SCIAMACHY (von Savigny et al., 2005b) and GOMOS (Kyrölä et al., 2004) observations for one month (Bracher et al., 2005). In terms of stratospheric SCIAMACHY ozone profiles, the concentrations agree within 10 % in the altitude range from 22 km to 35 km, and for about 8 km above this altitude range are within 20 %. For GOMOS the agreement of the compared profiles, up to an altitude of 60 km, is within 5 % to 10 %. MIPAS and POAM III (Lumpe et al., 2003) ozone profiles between 20 km and 50 km show agreement within 10 % (Steck et al., 2006). Steck et al. (2006) showed further comparisons with several LIght Detection And Ranging (LIDAR) and ozone sonde measurements. In general the MIPAS ozone profiles from IMK are well validated between 20 km and 50 km and agree with the observations from all compared instruments, there is a slight underestimate between 40 km and 50 km.

MIPAS's field of view is 30 km horizontally and 3 km vertically, while

—————————

1 See Appendix A for a description of the MIPAS instrument.

Sciamachy's horizontal field of view is about 960 km across track, about 500 km along track and about 3 km vertically. Thus the Sciamachy profiles are an average over a wide horizontal range. As the number of coincident Sciamachy and Mipas profiles is very large, both instruments are on the same spacecraft Envisat, the spatial radius of the coincident observations can be chosen to be quite small, 100 km or 200 km. Although this criterion is quite narrow, the number of collocations is still large enough for statistics that require at least several tens or hundreds of collocations. An additional restrictive condition is that the difference of the respective solar zenith angles is less than 2°. This ensures that only profiles that are obtained at nearly the same local time are compared. This is important at higher altitudes due to the diurnal variation of the ozone concentrations.

Mipas ozone data for 2003 were used for comprehensive comparisons since they are the only available data.[2] Sciamachy measurements were affected by a large tangent height error in 2003, even after the application of the tangent height retrieval True. Although this error limits the validation statistics, the agreement of the collocated Mipas and Sciamachy ozone profiles is within about 10 %.

8.1.1 Monthly Averages

Figure 8.1 shows the averaged differences between collocated Sciamachy and Mipas ozone profiles for different months in 2003. Due to the Sciamachy data gap no comparisons are shown between June and August. The collocation radius is 200 km and the number of collocated profiles varies between 14 and 365 per month.

In general, the mean agreement is within 10 %. An overestimate above 45 km and an slight underestimate below 40 km can be seen in some months. The slight overestimate above 45 km is in agreement with the above noted underestimate of the Mipas (Imk) profiles in comparison to Poam, Lidar and ozone sonde observations (Steck et al., 2006). The Sciamachy ozone profiles appear to be more re-

---

2 The Mipas instrument provided measurements only until December 2003 when the mounting of one mirror of the Fourier transform spectrometer was blocked.
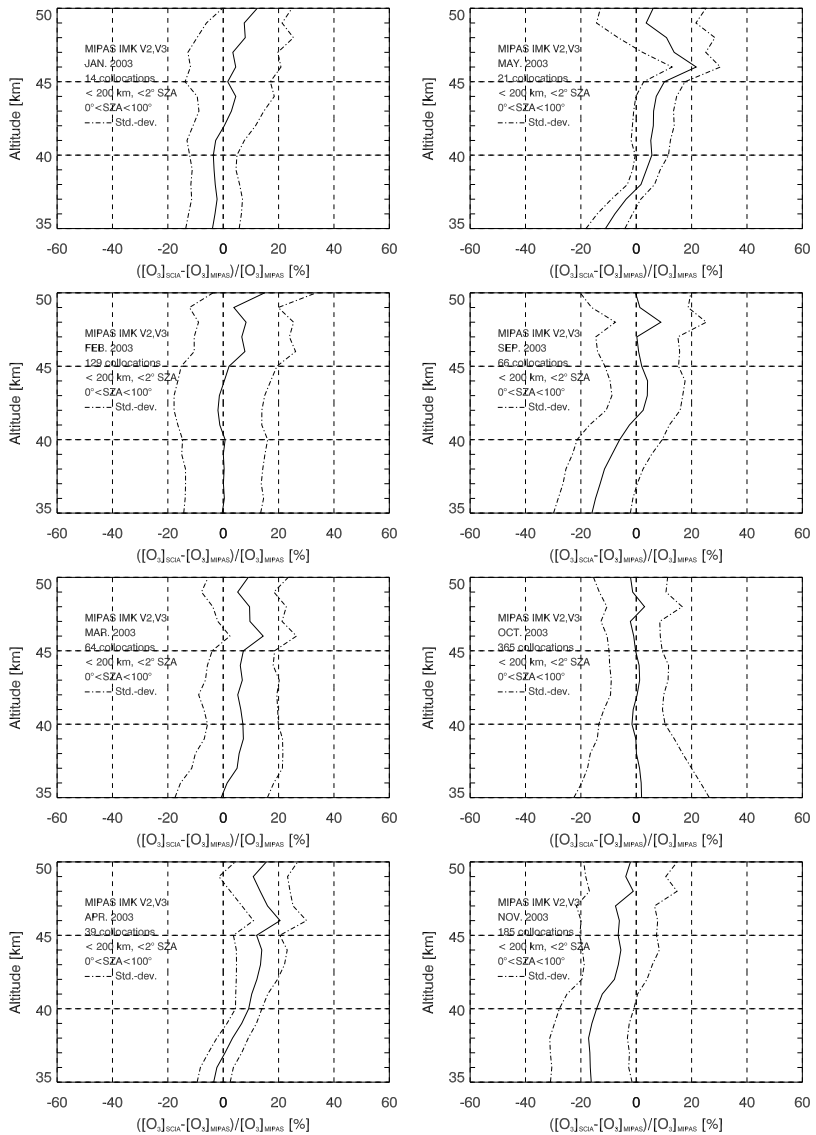
Figure 8.1: Statistics for monthly averaged comparisons with collocated ozone profiles from Mipas (Imk) in 2003. The solid lines indicate the mean differences and the dashed lines the respective standard deviations.

alistic than the Mipas profiles in this altitude range. The standard deviation is less than 10 % to 15 % which is a fairly good value considering the wide swath associated with the Sciamachy field of view.

8.1.2 Dependence on the Solar Zenith Angle

Figure 8.2 shows the monthly averaged comparisons of collocated Sciamachy and Mipas profiles for different solar zenith angles. Relatively poor profile retrievals at larger solar zenith angles, i.e., at less sunlight, are expected.[3] However, comparisons of the profiles from the measurements reveal the opposite behavior.[4]

Deviations are larger at higher altitudes. A possible explanation for this is the relatively large profile error induced by the tangent height offsets at higher altitude due to the decreasing ozone scale height. The standard deviations increase at larger solar zenith angles, in agreement with the finding of a better inversion fit at smaller solar zenith angles.

A slight systematic overestimate at 46 km altitude for small solar zenith angles is observable, but this is mostly in the tropics and at mid-latitudes. This could be due to the fact that the measurements for the tangent height retrieval True are taken from the tropics but the full reason for this is still unknown.

8.1.3 Dependence on the Latitude

To determine a possible latitudinally dependent systematic error in the profile retrieval, monthly averaged comparisons have been made for five different latitude bands (Figure 8.3 and Figure 8.4). Due to a lack of collocations in some latitude bands the collocation radius has been expanded to 500 km, which lowers the agreement.

Relatively large differences are observable in the southern polar re-

---

3 This is more or less true depending on the direction of the field of view with respect to the Sun. There are many other aspects but in general this statement is correct. At least profile retrievals above 85° solar zenith angle lead to unrealistic ozone profiles.

4 Although even here the averaged differences are within 10 %.
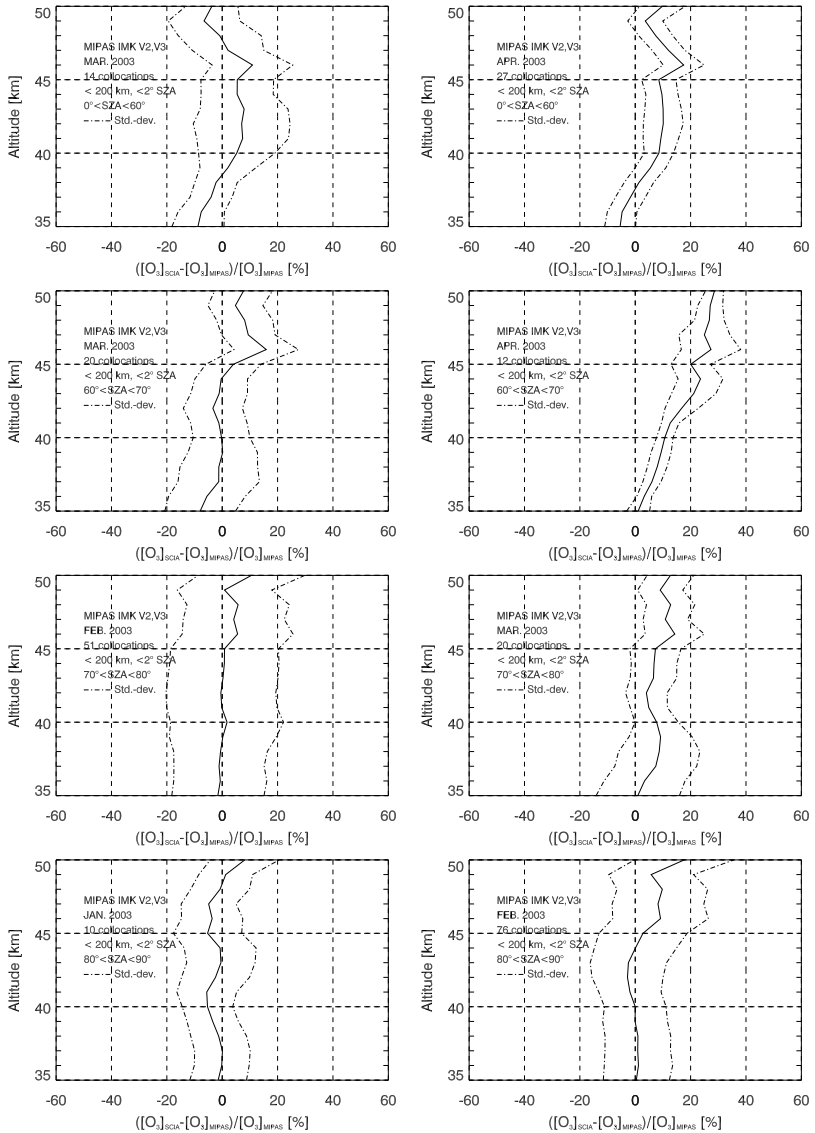
Figure 8.2: Statistics for monthly averaged comparisons with ozone profiles from Mipas (Imk) at different solar zenith angles in spring 2003. Months in the same season have been taken due to better comparability.
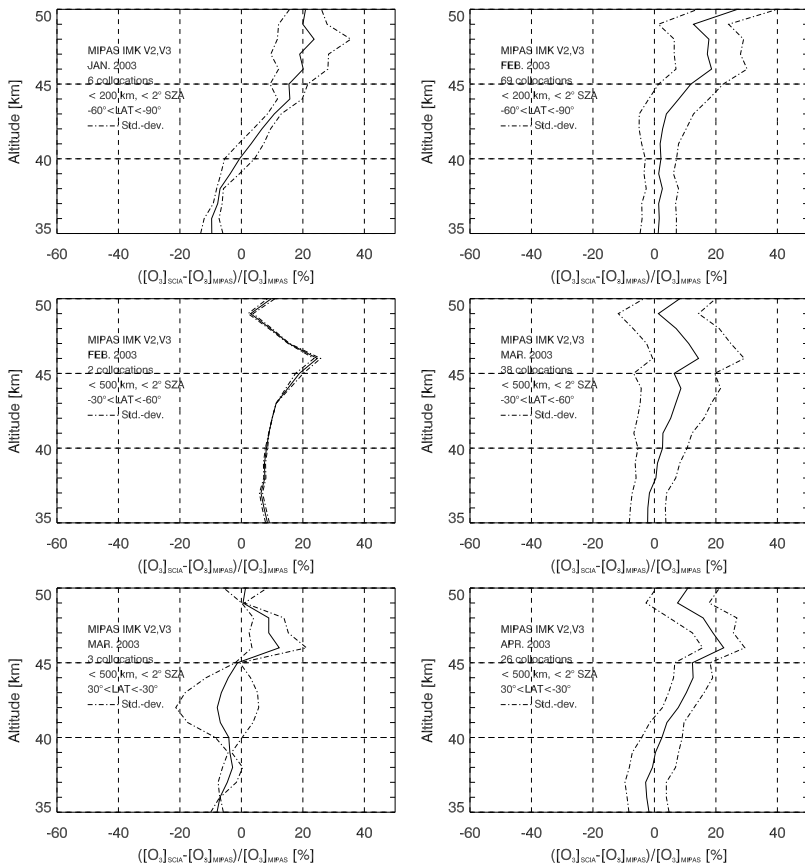
Figure 8.3: Statistics for monthly averaged comparisons with ozone profiles from MIPAS (IMK) in the southern polar region (top), southern mid latitude (middle), and in the tropics (bottom).
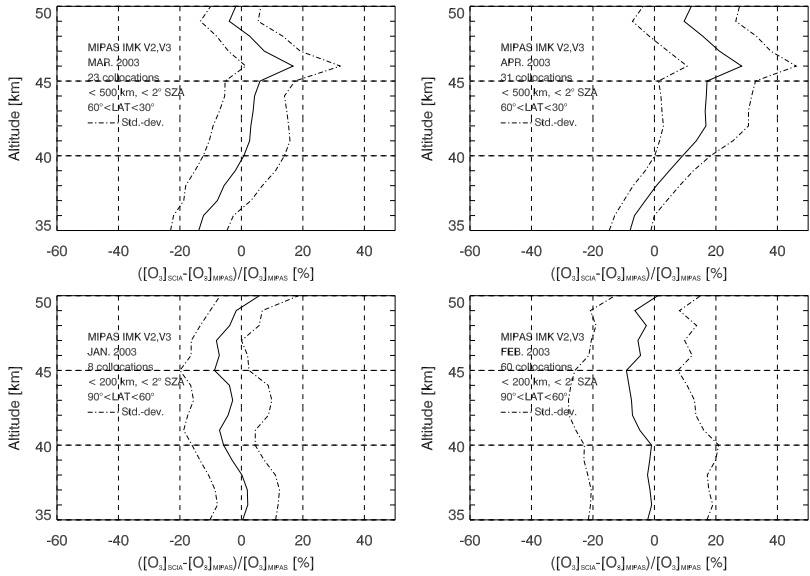
Figure 8.4: Statistics for monthly averaged comparisons with ozone profiles
from MIPAS (IMK) in the northern mid latitude (top) and in the northern
polar region (bottom).

gion above 45 km and increasing differences at higher altitude can be
seen due to the relatively large effect of the tangent height offset. The
comparisons are not as good as those shown in Figures 8.1 and 8.2.
This could be due to the fact that the tangent height offsets are de-
rived only once on each orbit[5] and therefore have a different quality
at different measurement locations. Another puzzle is the irregularity
of the comparisons at 46 km, which is only significant in the mid-
latitudes and tropics, but a possible relation to the tangent height
retrieval is still unclear.
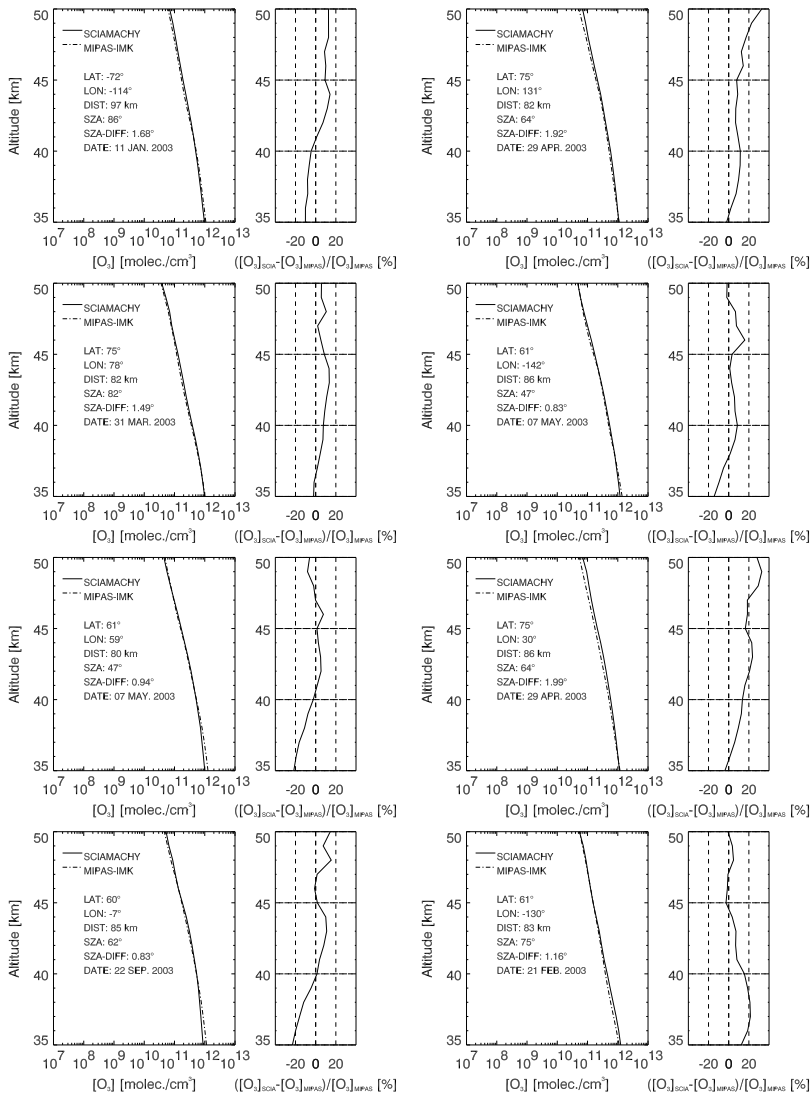
Figure 8.5: First set of eight sample comparisons of coincident Sciamachy and Mipas (Imk) profiles within a collocation radius of 100 km and a maximum solar zenith angle difference of 2°. Examples have been chosen arbitrarily.
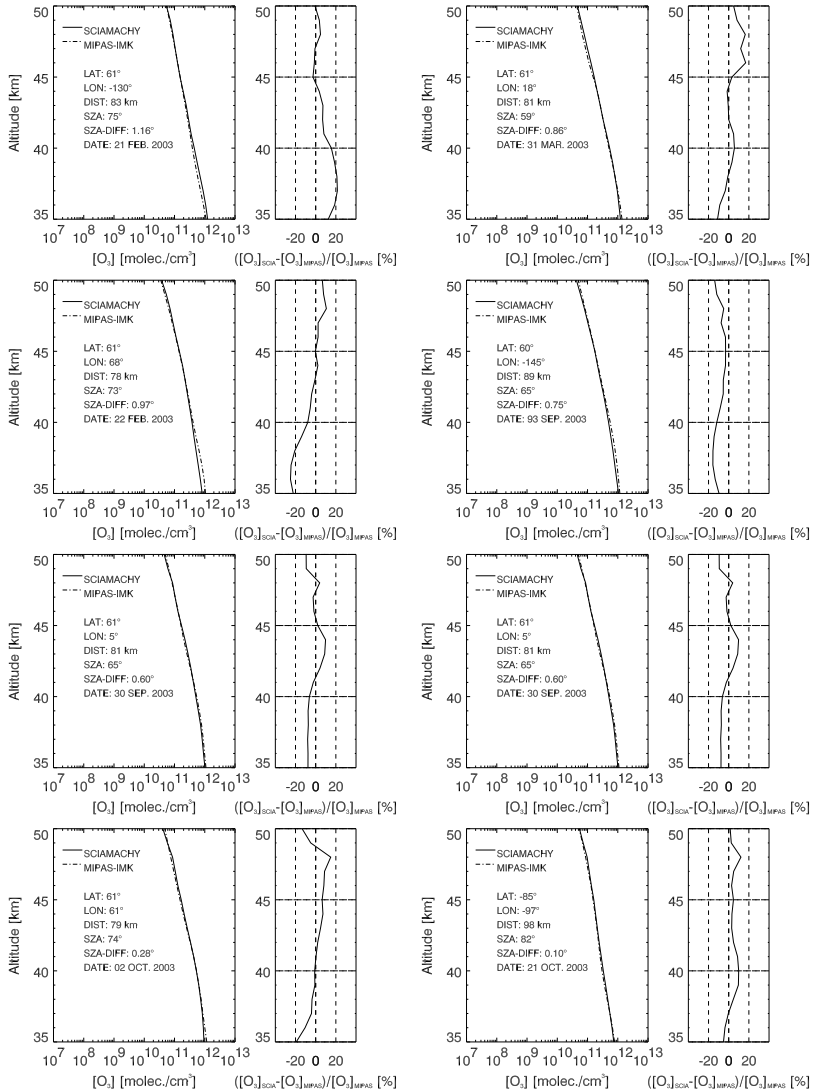
Figure 8.6: Second set of eight sample comparisons of coincident Scia-
machy and Mipas (Imk) profiles within a collocation radius of 100 km and
a maximum solar zenith angle difference of 2°. Examples have been chosen
arbitrarily.

8.1.4 Sample Profile Comparisons

Figure 8.5 and Figure 8.6 show some comparisons of coincident sample ozone profiles within a collocation radius of 100 km. The differences of the corresponding solar zenith angles are denoted in the caption of the figure.

8.2 Comparisons with HALOE Profiles

8.2.1 HALOE on UARS

HALOE (Russell et al., 1993) is one of the most cited instruments for polar ozone observations. The popularity of HALOE is due to the public interest in current global observations of the polar ozone decrease in general, but it is also due to the fact that HALOE provided one of the first reliable global observations of ozone distributions.[6]

HALOE on board the Upper Atmosphere Research Satellite (UARS) was launched in September 1991, into a 585 km circular orbit with 57° inclination, and was switched off on 31 December 2005. Solar occultation measurements over an altitude range between 15 km and 130 km provide a vertical resolution of 2.3 km with a coverage from about 80° S to 80° N during the course of the year. Spatially highly resolved measurements have been made in the polar region. About 30 occultation measurements occurred each day at sunrise and sunset in both hemispheres, respectively.

HALOE ozone profile retrievals and validations were quite successful (Brühl et al., 1996); 9.6 μm ozone absorption lines were employed for the profile retrievals. Brühl et al. (1996) validated these measurements with numerous sounder, including ozone sondes, LIDARs, balloons, rocketsondes, and other satellites; the HALOE ozone profiles

---

5 Strictly speaking up to six measurements, in the latitude band between 20° N and 20° S are taken in TRUE and are averaged to one offset value for the whole orbit.

6 The public interest has become considerable since Farman et al. discovered a deep total ozone minimum over Halley Bay in the beginning of the 1980s (Farman et al., 1985).

between 16 km to 38 km agree to within 5 % but with a tendency for a low estimate. These findings have also been confirmed by validations against the Poam and Mls observations (Rusch et al., 1997).

The current retrieval Version 1.9 provides ozone profiles up to 70 km. Validations of Haloe profiles up to 50 km are in excellent agreement with Sage ii ozone measurements, but there is a large systematic overestimate of up to 15 % or 20 % above 50 km (Nazarayan et al., 2005). The impact of twilight gradients on this inversion was demonstrated a few months after the Sage ii validation study (Natarajan et al., 2005). Solar occultation measurements face difficulties if sharp gradients are present in the species concentrations near sunrise and sunset conditions;[7] photochemically induced variations introduce asymmetries in the species distribution along the line of sight. Thus correction factors were routinely derived from photochemical model calculations and were applied to a number of sample inversions. With this, Natarajan et al. (2005) proved that the neglect of mesospheric twilight variations in ozone leads to more than 20 % overestimation at an altitude of 61 km. Additionally, strong differences in the photochemical correction factors for sunrise and sunset measurements were found. However, the findings indicate that for the Haloe Version 1.9 ozone profiles there is in general an overestimate above 50 km.

8.2.2 Photochemical Correction of Solar Occultation Observations

The local time differences between Haloe and Sciamachy measurements are usually considerable. Since Haloe measurements were performed during sunrise and sunset, they are affected by the strong diurnal variation of ozone. Sciamachy measurements are mostly made at about 10:00 Lt in the morning.[8] Collocated Haloe and Sciamachy

---

7 Solar occultation measurements are performed at a solar zenith angle of 90° which corresponds to the absolute minimum of ozone concentrations, as seen in Figure 3.2.

8 See also Figure 2.1 for the Sciamachy overflight times. Measurements with other local times are also possible.

observations are mainly between $70° N$ and $70° S$ with more occurrences at higher latitudes. To compare solar occultation observations with limb observations from SCIAMACHY, the local times of the measurements have to be approximately the same. For the present validation study, HALOE profiles have been converted to the solar zenith angle of the corresponding SCIAMACHY measurement using a photochemical model.

Figure 8.7 shows an example of the differences of ozone concentrations due to a shift of the solar zenith angle from the solar zenith angle of the HALOE measurement to that of the corresponding SCIA-
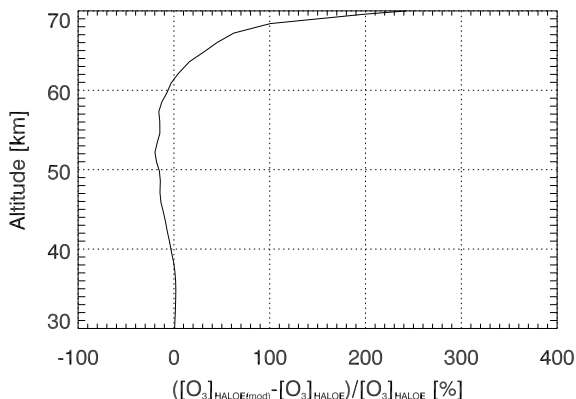
Figure 8.7: Relative differences between a HALOE sample ozone profile – photochemically corrected to $74°$ – and the original HALOE profile taken at a solar zenith angle of $90°$. The HALOE measurement was taken on 6 March 2003 at 18:33 UTC.

MACHY measurement. The ozone concentrations at $74°$ from a sample HALOE measurement were derived from a one dimensional version of SLIMCAT (Chipperfield, 1999). The photochemically corrected profile exhibits differences of up to 20% below $60\,km$ and up to several hundred percent above $60\,km$. Since the ozone concentrations are lowest at a $90°$ solar zenith angle,[9] the higher ozone concentrations above $60\,km$ are as expected. Below $60\,km$ the ozone concentrations during

---

9 See the diurnal variability of ozone concentrations in Figure 3.2, especially the ozone concentration at about 10:00 LT.

daytime are in general higher than at sunrise and sunset. However, the model derives the ozone concentrations corresponding to the same solar zenith angle, an angle at which the Sciamachy measurement was performed with a certain error. This error must now be estimated.

For this purpose, an investigation of the error propagation due to error sources in the model was made. The four most important model parameters were varied to infer the corresponding model results of ozone concentrations. These parameters are the initial ozone profiles, water vapor profiles,[10] and also the temperature and pressure profiles.[11]

Figure 8.8 shows the differences in ozone concentration caused by the assumed variation of one of the aforementioned parameters. The accuracy of the initial ozone and water profiles have been estimated to be $10\,\%$, temperature $10\,\mathrm{K}$, and pressure $1\,\%$. The impact of both negative as well as positive change of the respective parameter is shown.

Changes of the initial ozone profile cause smaller errors at higher altitude in contrast to the changes due to H_2O and temperature. In contrast to that, HO_x, which is mainly produced by H_2O, plays a major role in determining the chemistry of the mesosphere. Temperature has a large impact on the model as most of the reaction rates are temperature dependent.

Table 8.1 shows an overview of the error sources in the model. The $1\,\sigma$ propagation error of the model is between $10.7\,\%$ and $17.5\,\%$. An additional dependence on the solar zenith angle is not considered here, and therefore Table 8.1 is only an estimate.

Uncertainty in the original Haloe profiles as well as the model errors in Table 8.1 result in the total reasonable uncertainty ($1\,\sigma$ propagation was considered) for the modeled Haloe profiles (Table 8.2).

---

10 Water profiles were also taken from collocated Haloe measurements.

11 See a description of the Slimcat model for the origin of the different parameters (Chipperfield, 1999).
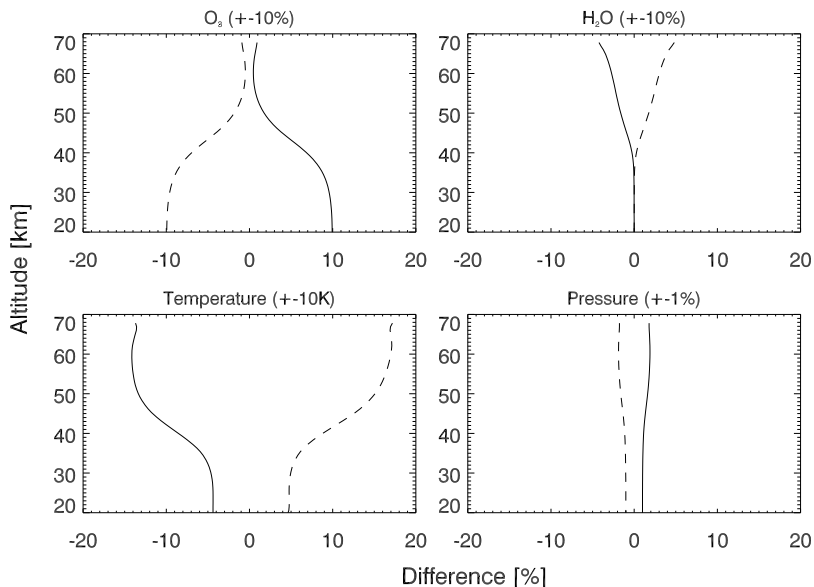
Figure 8.8: Error propagation due to a change of O_3 ($\pm 10\,\%$), H_2O ($\pm 10\,\%$), temperature ($\pm 10\,K$), and pressure ($\pm 1\,\%$) due to a solar zenith angle correction from $90°$ to $74°$. The dashed line indicates the difference due to a negative change of the parameter, whereas the solid line indicates the changes due to a positive change of the respective model parameter. Courtesy of H. Winkler.

Table 8.1: Summary of the error sources in the model used for the photochemical corrections in percent. Only the changes due to a negative change of the respective model parameter are shown in this table.

Altitude [km]	35	39	45	51	57	65
O_3 ($-10\,\%$)	-8.7	-7.3	-3.8	-1.5	-0.6	-0.7
H_2O ($-10\,\%$)	<0.1	0.2	1.0	1.9	2.6	3.9
Temperature ($-10\,K$)	6.1	8.3	12.7	15.4	16.7	17.0
Pressure ($-1\,\%$)	-1.1	-1.1	-1.4	-1.7	-1.8	-1.8
Total Error ($1\,\sigma$)	10.7	11.1	13.4	15.7	17.0	17.5

Table 8.2: Summary of uncertainties for Sciamachy and Haloe ozone profiles in percent. The uncertainty of the Haloe profiles is estimated.

Altitude [km]	35	39	45	51	57	65
Sciamachy profiles	16.5	15.7	19.5	18.8	21.3	22.2
Haloe profiles	10.0	10.0	12.0	12.0	15.0	15.0
Model[a]	10.7	11.1	13.4	15.7	17.0	17.5
Total Error (Haloe)	14.6	14.9	18.0	19.7	22.6	23.1

a On basis of negative changes of the respective model parameters.

8.2.3 Validation Results

Figure 8.9 shows three monthly averaged comparisons for the year 2004. The collocation radius is 200 km. The figures also show the standard deviations calculated from the comparisons, these are fairly large but reasonable due to the large uncertainty in the solar zenith angle corrected Haloe profiles. The comparisons show a general agreement within 20 % but with the tendency to be low at higher altitude. A slight overestimate of about 20 % is observable near 45 km. The comparisons between 50 km and 70 km show both an overestimate (July) as well as an underestimate (August and December). The latter is in agreement with the findings of Natarajan et al. (2005) that the Haloe Version 1.9 ozone profiles overestimate the ozone concentrations above 50 km by up to 20 %. Figure 8.10 and Figure 8.11 show some arbitrarily selected profile comparisons.

Although the comparisons with Haloe profiles do not provide excellent agreement with the Sciamachy profiles, they are within the expected uncertainties. The slight overestimate of Sciamachy ozone profiles between 40 km and 50 km as well as that of the Haloe profiles at higher altitude, as reported by Nazarayan et al. (2005) and Natarajan et al. (2005), can be seen. Considering the fairly large uncertainties due to the modeled correction of the solar zenith angle of the respective Haloe measurement, the compared profiles are in very good agreement.
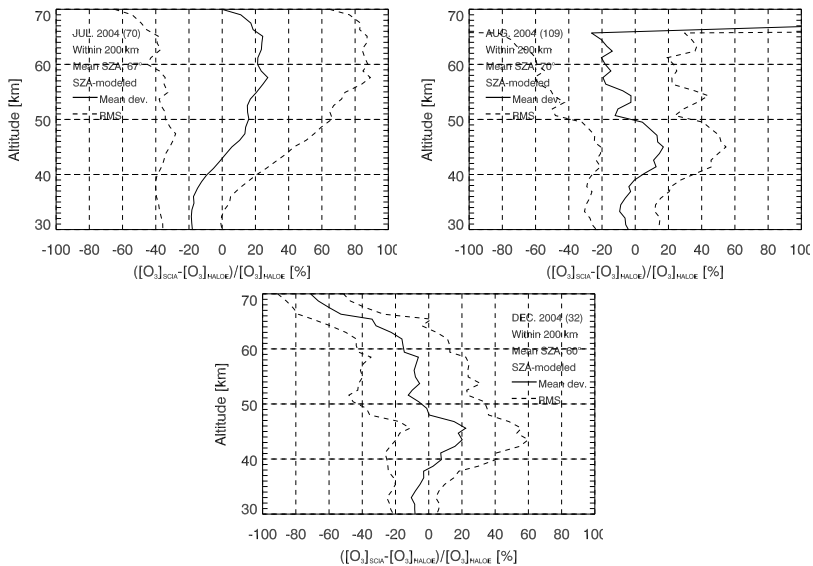
Figure 8.9: Monthly averages of profile comparisons and the respective $1\,\sigma$ standard deviations (dashed lines) using photochemically shifted Haloe sunrise measurements. The collocation radius is $200\,\mathrm{km}$. The outlier on the figure top right is due to missing Haloe data above $66\,\mathrm{km}$ in August 2004.
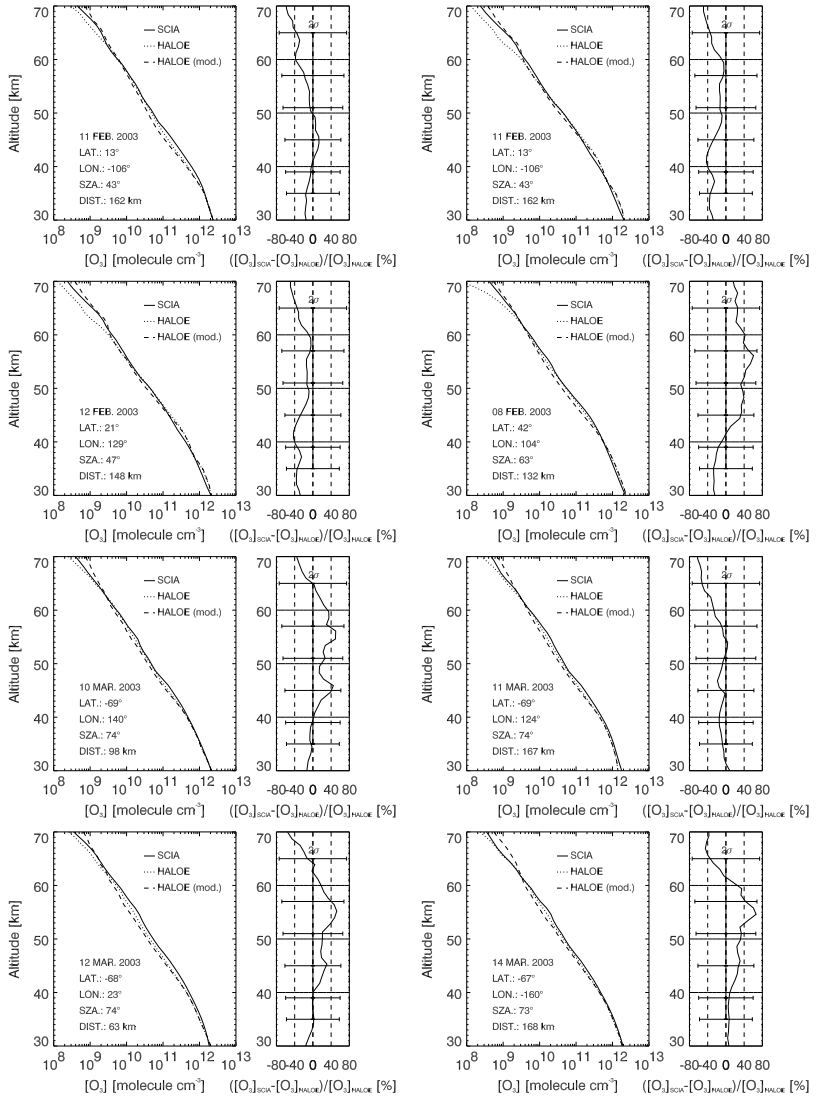
Figure 8.10: First set of eight sample profile comparisons retrieved from Sciamachy Version 2.25 and Haloe profiles Version 1.9.
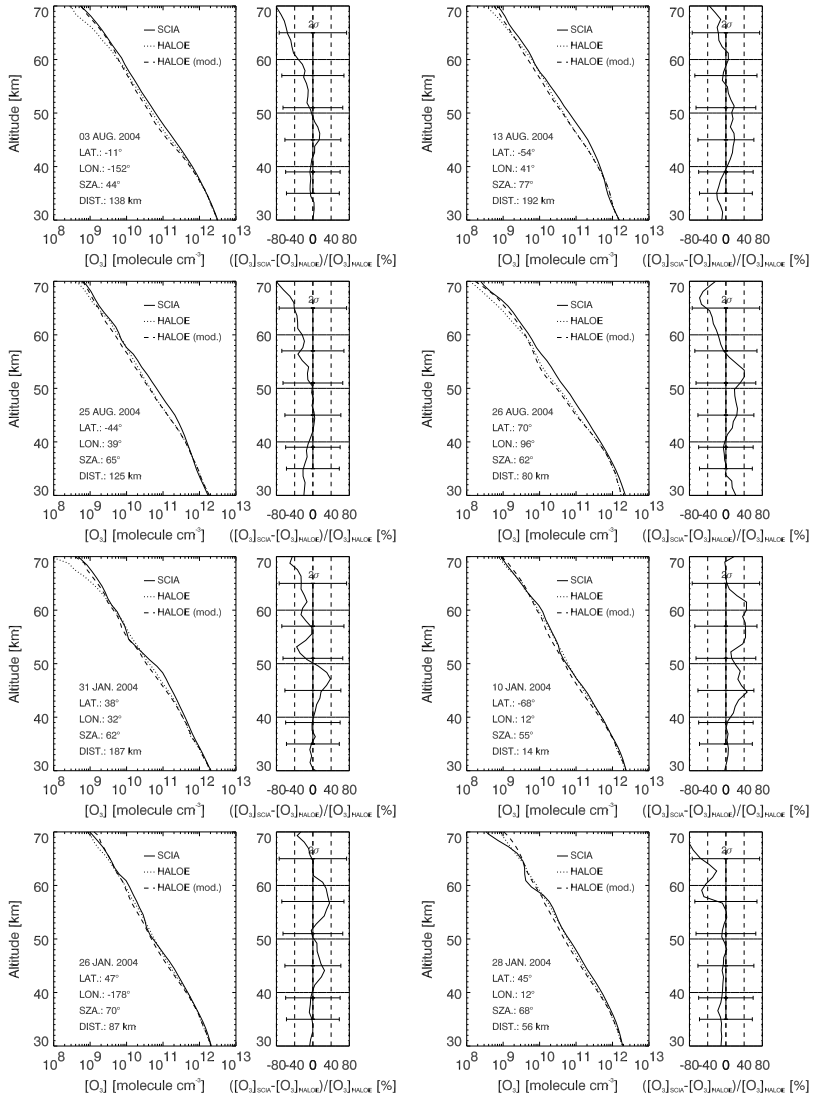
Figure 8.11: Sample comparisons of Sciamachy Version 2.25 and Haloe Version 1.9 profiles.

8.3 Validation with RAM Profiles

This section deals with validation results from the ground based Radiometer for Atmospheric Measurements (RAM) (Palm et al., 2005, and references therein) at Ny Ålesund. RAM is a millimeter-wave radiometer tuned to the frequency of an ozone transition line at 142 GHz with a bandwidth of about 1 GHz and a spectral resolution of 1.3 MHz. Spectral measurements over Ny Ålesund, Svalbard (78° N, 11° E) have been taken every thirty minutes since November 1994. Ozone profiles are retrieved using an Optimal Estimation inversion scheme. Retrieved ozone profiles provide a vertical coverage between 15 km and 55 km with a vertical resolution between 8 km and 20 km.

RAM retrieved ozone profiles are well validated by several ozone sondes in the stratosphere between 18 km and 24 km with a deviation smaller than 10 %, and with LIDAR instruments between 16 km and 34 km with a maximum deviation of 11 % (Palm et al., 2005). MLS observations of ozone are used for validation between 20 km and 55 km, these show an agreement within 10 % (Langer, 1999).

A disadvantage of the ozone profiles retrieved from the RAM instrument is the poor vertical resolution between 8 km and 20 km. SCIAMACHY profiles have therefore been convolved with the averaging kernel functions of the RAM ozone profile retrieval for comparisons.[12]

Figure 8.12 shows a statistical comparison of seven collocated SCIAMACHY and RAM measurements within a radius of 500 km. The comparisons show good agreement. Only between 40 km and 50 km are the concentrations retrieved from SCIAMACHY 10 % larger than those from the RAM instrument. The standard deviation is about 20 %.

---

12 A detailed description of this mathematical calculation of the RAM profiles can be found in Palm et al. (2005).
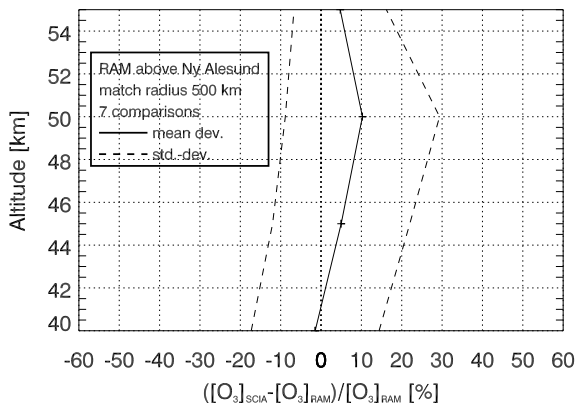
Figure 8.12: Statistical comparison of SCIAMACHY and RAM profiles over Spitsbergen

8.4 Conclusion of the Validation Studies

In general the global and monthly averaged comparisons of VERSION 2.25 ozone profiles from SCIAMACHY measurements with those from MIPAS (IMK) and HALOE (VERSION 1.9), and the RAM profiles over Spitsbergen show a good agreement between 35 km and 50 km, mostly within 10 % to 15 %. Slight systematic overestimates have been found in the altitude range 40 km and 50 km in comparison with the observations from other instruments. A systematic overestimate, with increasing altitude and an irregularity at 46 km, has been found in tropical and mid-latitude regions; this is probably due to the 'knee' tangent height error caused by the decreasing ozone scale height.

Validations with HALOE profiles between 50 km and 70 km show a general agreement that are within 10 % when recent findings of an overestimate of the HALOE VERSION 1.9 profiles are considered. Due to the need for photochemical corrections for the HALOE ozone profiles no further conclusions can be drawn.

Part III

Applications

9 First Analysis
of Sciamachy Observations

As a first application of the retrieved ozone profiles the morphology of ozone in the upper stratosphere and lower mesosphere region is presented in this section.[1] The vertical distribution of ozone is exemplified by global maps that show the upwelling tropical stratospheric ozone and a strongly radiation-driven ozone variation in the lower mesosphere.

Maps of global ozone concentrations show the extent of the seasonal variation. Besides the tropical stratospheric ozone maxima in the respective summer hemisphere a contemporaneous maximum in southern winter[2] was found. Finally, the year-on-year ozone distribution in 2002, 2004, and 2005 reveals the relative small annual variation of ozone concentrations in the upper stratosphere and lower mesosphere.

9.1 Availability of Retrieved Profiles

Figure 9.1 shows the current number of retrieved profiles from Sciamachy limb measurements for every month until the end of October 2005. Large measurement data sets have been available since beginning of 2004. Along the scheduled fourteen orbits per day, each

---

1 It is one of Sciamachy's benefits to provide global maps of trace gas concentrations at almost the same local time, which is a prerequisite for the observation of variations in gas concentrations.

2 'Southern winter' denotes the coldest months in the southern hemisphere, i.e., technically between 21 June to 23 September, and southern summer denotes the warmest months in the southern hemisphere, i.e., between 22 December and 21 March. The northern hemisphere is denoted similarly.
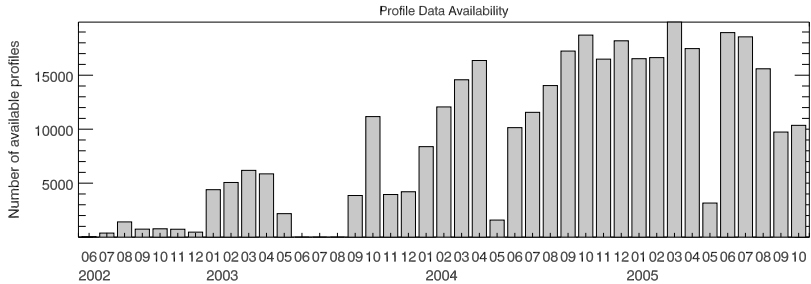
Figure 9.1: Current number of retrieved ozone profiles from Sciamachy measurements for every month up to the end of October 2005. Large data sets have been available since 2004. The data gap between June and August 2003 is caused by a broken calibration processing chain.

consisting of about 35 measurements, approximately 15 000 measurements each have been made each month. An incorrect assignment of measurements and respective orbits causes a repeated listing of the same measurement. The number of reported observations may therefore reach 20 000 in a single month, e.g., in March 2005. A data gap from June until August 2003 was caused by a broken data processing chain from level 0 to level 1 data format, which translates the raw binary data into calibrated data.[3] With the exception of May, a large data set is available in 2004 and in 2005. The large number of retrieved ozone profiles provides an excellent global coverage (see the coverage with retrieved ozone profiles in January 2004 in Figure 9.2).

Figure 9.2 also shows a data gap that is caused by the so-called South Atlantic anomaly, where a large change in the Earth's magnetic field occurs. This anomaly affects the electronic instruments in space and also impacts Envisat. Perturbed Sciamachy measurements have been rejected by an upstream algorithm that checks the shape of the limb radiance profiles, e.g., for negative radiances.

---

3 For a description of the calibration processes see Lichtenberg et al. (2005).
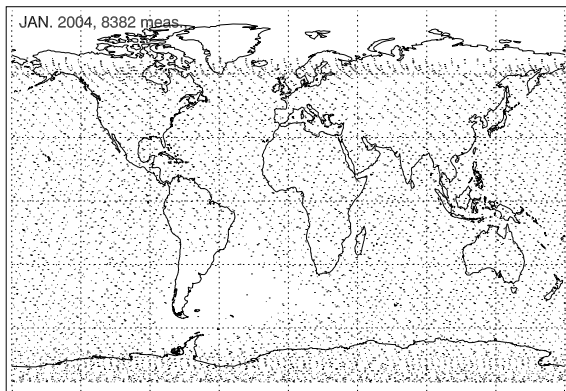
Figure 9.2: Distribution of retrieved ozone profiles in January 2004. A dot indicates the location of a retrieved ozone profile. The observations cover the northern and southern pole regions, respectively, depending on the season. Above the South Atlantic no profiles are available due to measurements affected by the local magnetic field anomaly. Affected measurements have not been evaluated.

9.2 Global Vertical Distribution

Figure 9.3 shows contours of the retrieved ozone concentrations in January 2004 at various altitudes between 35 km and 65 km. The data set includes 8382 measurements that are linearly Delaunay-triangulated (Akima, 1978) and then linearly interpolated on to a 5° spaced latitude and longitude grid. A variable color bar is used for scaling.

Upwelling tropical ozone causes a maximum between the equator and 30° S at 35 km and 40 km. In both polar regions low ozone concentrations are observed, but the effect in the northern polar region is larger. At 45 km and 50 km no large global latitudinal gradients of the ozone concentrations are observed. Even the ozone concentrations in the polar regions have almost the same order of magnitude.

This distribution changes dramatically at 55, 60, and 65 km. The ozone concentrations in the southern hemisphere decrease and increase in the northern polar region. In the southern polar regions ozone concentrations differ by several hundred percent at 65 km.

The ozone distribution displays the general photochemistry of ozone
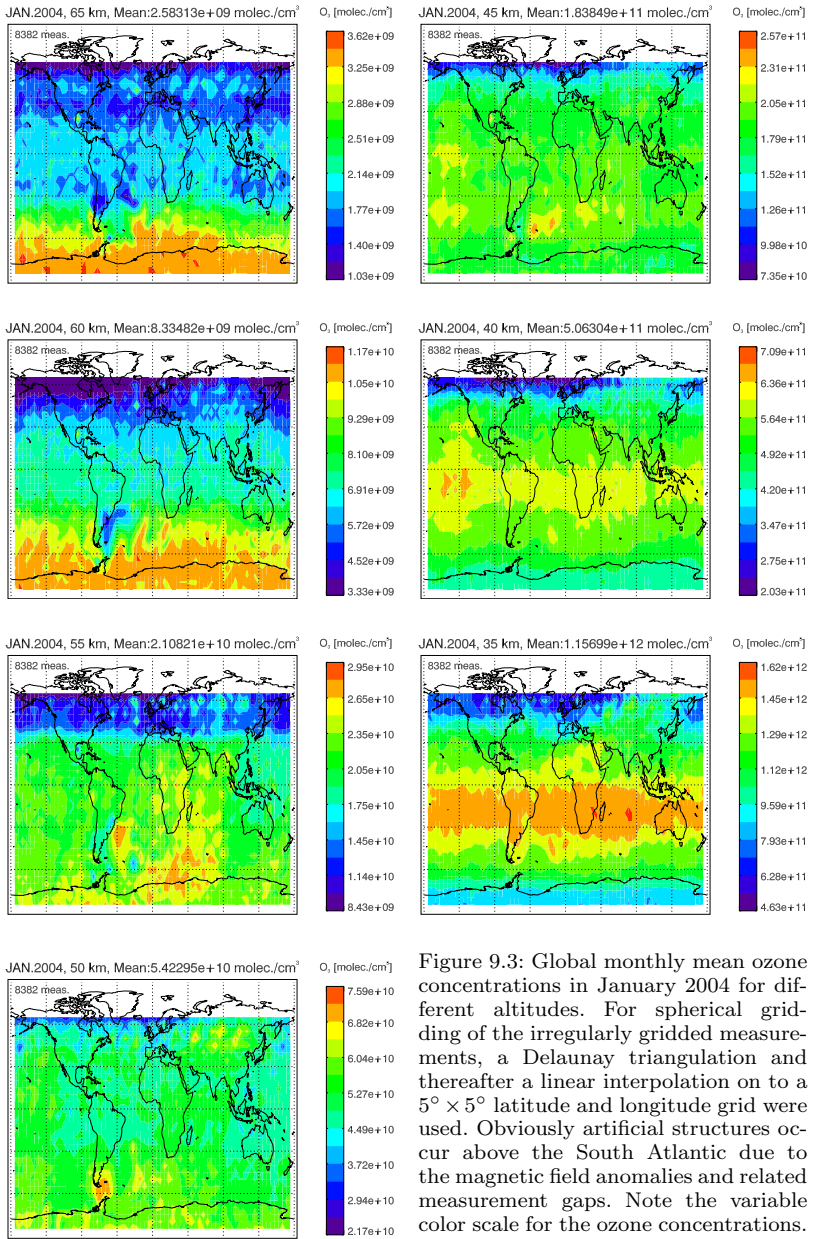
Figure 9.3: Global monthly mean ozone concentrations in January 2004 for different altitudes. For spherical gridding of the irregularly gridded measurements, a Delaunay triangulation and thereafter a linear interpolation on to a $5° \times 5°$ latitude and longitude grid were used. Obviously artificial structures occur above the South Atlantic due to the magnetic field anomalies and related measurement gaps. Note the variable color scale for the ozone concentrations.

and oxygen at different altitudes. The photochemical equilibrium is fixed by the different relation of the radiation in the Schumann-Runge bands and continuum[4] and in the ozone absorption bands.[5] Oxygen photolysis in the Schumann-Runge spectral range produces atomic oxygen and is, therefore, responsible for ozone production. Ozone photolysis in the ozone absorption bands dissociates ozone and does not change the amount of odd oxygen. At lower altitudes relatively large amounts of ozone is dissociated. Radiation in the Schumann-Runge bands is absorbed at higher altitudes. The lifetime of ozone is short at higher altitudes where ozone is strongly photolyzed by short wave radiation.

9.3 Seasonal Variability

Figure 9.4 and Figure 9.5 show the change of ozone concentrations at 40 km for each month of the year 2004. A fixed color bar is used in this representation to distinguish the absolute differences in the ozone concentrations. May 2005 is currently missing due to a lack of measurements (see Figure 9.1 on page 116).

The tropical maximum due to upwelling ozone during southern summer is not as apparent as during northern summer, where a secondary maximum during southern winter also occurs. This secondary maximum is located below Africa and drifts towards Australia extending from 30° S to 65° S in October. The establishment of this winter maximum is known as the 'collar effect'.[6] Ozone rich air is moved from the tropics to high latitudes, where it collides with the polar vortex (Schoeberl and Hartmann, 1991).[7] Inside the vortex descent rates are

---

4 Molecular oxygen is dissociated strongly in the Schumann-Runge continuum between 135 nm and 176 nm and the Schumann-Runge bands between 176 nm and 192.6 nm.

5 The ozone absorption band consists of mainly the Hartley, the Huggins, and the Chappuis bands.

6 The effect is named so due to the fact that the ozone is accumulated all around the polar vortex and observations look like a collar.

7 The polar vortex is a persistent, large-scale cyclone located near the Earth's
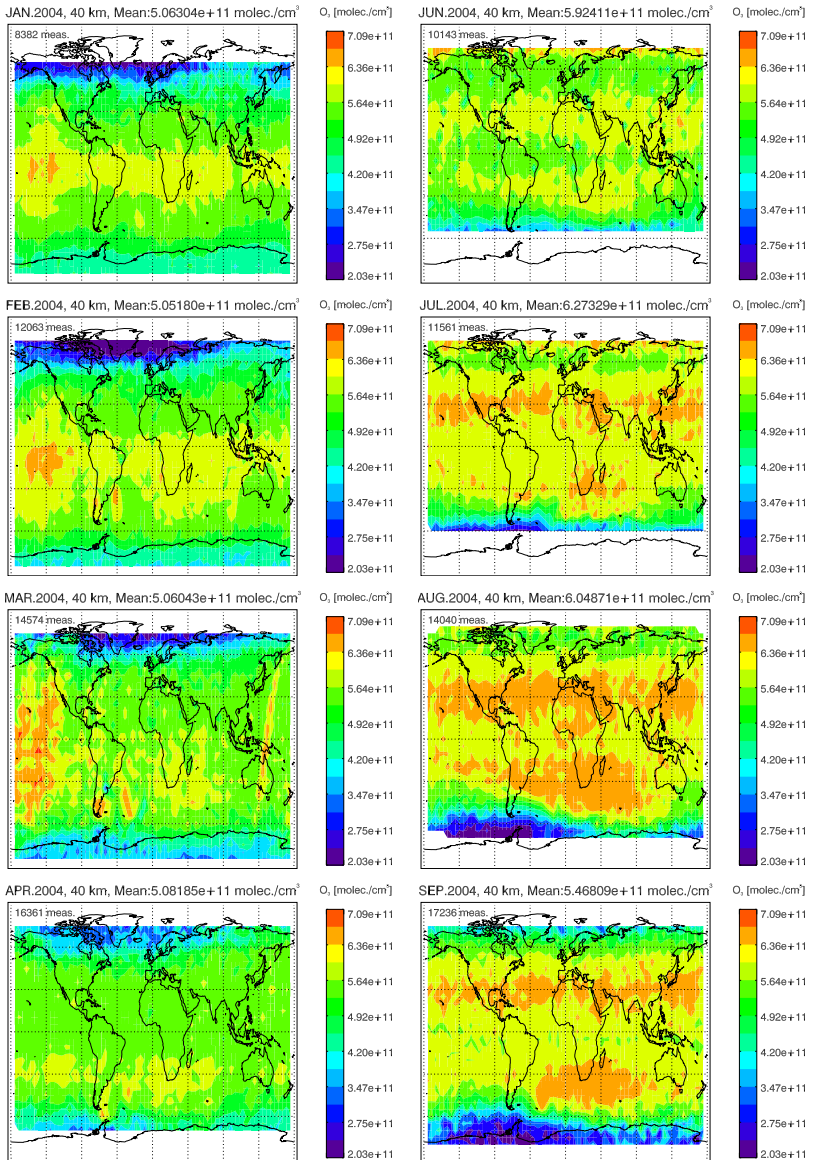
Figure 9.4: Global monthly mean ozone concentrations at 40 km from January 2004 to September 2004. The northern and southern summer ozone maxima as well as the southern winter maximum is clearly observable where the northern summer maximum is more distinctive in comparison to the southern. See the continuation of the time series in 2004 in Figure 9.5.

OCT.2004, 40 km, Mean:5.30490e+11 molec./cm³   O₃ [molec./cm³]

DEC.2004, 40 km, Mean:5.25815e+11 molec./cm³   O₃ [molec./cm³]

NOV.2004, 40 km, Mean:5.13976e+11 molec./cm³   O₃ [molec./cm³]
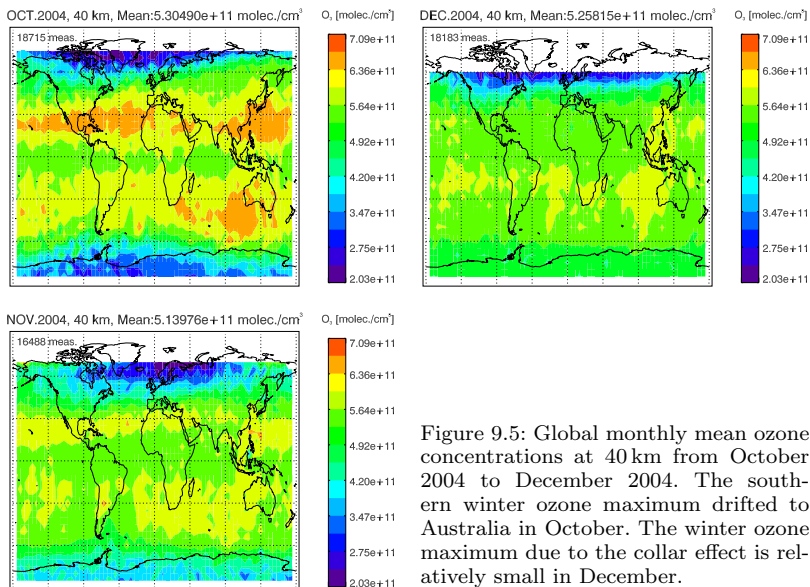
Figure 9.5: Global monthly mean ozone concentrations at 40 km from October 2004 to December 2004. The southern winter ozone maximum drifted to Australia in October. The winter ozone maximum due to the collar effect is relatively small in December.

weak and ozone mixing ratios are mainly determined by chemical effects (Rosenfield et al., 1994).

In summary, it can be stated that the upwelling tropical ozone provides a maximum in the summer hemisphere but the extent of this maximum in the northern summer is much stronger although a secondary maximum also appears in the southern mid-latitudes. This second maximum drifts south- and eastwards, before it vanishes in northern winter.[8]

---

poles, in the middle and upper troposphere and the stratosphere. The vortex is most powerful in the hemisphere's winter, when the temperature gradient is the steepest, and diminishes or can disappear in the summer. The Antarctic polar vortex is more pronounced and persistent than the Arctic one. The Arctic vortex is elongated in shape, with two centers, one roughly over Baffin Island in Canada and the other over northeast Siberia. The chemistry of the Antarctic polar vortex has created severe ozone depletion. The nitric acid in polar stratospheric clouds reacts with chlorofluorocarbons to form chlorine, which also destroys ozone. These clouds can only form at temperatures below about $-80°$ C, so the warmer Arctic region does usually not have an ozone hole.

8 Actually, the vortex rotates about every 22 days to a very variable extent. In the presented observations only monthly averaged observations are shown.

9.4 Yearly Variability

The simultaneous appearance of two maxima at 40 km in the northern summer and southern winter is also observed in 2005 (see Figure 9.6, where ozone concentration contours for August 2002, 2004, and 2005 are shown). In 2002, only a broadening of the maximum in southern summer maximum (December 2004) can be seen. A small secondary maximum is just observed around Madagascar. The collar effect seems to occur every year, but with a different extent.
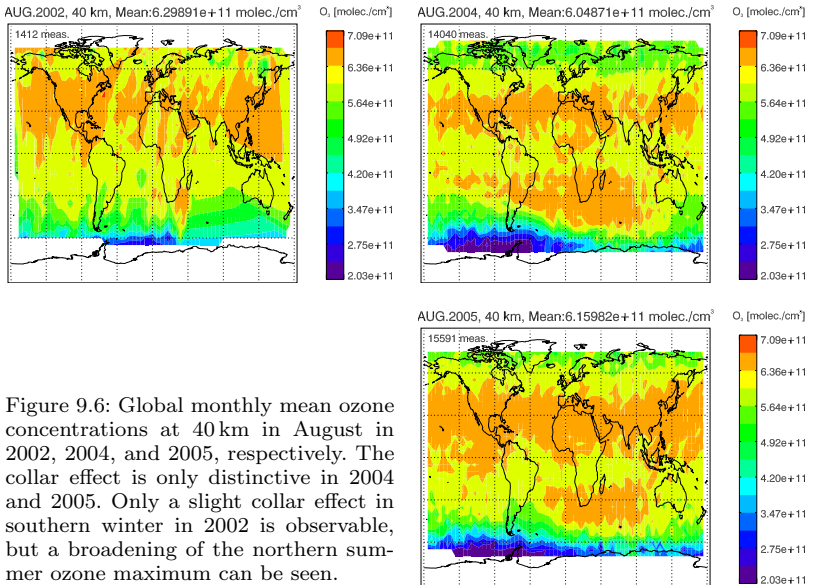
Figure 9.6: Global monthly mean ozone concentrations at 40 km in August in 2002, 2004, and 2005, respectively. The collar effect is only distinctive in 2004 and 2005. Only a slight collar effect in southern winter in 2002 is observable, but a broadening of the northern summer ozone maximum can be seen.

10 Ozone Depletion During the Solar Storm Oct./Nov. 2003

This section treats the massive ozone depletion caused by solar particle precipitation in October and November 2003 as seen in the retrieved SCIAMACHY ozone profiles. The ozone depletion during the 'Halloween storm', which was one of the strongest solar storms ever observed, is both an excellent quality test of the retrieved ozone profiles[1], and an example of the exciting interaction between the Sun and the Earth.

In general Sections 10.1 to 10.3 follow the publication of Rohen et al. (2005) and are therefore also based on the efforts of the coauthors of this paper. Corresponding parts will be denoted.

10.1 Introduction to Solar Proton Events

The Sun drives the photochemistry of the atmosphere through variations in the solar radiance on different time scales, e.g., the eleven year solar cycle, which has been shown to cause variations in the to-

---

1 The observations show that even under exceptional conditions such as a bombardment with highly energetic solar particles, both the Envisat spacecraft and the instruments on board are capable to perform reliable measurements. This is a benefit from the large size of the spacecraft and the robustness of the instruments. Observations under extreme conditions such as during a solar proton event are also a challenge for the retrieval technique. Such rapidly changing ozone concentrations in the upper stratosphere and lower mesosphere are usually rare. Additionally, limitations of the radiative transfer model can be tested, or the capability of the technique to provide real ozone concentration profiles, even if the true profiles are far apart from the *a priori* profiles. The shape of the profiles under solar proton event conditions is also quite different and are, therefore, a challenge for the profile retrieval.

tal ozone column (Jackman et al., 1996), the occurrence frequency and brightness of noctilucent clouds (Thomas and Olivero, 1989) and many other atmospheric parameters. The Sun also affects the terrestrial atmosphere through more intermittent events such as coronal mass ejections that enhance the precipitation of highly energetic particles (protons, electrons, and ions) into the mesosphere and upper stratosphere (Weeks et al., 1972; Crutzen et al., 1975; Baker, 2000). These charged particles do not penetrate the atmosphere at all latitudes, but are guided by the Earth's magnetic field lines and therefore enter the middle atmosphere in the polar cap regions mainly at geomagnetic latitudes above $60°$. The penetration depth and the ion production rates are a function of the proton energies. Protons with energies of about $1\,MeV$ reach the mesopause, $10\,MeV$ protons reach about $65\,km$, and protons with $100\,MeV$ get down to about $30\,km$ to $35\,km$ (Reid, 2001).

During a solar proton event[2] the precipitating highly energetic protons ionize the major atmospheric constituents N_2^+ (58.5 % partitioning of total ionization), N^+ (18.5 %), O^+ (15.4 %), and O_2^+ (7.6 %) (Solomon and Crutzen, 1981). The transformation of all initial ions to intermediate water clusters (Swider and Kenesha, 1973; Solomon and Crutzen, 1981; Jackman and McPeters, 2004), as well as further clustering and dissociative recombination of these water clusters produce the main HO_x constituents H and OH.

NO is a result of N_2 dissociation and a series of interchange and recombination reactions involving nitrogen and its ions (Rusch et al., 1981). The net effect is the production of atomic nitrogen which is oxidized to nitric oxide. Ozone is destroyed through the well known HO_x and NO_x cycles. The HO_x catalytic cycle is very efficient in the mesosphere and upper stratosphere, above about $40\,km$, while the NO_x cycle is most efficient in the middle stratosphere (Lary, 1997; Wayne, 1985), see also Section 3.2.

To describe the effect of the solar proton event induced ozone depletion, the sources and sinks of HO_x and NO_x under normal conditions are briefly summarized. HO_x is normally produced by photolysis of

---

2 An often used acronym of solar proton event is SPE.

water vapor, and the reaction of atomic oxygen in the D state with water vapor, and it is rapidly destroyed through

$$OH + HO_2 \rightarrow H_2O + O_2 \,. \tag{10.1}$$

The largest natural source of stratospheric NO, the main driver of the NO_x cycle, is the reaction of nitrous oxide with atomic oxygen in the D state, which is produced by photolysis of ozone

$$O(^1D) + N_2O \rightarrow 2\,NO \,. \tag{10.2}$$

The depletion of NO is due to photolysis,

$$NO + h\nu \rightarrow N + O \qquad \nu < 191\,nm \,, \tag{10.3}$$
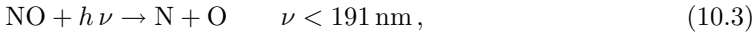
or the reaction with atomic nitrogen by

$$N + NO \rightarrow N_2 + O \,. \tag{10.4}$$

Due to the optical thickness of the atmosphere for radiation at wavelengths below $191\,nm$, photolysis of NO is mainly active at altitudes above about $50\,km$. The ozone depletion through HO_x closely follows the ionization nearly instantaneously and is rapidly reduced again, after the enhanced proton fluxes cease (Solomon and Crutzen, 1981). In contrast, the NO_x induced depletion destroys ozone for several months or years by conserved NO_x sinking down into the stratosphere (Crutzen et al., 1975; Randall et al., 2005).

In the summer hemisphere the solar proton event induced depletion of ozone is less apparent due to the photolyzed water vapor and therefore more ambient HO_x. With continuous solar illumination and hence ozone production, the solar proton event depleted ozone can recover quickly. Also, NO_x is depleted faster in the summer hemisphere (see Equation (10.3)) and so leads to an enhancement in the ozone concentrations.

Although the catalytic ozone destruction can reach $50\,\%$ or more in the mesosphere and upper stratosphere, the impact on the total ozone column, and therefore on the ultraviolet irradiance at the surface associated even with strong solar proton events, is less than $1\,\%$

to 2% (Jackman et al., 2005a). Apart from the production of HO_x and NO_x, solar proton events were previously speculated to lead to an enhanced stratospheric aerosol loading caused by ion nucleation of sulphate aerosol particles (Shumilov et al., 1996).

Mipas observations showed the establishment of a high altitude (35 km to 45 km) HNO_3 layer between 20 November 2003 and early January 2004, this is caused by NO_x produced during the solar proton event in Oct./Nov. 2003 (Orsolini et al., 2005). HNO_3 is photolyzed to yield OH in the upper stratosphere and mesosphere (Solomon and Crutzen, 1981). Orsolini et al. (2005) also showed a confinement of these phenomena to the polar vortex regions.

According to Jackman et al. (2005a) the Oct. 28/29 solar proton event was the fourth largest solar proton event within the past four decades in terms of the total amount of produced NO_x (3.4×10^{33} molecules NO_x). The largest solar proton event ever measured occurred in October 1989 (6.7×10^{33} molecules NO_x), followed by the events on August 1972 (3.6×10^{33} molecules NO_x), and on 14 July 2000 (3.5×10^{33} molecules NO_x). Seppälä et al. (2004) published the first results on ozone depletion and production of NO_2 due to the Oct./Nov. 2003 solar proton events retrieved from Gomos. The study focuses on northern hemisphere observations during nighttime. Seppälä et al. (2004) presented zonally averaged ozone and nitrogen dioxide profiles at geographic latitudes in the northern hemisphere between 70° and 75° and compared them with results from a non solar proton event forcing model.

The long-term effects of this solar proton event on NO_2 and O_3 concentrations between March and July 2004 as seen by numerous satellite instruments like Mipas, Haloe, Sage iii, Poam iii and Osiris have already been shown (Randall et al., 2005). Randall et al. (2005) showed that the NO_x enhancements and O_3 reductions from January 2004 up to July 2004 can be attributed to a combination of the effects of the solar proton event in Oct./Nov. 2003 and an exceptionally strong vortex. Haloe and Sbuv 2 satellite observations of O_3 and changes of NO_x (NO and NO_2) during the Halloween storm and model simulations of O_3, NO_x, and OH in both hemispheres are presented in the work of Jackman et al. (2005b). Jackman et al. (2005b)

predicted OH enhancements of 100 % and measured ozone depletions of greater than 70 % and a NO_x induced long term ozone depletion for over eight months beyond the solar proton event in Oct./Nov. 2003.

10.2 Modeling Effects of Solar Proton Events

The effect of highly energetic solar protons on the chemical composition of the middle atmosphere is modeled in two steps. In the first step atmospheric ionization rates are calculated from measured proton fluxes. In the second step those ionization rates are used in a photochemical model of the neutral atmosphere. The derivation of the ionization rates was performed at the University of Osnabrück by Dr. M.-B. Kallenrode and J. Schröter; the modeling was performed at the IUP by M. Sinnhuber.

10.2.1 Atmospheric Ionization

Ionization rates for precipitating protons are calculated with a Monte-Carlo code based on the Giga bit European Academic NeTwork4 (GEANT4) toolkit (Agostinelli et al., 2003). First, the energy spectra of precipitating protons in the range from 1 MeV to 500 MeV are retrieved from the Geostationary Operational Environmental Satellite 11 (GOES-11) data. These serve as input for a Monte Carlo simulation, which calculates energy losses for a standard atmosphere consisting of N, O, O_2, N_2 and Ar. Ion pair production rates are determined for the assumption of an average ionization energy of 35 eV (Porter et al., 1976). The considered energy range is discretized into 109 equidistant energy steps on a logarithmic scale, and the precipitation angles in nine equidistant steps from 0° to 80°. Both scales are logarithmic. Particle precipitation and subsequent ionization is assumed to occur homogeneously throughout the entire magnetic polar cap and the ionization rates are determined for precipitating protons only, since reliable electron data were not available.

The error in ionization rates due to the neglect of the electrons is less than 10 %. The maximum contribution of electrons to the total ionization for two solar flares in 1989 is located at an altitude between 50 km to 70 km, never exceeds 30 % and is less than 10 % on average (Schröter et al., 2005). The contribution is very different for gradual (and electron-poor) or impulsive (and electron-rich) flares. Since the Halloween storm originated in a gradual flare and was accompanied by a strong shock, the event can be classified as electron-poor.

Figure 10.1 shows the calculated ionization rates for the northern polar cap during the solar proton event in Oct./Nov. 2003. The ionization of the atmosphere from 24 to 27 October (marked with (1) in Figure 10.1) is associated with high ionization rates in the upper mesosphere and mesopause region, but does not cause significant ionization below 70 km. On 27 October a first weak and short ionization down to about 40 km follows (2). On 28 October the first major sustaining ionization of the middle atmosphere begins (3), reaches the lower stratosphere at about 15 km and lasts for several days. It is followed by two ionization periods between 3 and 7 November (4 and
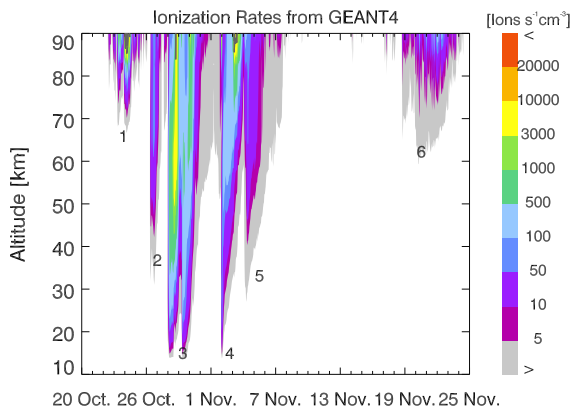
Figure 10.1: Atmospheric ionization rate profiles from GEANT4 in the northern hemisphere. Hourly resolved rates are used for the photochemical calculations. The marks on the abscissa denote 00:00 UTC of the particular day. The vertical resolution is approximately 3.5 km. Data have been provided by M.-B. Kallenrode (University of Osnabrück).

5). Finally a smaller event occurred between 20 November and 25 November down to 60 km (6). The ionization rates used by Jackman et al. (2005b) derived with the methodology described by Vitt and Jackman (1996) agree almost exactly with these calculated ionization rates.

10.2.2 Photochemical Model

To consider the geographic distribution and the variability of the solar zenith angles of the SCIAMACHY measurements, a combination of a two dimensional chemistry transport model and a one dimensional model is used. The calculations have been performed by M. Sinnhuber (IUP, Bremen). The chemistry codes of both models are based on SLIMCAT (Chipperfield, 1999). The two dimensional and one dimensional model use the same set of chemical reactions, the same reaction rates and the same implementation of ionization driven NO_x and HO_x production. The two dimensional model uses a time saving family approach for short-lived species, while the one dimensional model is used to model the diurnal variability of trace gases, and does not use a family approach. The formation of NO_x and HO_x due to atmospheric ionization is calculated with an empirical algorithm (Porter et al., 1976; Solomon and Crutzen, 1981), and is similar to the approach of Jackman et al. (2005b); 1.25 NO_x molecules are produced per ion pair in total. 55 % are produced as NO, 45 % are produced as ground-state N, which can be a sink for NO_x via the reaction of N and NO. Up to two HO_x molecules are produced per ion pair, decreasing with increasing altitude and atmospheric ionization (Jackman et al., 2005b). The two dimensional model combines the chemistry code with the THIN AIR metrological code (Kinnersley, 1996) that calculates temperature, pressure and wind speed on isentropic surfaces from the ground up to 100 km. Vertical transport across the isentropes is calculated from heating rates. The model has a horizontal resolution of 9.5° extending from 85.3° S to 85.3° N in 19 evenly spaced latitude bands, and a vertical resolution of about 3 km. 24 different model runs were carried out with the two dimensional model on different longitude bands from

the Greenwich meridian once around the globe in 15° steps. Ionization is considered only in areas where the geomagnetic latitude is larger than 60°. Different model runs for different longitudinal segments are necessary because of the large displacement of the southern geomagnetic polar cap. For model boxes containing the edge of the polar cap, ionization is scaled by the ratio of the polar cap area within this box to the total box area. This might lead to an imprecise estimation of the ionization effect in areas at the edge of the polar cap, a possible error source that could only be avoided by significantly increasing the spatial resolution of the model boxes.

Model results from the two dimensional model are used to initialize a one dimensional model run with the solar zenith angle of each Sciamachy measurement. In the one dimensional model, ionization is again considered for all measurements at a magnetic latitude above 60°. The one dimensional model runs are initialized one day before the measurement, and run for two days. Model results are then output for the time corresponding to the Sciamachy measurement.

10.3 Results

10.3.1 Response to Proton Fluxes

Figure 10.2 shows the time series of zonally averaged ozone changes for an altitude of 54.4 km in the northern hemisphere above 60° geomagnetic latitude from 23 October to 24 November 2003. The model results and the Goes-11 proton flux with energies of 15 MeV to 40 MeV which are mainly responsible for the atmospheric ionization at this altitude (Reid, 2001) are also shown. The reference period for Figure 10.2 and all following figures in this section is 20 to 24 October 2003.

The proton flux and the ozone depletion rates at this altitude are mostly anti-correlated. Deviations of proton fluxes and the measured ozone depletion rates, e.g., on 1 November, are possibly due to the sampling of the measurements. Model simulations reproduce the depletion qualitatively well, but underestimate the amount of depletion
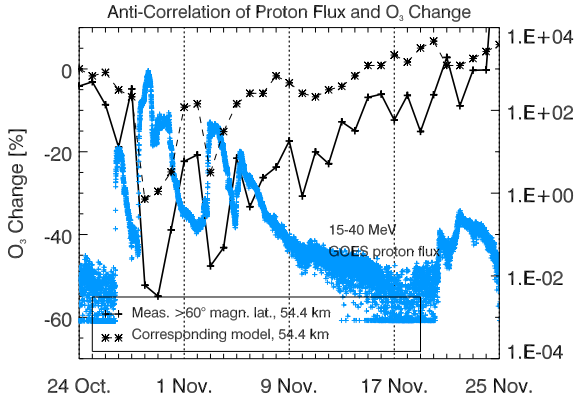
Figure 10.2: Ozone depletion rates above $60°\,N$ geomagnetic latitude (crosses), model results (stars), and GOES-11 $15\,MeV$ to $40\,MeV$ proton flux (blue crosses). The altitude is $54.4\,km$ and the observation and model data are daily and zonally averaged. The reference period for this picture and for all following figures in this chapter is from 20 to 24 October 2003.

by about $20\,\%$ to $30\,\%$. This is most likely due to incorrect ionization calculations and applications of the model and will be discussed later.

The largest signatures occur from 28 to 30 October and from 3 to 4 November. On 10 November the measured ozone recovery decreases; this is obviously not caused by the proton precipitation directly but more likely by the sampling of the measurements. The variation of about $10\,\%$ as seen in the measured ozone changes after 10 November is caused by errors associated with the imprecise attitude pointing of Envisat.[3]

The time series of ozone depletion rates agrees qualitatively with observations of GOMOS (Seppälä et al., 2004) and SBUV 2 (Jackman et al., 2005b). Both noticed maximum depletion rates of up to $60\,\%$ in the northern hemisphere in the lower mesosphere; it will be shown later that this is in agreement with SCIAMACHY observations.

---

3 See discussion in Section 7.6

10.3.2 Interhemispheric Differences

Figures 10.3 and 10.4 show a global perspective of the change of ozone concentrations relative to the reference period 20 to 24 October at an altitude of 49 km in both hemispheres. In the northern hemisphere changes from 29 October to 6 November relative to the reference period are shown. For the representation of the ozone changes in the southern hemisphere the shorter time period 29 to 30 October is chosen. The depletion of ozone in the southern hemisphere does not last as long as in the northern hemisphere, so averaging many days together would dilute the observed loss.

The ozone profiles for the reference period and the ozone profiles for the solar proton event time periods are interpolated on to a grid of $2.5°$ latitude and $10°$ longitude steps using a Delaunay triangulation. Also shown are isolines of different magnetic latitudes ϕ_{mag}. These are determined from the magnetic inclination I for 2003, calculated with the WMM 2000 (World Magnetic Model 2000) (Macmillan and Quinn, 2000) and using the relation $\phi_{\mathrm{mag}} = \arctan(\frac{1}{2}\tan I)$ (Prölls, 2003, p. 224 ff.).[5] This relation for ϕ_{mag} provides a better representation than the standard magnetic coordinates based on a magnetic dipole field, because near the polar cap the actual Earth's magnetic field is not well represented by a pure dipole field.

The error in the ozone changes represented in Figure 10.4 differs from the error in the retrieved profiles as estimated by Table 7.1 on page 89. The normalization of ozone concentrations with respect to the concentrations before the solar proton event reduces the systematic errors since a large number of profiles are averaged by the triangulation. On the other hand, the maximum statistical error is larger by a factor of $\sqrt{2}$. Thus the maximum error of the changes is assumed to be larger than the error of the retrieved profiles.

The solar proton events cause ozone losses of several tens of percent in both hemispheres. In the northern hemisphere the area of ozone depletion coincides generally with the geographic polar cap rather than with the magnetic polar cap. The confinement to the polar vortex can

---

5 The magnetic inclination is defined as the angle between the tangential plane and the magnetic field vector.
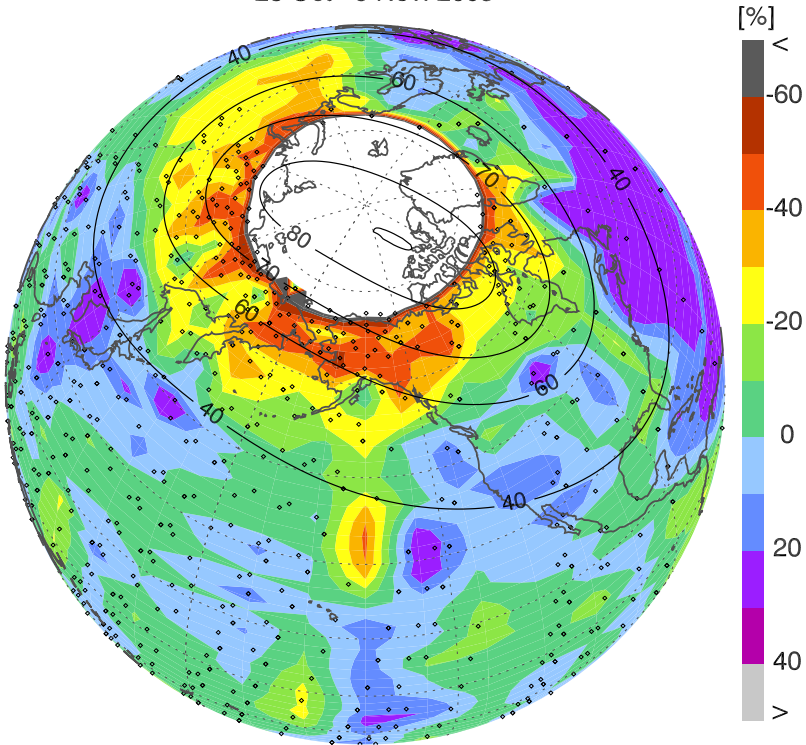
Figure 10.3: Change of ozone concentrations at 49 km altitude in the northern hemisphere in a global perspective. The figure shows the changes of ozone concentrations in a period from 28 October to 5 November relative to a reference period from 20 to 24 October. A Delaunay triangulation of the reference data set and the data set during the solar proton event and a following linear interpolation on a 2.5° latitude times 10° longitude grid is used. The white area depicts places with no observations from SCIAMACHY. The black dots indicate the locations of the limb measurements between 28 October and 5 November.[4] The black solid lines are the Earth's magnetic latitudes at 60 km derived with the WMM 2000 model (Macmillan and Quinn, 2000). The Delaunay triangulation produces changes even at locations, where no measurements were taken, e.g., over Scandinavia. This could also be due to large ozone changes during the reference time period, which also contribute to the depicted changes. Evidently the ozone depletion is confined to the geographic and geomagnetic poles.
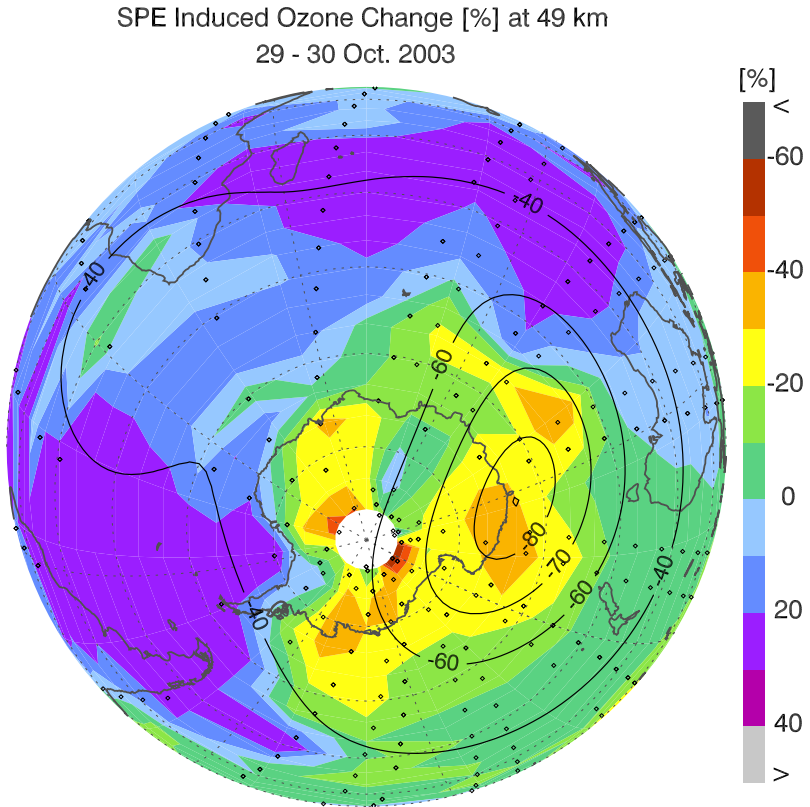
Figure 10.4: Change of ozone concentrations at 49 km in the southern hemisphere between 29 and 30 October. Settings and descriptions are the same as in Figure 10.3.

also be seen in long term observations (Randall et al., 2005; Orsolini et al., 2005). Perhaps strong winds cause a zonal mixing of the air masses at the edge of the vortex within the first week after the first event, and are therefore the reason for the confinement of the ozone loss to the geographical pole. This issue is still puzzling.

The ozone loss in the southern hemisphere is mainly confined to the region at high magnetic latitudes. Additional depletion of ozone occurs around the geographic South Pole due to a larger solar zenith angle and therefore enhanced ozone depletion through photolysis and

Equation (10.2). An anomaly in the Earth's magnetic field is located above the South Atlantic, where ozone depletion is also observed even outside the geographic polar cap. This depletion is in agreement with the observations of Jackman et al. (2005b).

The observed ozone depletion at 49 km is significantly different in the northern and the southern polar stratopause, this was also observed by Jackman et al. (2005b). In the northern hemisphere maximum ozone depletion rates of 50 % or more occur at 49 km. In contrast, the magnitude of the ozone depletion as well as the spatial extent is smaller in the sunlit southern hemisphere. This is a consequence of smaller solar zenith angles in the southern hemisphere, i.e., stronger solar illumination, which leads to photolysis of the ambient H_2O and higher ambient HO_x concentrations that are not produced by the solar proton event. Therefore the effect of HO_x production due to the solar proton event is not as large as in the darker hemisphere. Additionally, the solar proton event depleted ozone in the southern hemisphere recovers quickly because of the continuous solar illumination and photolysis of molecular oxygen for ozone production. NO_x is depleted faster through photolysis (10.3) above about 50 km, which also enhances the recovery of ozone. In contrast, in the winter hemisphere H_2O as well as NO are protected from the sunlight and ozone depletion is stronger and lasts for a longer time.

The observations of this interhemispheric difference, the shape of the ozone depletion area and the magnitude of the depletion rates agree quite well with the calculations of Jackman et al. (2005b). Seppälä et al. (2004) provide a good agreement in terms of the spatial extent of the ozone depletion area. They also found that the center of the depletion in the northern hemisphere is above the pole and elongated towards Russia and North America. Almost no depletion was observed above Europe. Sbuv observations (Jackman et al., 2005b) and the observations shown in this section show that the ozone depletion in the southern hemisphere is mainly located poleward of Australia.

10.3.3 Global Model Predictions

Figure 10.5 shows the measured and modeled changes of the zonally averaged ozone concentration before and during the solar proton event relative to the mentioned reference period from 20 to 24 October for each day.
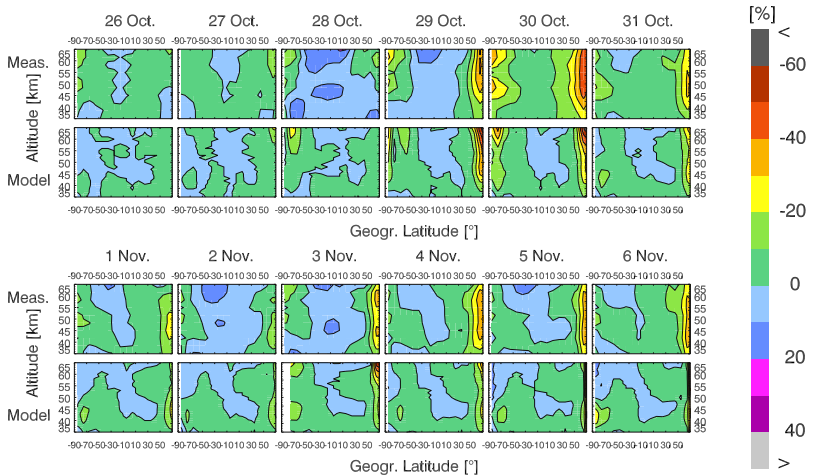
Figure 10.5: Measured and modeled change of ozone concentrations during the Halloween storm as a function of the altitude and latitude. The measurements and models show the significant ozone depletion during the solar proton event.

The model predicts the general morphology of ozone depletion and recovery fairly well, although it slightly underestimates the ozone changes, as already seen in Figure 10.2 on page 131. On 29 October the model dramatically overestimates the depletion. A separation of the ozone depletion on 3 November at about 50 km is observed, indicating the regimes of HO_x and NO_x. In the southern hemisphere the model again predicts the temporally varying morphology of the ozone depletion fairly well. Only isolated ozone changes near 70° differ from the measurements.

The general underestimation may be caused by incorrect calculated ionization rates or due to the transfer of these rates on to a geographic

grid for the model calculations (see Section 10.2.2). Other possible reasons for the underestimate may be the omission of the ionization by the solar electrons or simply because of the fact that the spatial distribution of the calculated ionization used in the model is not as homogeneous as assumed.

The overestimate on 29 October is most likely due to the fact that the production of HO_x due to ionization is calculated with empirical algorithms in the model; the amount of available water vapor is not limited. This is particularly important during events with large HO_x production. HO_x is not present in the atmosphere to the extent that the model predicts.

The isolated ozone changes in the southern hemisphere at about $70°$ are caused by the separation of the southern geographic and magnetic poles, which leads to incorrect ionization rates at the edge of the auroral oval. Previous model runs showed that using only zonally averaged ionization rate profiles is insufficient for modeling the solar proton event effect, particularly in the southern hemisphere where the magnetic polar cap is not coincident with the geographic polar cap. Therefore meridional bins have been introduced and these improve the model results significantly; differences in the model results of ozone loss at the edge of the auroral oval without this longitudinal binning are larger than 50 %.

Ozone Depletion Time Series

Figure 10.6 shows time series of ozone concentration changes between 24 October and 27 November in both hemispheres in the magnetic pole areas. The ozone depletion in the southern hemisphere is weaker than in the northern hemisphere, where the ozone depletion during the first large event from 28 to 30 October exceeds 50 %. The second large event produces ozone depletion with two maxima at 45 km and 55 km. These maxima can be seen again in the model results and in the southern hemisphere measurements during the first event. Ozone recovers quickly above 50 km in both hemispheres after the second large event whereas an ozone loss of about 10 % continues for several weeks after the events below 50 km.
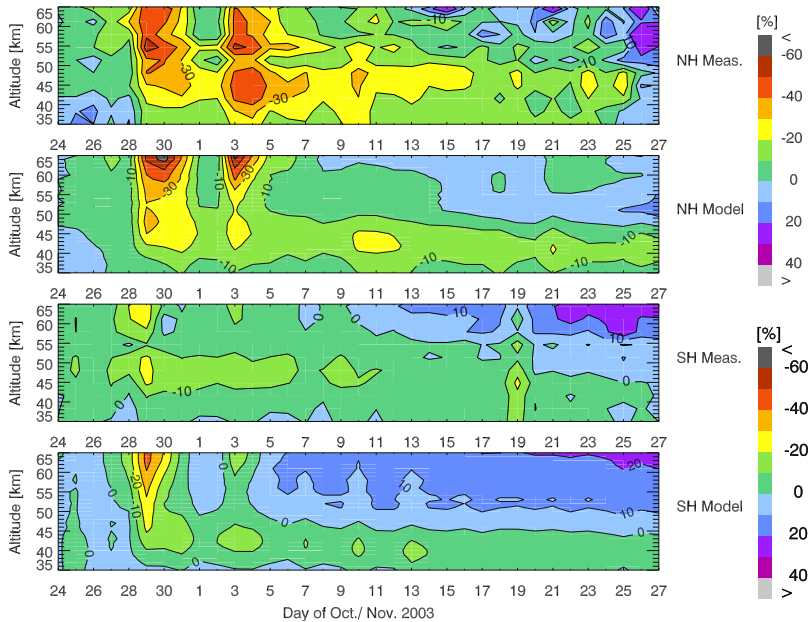
Figure 10.6: Ozone change in both hemispheres above 60° magnetic latitude. Below each representation of the measurements the corresponding model results are shown. Retrieved profiles and model results are daily and zonally averaged.

The interhemispheric difference is well captured by the model, as well as the fast recovery of ozone at higher altitudes due to the short lifetime of HO_x and photolytic production of ozone. At lower altitudes the recovery of ozone is well captured by the model. The model also shows the regime change at about $50\,km$ between ozone loss driven by short-lived HO_x and by long-lived NO_x. The modeled long-term ozone recovery is only slightly faster than that seen in the observations. This again is most likely due to underestimated ionization rates (see Section 10.2.2 and Section 10.3.3).

The establishment of two maxima is due to the already recovered ozone in the boundary region and the renewed ionization in the HO_x region. In the southern hemisphere the model does not show these maxima, this most likely due to the incorrect HO_x production during large events as discussed in the previous section.

Additionally, an enhancement of ozone can be observed in both hemispheres above 45 km on 26 November in the northern hemisphere and from 22 to 27 November in the southern hemisphere. This was also seen by Seppälä et al. (2004) and is a seasonal effect.

10.3.4 HO_x and NO_x Regimes

In a HO_x dominated regime and for a horizontally homogeneous proton precipitation, the solar proton event induced ozone change is larger at larger solar zenith angles (Solomon et al., 1983). This is due to the fact that at higher solar zenith angles the solar proton event induced HO_x production is larger relative to the HO_x production from H_2O photolysis (Solomon and Crutzen, 1981). In contrast, the NO_x induced ozone loss is relatively large at even low solar zenith angles. The NO_x catalytic cycle is more efficient due to enhanced production of atomic oxygen by photolysis (see Equation (10.2)).

Figure 10.7 shows the change of the measured ozone concentrations from 29 to 30 October above 70° S geomagnetic latitude as a function of the solar zenith angle for different altitudes.
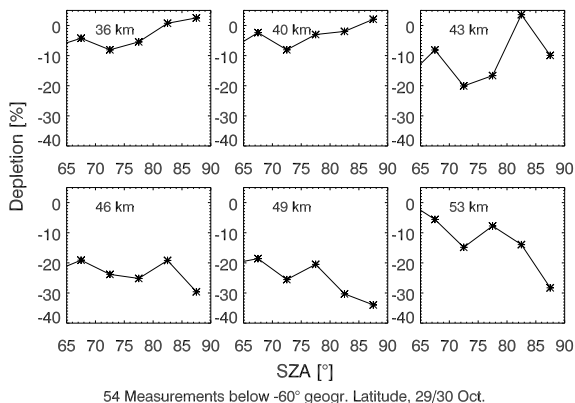
Figure 10.7: Ozone change from 29 to 30 October above 70° S geomagnetic latitude as a function of the solar zenith angle. Averaged measurements are shown from 36 km to 63 km.
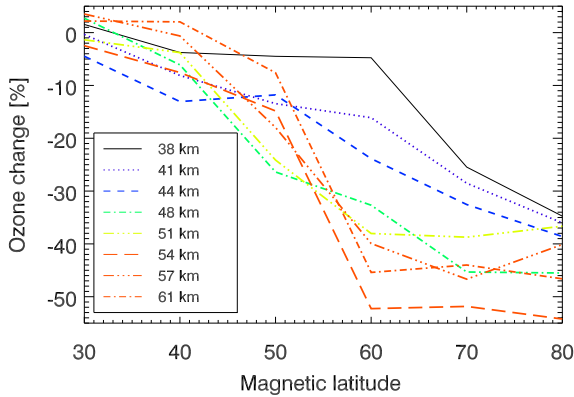
Figure 10.8: Ozone depletion rates at different altitudes in the northern hemisphere on 29 and 30 October across the border of the auroral oval. Averages of the ozone changes within $10°$ latitude bins have been taken.

Ozone is depleted mainly through NO_x at lower altitudes and small solar zenith angles. Less ozone is depleted during the solar proton event with increasing solar zenith angle. At higher altitudes, more ozone is depleted with increasing solar zenith angles during the solar proton event. The dependence of the ozone depletion on the solar zenith angle cannot be separated from the dependence on the magnetic latitude. Although this weakens the effects shown in Figure 10.7 the dependence on the geomagnetic latitude can not explain the different behavior of the ozone change at different altitudes.

10.3.5 Vertical and Horizontal Extent of the Ozone Depletion

The model calculations presume a vertical edge to the ionization at 60° magnetic latitude. Incorrect assumptions for the shape of the ionization area are a potential error source for modeling the ozone loss. In Figure 10.8 ozone losses are shown across the border of the auroral oval.

Ozone losses are not significant at low geomagnetic latitudes. They increase over a certain geomagnetic latitude range, and then stay more

or less constant at high geomagnetic latitudes. At higher altitude the transition from low to high ozone change occurs in a relatively small geomagnetic area around $50°$ N to $60°$ N geomagnetic latitude. With decreasing altitudes, the transition region gets larger and the transition is less sharp. At lower altitudes ozone losses occur at geomagnetic latitudes of $40°$ N to $50°$ N.

Although these findings can not be evaluated quantitatively because of the correlation of magnetic latitude and the solar zenith angle, significant ozone depletion is found at geomagnetic latitudes between $40°$ N and $50°$ N. Neither vertical transport of NO_x can be a reason, due to the slow vertical motion of the air masses, nor the gyro radii of the incident protons, which increase at lower altitudes only up to about 1000 km. The most likely reason is that the edge of the ionization is not as sharp as assumed in most of the models.

10.4 Infrared Atmospheric Band Emissions

Observations of Infrared Atmospheric band limb emission rates[6] during the solar proton event in October and November 2003 are shown in this section and indicate another novel way to observe solar storms.[7]

10.4.1 SCIAMACHY Infrared Atmospheric Band Spectra

Figure 10.9 shows a modeled emission spectrum (Degenstein, 1999) and a sample SCIAMACHY spectrum in the Infrared Atmospheric bands at an altitude of 55 km.

Jones and Harrison (1958) detected the Infrared Atmospheric band emissions in rocket measurements. Evans et al. (1968) and Llewellyn et al. (1973) showed the first limb emission rate profiles and made clear

---

6 The limb emission rate is the integrated emission rate along the line of sight in limb viewing geometry (the rate is called *non-inverted*).

7 See also the introduction of the Infrared Atmospheric band in Section 3.3.
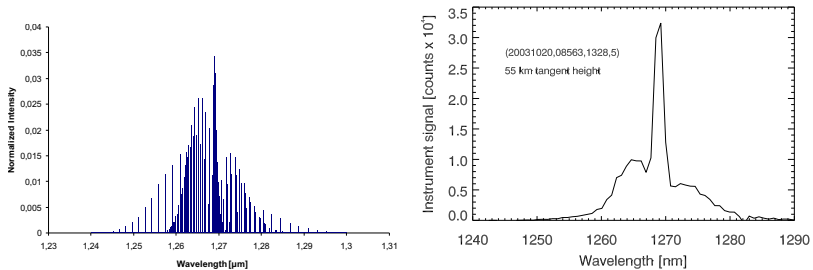
Figure 10.9: Left: Modeled $O_2(a^1\Delta_g \rightarrow X^3\Sigma_g^-)$ spectrum around $1.27\,\mu m$ (Degenstein, 1999) which exhibits the P- and R-branches in the rotational-vibrational spectrum, and the centered Q-branch. Courtesy of D. Degenstein. Right: Sample $O_2(a^1\Delta_g \rightarrow X^3\Sigma_g^-)$ emissions as measured by Scia-machy at 55 km tangent height. Due to a spectral resolution of about 0.21 nm the spectrum is fairly smooth, but shows similar branch structures like in the modeled spectrum (left panel).

that the main source of $O_2(a^1\Delta_g \rightarrow X^3\Sigma_g^-)$ emissions in the upper atmosphere is ozone dissociation in the Hartley bands, i.e.,

$$O_3 + h\nu \rightarrow O_2(a^1\Delta_g) + O(^1D)\,. \tag{10.5}$$
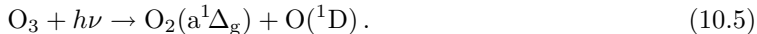
Mlynczak and Olander (1995) reviewed the sources and sinks of the Infrared Atmospheric band limb emission rates, whose losses can roughly be summarized by

$$O_2(a^1\Delta_g) \rightarrow O_2(X^3\Sigma_g^-) + h\nu \quad (1.27\,\mu m) \tag{10.6}$$
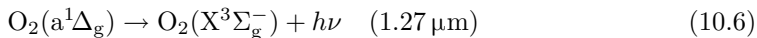
and secondly quenching

$$O_2(a^1\Delta_g) + M \rightarrow O_2(X^3\Sigma_g^-) + M\,, \tag{10.7}$$

mainly by the most abundant atmospheric trace gas molecules.[8] Reliable ozone profiles and columns have been induced from Infrared Atmospheric band limb emission rate measurements, (e.g., Llewellyn and Witt, 1977; Weeks et al., 1978; Thomas et al., 1983; Evans et al., 1988). Although the general reaction schemes are well known, the potential errors in the key rate constants are still large; they range from

---

8 Mainly O_2 and N_2

five to more than several hundreds percent (Mlynczak and Olander, 1995). The Einstein A coefficients for the spontaneous emission in Equation (10.6) retrieved from several measurements and compiled in the Hitran spectroscopic database (Rothman et al., 1998) differ by a factor of two, and recently derived rate coefficients from Mlynczak and Olander (1995) are smaller by a factor of 1.75 than, e.g., from Badger et al. (1965).
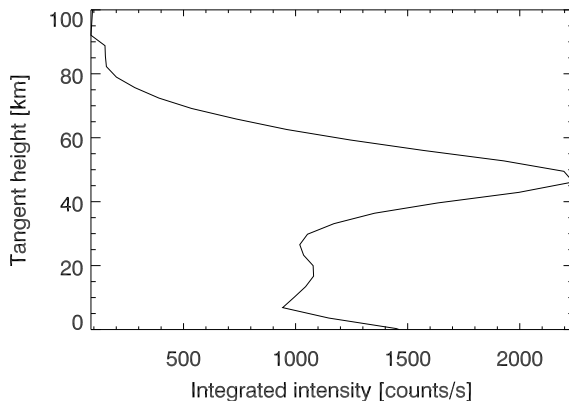
Figure 10.10: Non-inverted altitude limb emission profile of $O_2(a^1\Delta_g \rightarrow X^3\Sigma_g^-)$ limb emission rates in a spectral range between 1.2685 µm and 1.2695 µm. The peak is mainly caused by the decreasing (ozone) density at higher tangent heights (and therefore smaller amounts of the $O_2(a^1\Delta_g)$ state of O_2), the increasing quenching, and the increasingly absorbed radiation in the Hartley bands at lower altitudes. The measurement was taken on 20 October 2003 (08563, 1328, 10).

Figure 10.10 shows a non-altitude inverted Infrared Atmospheric band limb emission profile from a sample Sciamachy measurement on 20 October 2003. The profile peaks at about 50 km what is caused by the decreasing air and ozone density at higher altitudes and by the increased quenching and the decreasing ultraviolet radiation at lower altitudes.

10.4.2 Infrared Atmospheric Band Limb Emission Rates

The limb emission rates exhibit a significant decrease during the solar proton event as for the presented ozone concentration in Section 10.3 because the Infrared Atmospheric band emissions are mainly excited through the photolysis of ozone.

Figure 10.11 shows the ratio of the integrated limb emission rates in the spectral range between 1267 nm and 1271 nm during the solar proton event in October and November 2003 relative to the reference time period between 20 and 24 October 2003. About 500 spectra for each day have been averaged. The retrieved emission profiles are not altitude inverted and the measurements show therefore bends, especially at lower tangent heights.

A clear connection to the solar proton event is observable. The decrease starts on 28 October with decreasing emission rates of up to 30 %. On 29 October depletion maxima between 60 km and 70 km are observable in both hemispheres. Especially in the southern hemisphere the emission rates recover until 2 November when the second event (see Figure 10.1) starts.
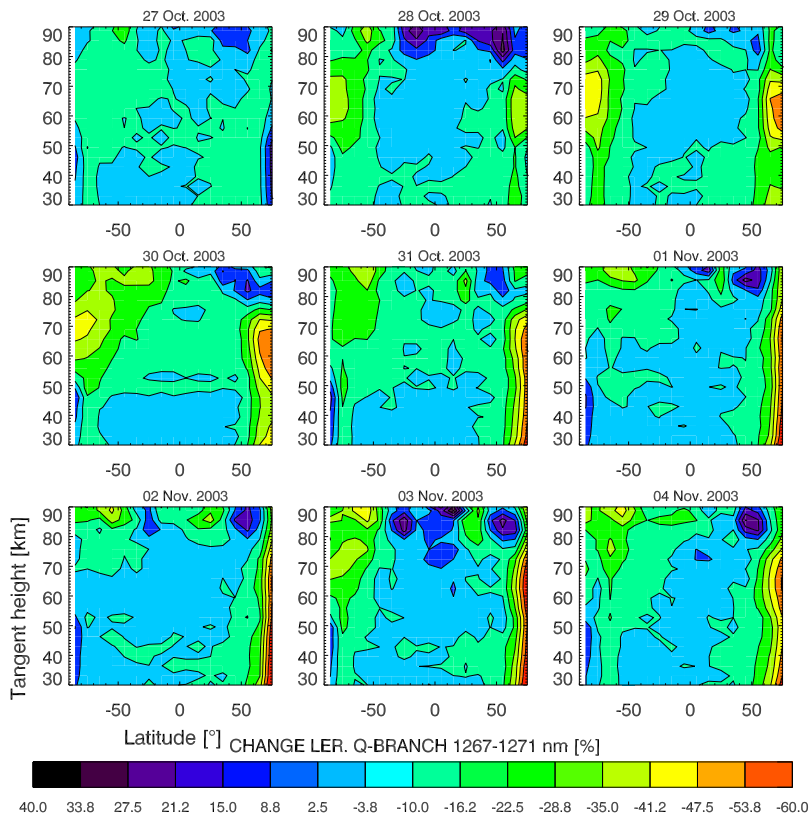
Figure 10.11: Change of Infrared Atmospheric band limb emission rates during the solar proton event in October and November 2003 relative to a reference period of 20 to 24 October 2003. All available spectra on a particular day have been taken for this representation, i.e., about 500 spectra on each day. The shown observations are zonally averaged into $10°$ latitude bins between $85°\,$S and $75°\,$N. The measurements show a significant decrease of $O_2(a^1\Delta_g \rightarrow X^3\Sigma_g^-)$ limb emission rates at the same altitude and time similar to the depletion of ozone as shown in Figure 10.5.

10.5 Summary

In this chapter the ozone depletion as retrieved from Sciamachy measurements during the solar proton events in October and November 2003 was shown. The depletion rates are in agreement with the location and arrival of the incident solar proton fluxes, and the calculated ionization rates. The depletion in the northern hemisphere is restricted more closely to the geographical pole whereas the southern hemisphere depletion is confined to the geomagnetic polar region. Depletion rates reach 60 % or more in the northern hemisphere and 40 % in the southern hemisphere. The interhemispheric difference is caused by different water vapor amounts. Model runs show that the HO_x production is overestimated for large events while the NO_x production is slightly underestimated. Time series of observations indicate the extent and temporal order of the ozone depletion. The border of the HO_x and NO_x regimes at about 50 km is clearly distinguished. The establishment of two simultaneous depletion maxima in both hemispheres has been identified, these are caused by temporally and spatially changing HO_x and NO_x regimes during the proton events, respectively.

In a second part observations of Infrared Atmospheric band limb emission rates during the solar proton event were presented. They show a similar temporal change of the emission rates as those observed for the ozone depletion rates. These emission rates may provide a novel way to study solar proton events.

11 Conclusions and Outlook

This thesis documents the evaluation of a novel retrieval technique to infer ozone concentration profiles in the upper stratosphere and lower mesosphere from SCIAMACHY limb scatter measurements in the Hartley bands. A second focus has been on the observation of ozone distributions and the ozone depletion by highly energetic solar protons during the solar storm between 26 October and 6 November 2003.

A retrieval technique (current VERSION 2.25) has been developed successfully, and comprehensive sensitivity and validation studies have been performed. These studies show that the technique provides reliable ozone concentration profiles between altitudes of 35 km and 65 km. Although the technique itself has an accuracy of better than 10 %, the error in the tangent height specification leads to total inaccuracies between 15 % and 20 %. Even so, comparison with well validated observations for other instruments up to an altitude of 50 km shows an agreement for the collocated profiles that is generally within 10 %, and within at least 20 % above this altitude. A slight overestimate between 40 km and 50 km has been found and an increasing deviation with increasing altitude due to the tangent height offset. The retrieved ozone profiles have also been validated between 50 and 65 km with a mean agreement of 20 %. More validations need to be performed in the future since the comparisons with HALOE ozone profiles provide only partial validation as there is some uncertainty in solar zenith angle correction.

The morphology of ozone in the upper stratosphere and lower mesosphere has been displayed by global concentration contours. Apart from the tropical ozone maxima during the northern and southern summers a south tropical ozone accumulates in the winter due to a strong polar vortex what is known as the collar effect.

The retrieved profiles have been used to display the ozone depletion during the strong solar proton storms in October and November 2003. These show that the main chemical processes are well understood although comparisons with models show deviations that are mainly caused by incorrect settings. The observations can also be used to determine other parameters, such as the extent and change of the magnetic field due to extraterrestrial events, or to infer the ionization rates.

This work shows the feasibility of providing reliable information on ozone up to 70 km through the technique of using limb scatter measurements in the Hartley bands. The common way to infer ozone profiles at lower altitudes is the use of the Chappuis bands, and the oxygen Infrared Atmospheric band transitions at higher altitudes. It will be the task of future work to combine these retrieval techniques and to provide overall SCIAMACHY distributions between 15 km and 92 km altitude.

The retrieved ozone data allow an investigation of numerous atmospheric properties, e.g., the 'collar effect' and the correlation of the Infrared Atmospheric band transitions at solar proton event. It should also be mentioned that an additional ozone enhancement at 70 km altitude was observed that indicates a novel geophysical feature during solar proton precipitation.

Appendix

A Mipas and Gomos on Envisat

The instrument Michelson Interferometer for Passive Atmospheric Sounding (Mipas), directly opposite to the flight direction of Envisat, scans the limb of the Earth for tangent heights ranging from 5 km to 160 km in 3 km steps with an instantaneous field of view of $0.045° \times 1.8°$, which is about $3 \, km \times 30 \, km$ at the tangent point. A typical vertical scan lasts about 75 s, corresponding to a forward motion of the spacecraft of about 460 km. As it is for Sciamachy limb measurements, the tangent point is about 3000 km away from the location directly underneath the satellite.[1] Due to the related measurement technique and geometry, Mipas was used for validation campaigns with Sciamachy ozone profiles.

The second spectrometer on Envisat, the Global Ozone Monitoring by Occultation of Stars (Gomos) instrument (Bertaux et al., 1991; Esa, 2001) measures the ultraviolet radiation from 250 nm to 675 nm reflected from the stars, and in two small infrared bands. The spectral resolution is between 0.2 nm and 1.2 nm. Besides the two spectrometers, Gomos consists of two fast photometers that monitor the input signal scintillations and turbulences. Up to forty stars are observed along one orbit, and thus a good global coverage is achieved. Measurements can in principal made in daylight, but due to stray light contamination, only nighttime observations are currently used for inversions. Since disturbing light sources are avoided very accurate ozone profiles have been retrieved (Bracher et al., 2005).

---

1 This point is called the *sub-satellite point*.

B Description of the Aerosol Extinction

Mie theory (Mie, 1908) describes the scattering properties of particles whose size is large compared to the wavelength of the incident radiation, and strictly speaking, this theory is only valid for spherical and di-electrical particles in the far field. Mie theory is only an estimation for many atmospheric applications. The Mie size parameter

$$\beta = \frac{2\pi r}{\lambda} \, , \tag{B.1}$$

is a coarse parameter that determines if the theory is applicable. r denotes the radius of the scattering particle and λ the incident wavelength. The main contribution for $\beta \ll 1$ is Rayleigh scattering. Atmospheric molecular diameters are typically three magnitudes smaller than the visible wavelength. This scattering is described by the Rayleigh formalism. However, in the microwave region, rain drops are also Rayleigh scatterers. The Mie formalism becomes important at $\beta \gg 0.05$. The scattering coefficient shows an oscillatory dependence on β and depends on other particle properties (Wallace and Hobbs, 1977). The aerosol extinction can be modeled with a parametrization (Hess et al., 1998),

$$\kappa_{ai} = \sigma_{ai}^1 \lambda^{-\alpha_i} \, , \tag{B.2}$$

where typical values are $\alpha_i \in [-0.5, 2]$. σ_i^1 is the aerosol extinction at $\lambda = 1\,\mu\text{m}$. The sum of the aerosol scattering coefficients and the aerosol absorption coefficients yields the aerosol extinction coefficient κ_{ai} for each aerosol type i.

The angular distribution $\zeta_i(\gamma)$ is also described by the Mie theory. The Henyey-Greenstein phase function is a common approximation (Sobolev, 1975),

$$\zeta_i(\gamma) = \frac{1 - g^2}{\left(1 - g^2 - 2\,g\cos\gamma\right)^{3/2}}\,,$$ (B.3)

where γ denotes the scattering angle and g is an asymmetry factor in the range $[-1, 1]$.

In general the absorption by aerosols in the stratosphere is much weaker than scattering and in this case the extinction coefficient is approximated by the scattering coefficient alone,

$$\kappa_{ai} \approx \sigma_{ai}\,.$$ (B.4)

The total aerosol extinction coefficient κ_a is the sum of the individual extinction coefficients,

$$\kappa_a \sum_{i=1}^{N} \approx \sigma_{ai}\,,$$ (B.5)

and the effective aerosol scattering phase function ζ is the average of all individual aerosol scattering phase functions ζ_i weighted with their corresponding scattering coefficients,

$$\zeta = \frac{\sum_{i=1}^{N} \sigma_{ai}\,\zeta_i}{\sum_{i=1}^{N} \sigma_{ai}}\,.$$ (B.6)

The Rayleigh phase function (4.8) and the aerosol phase function (B.3) cannot be added together directly. All possible scattering processes have to be taken into account for a summation (Kaiser, 2001).

C Acknowledgments

It should be mentioned at this juncture that this work was not accomplished by the author of the thesis alone. Without the preparatory and supportive work of the following people this thesis would never have been successful.

The author is at first greatly indebted to Dr. Christian von Savigny, who attended to this thesis with tremendous scientific background and instinct, and friendly personal advice. I thank Prof. Dr. Edward J. (Ted) Llewellyn, who is a great example of how top class science can be done in a human and life-enriching way. It was a great pleasure to work with both of these scientists.

A special thanks is also dedicated to Prof. Dr. John Burrows, the great wirepuller. It is to his merit that he established one of the leading remote sensing groups, thereby giving many researchers the chance to carry out their research. It is no accident that solely visionaries are able to do this work.

The author also thanks Dr. Kai-Uwe Eichmann, Dr. Bernd Sierk, Dr. Michael Buchwitz, Dr. Rüdiger de Beek, Holger Winkler, Dr. Stefan Noël, Dr. Astrid Bracher, Dr. Klaus Bramstedt, Dr. Mark Weber, and Dr. Marco Vountas for their pleasurable and constructive cooperation, Lothar Meyer-Lerbs for his support at the LaTeX setting, Dr. Marco Bruns, Dr. Vladimir Rozanov, and Dr. Alexej Rozanov for dedicated proofreading. I also thank Dr. Johannes Kaiser for his support in terms of SCIARAYS, and Dr. Miriam Sinnhuber for providing the model data.

Finally, I thank Imke Goldenstein for her patience.

D Acronyms

Acronyms	Meanings
AATSR	Advanced Along Track Scanning Radiometer
ASAR	Advanced Synthetic Aperture Radar
BMBF	BundesMinisterium für Bildung und Forschung
CET	Central European Time
CRISTA	CRyogenic Infrared Spectrometers and Telescopes for the Atmosphere
DLR	Deutsches Zentrum für Luft- und Raumfahrt
DORIS	Doppler Orbitography and Radiopositioning Integrated by Satellite
Envisat	Environmental satellite
ERS 2	European Remote Sensing satellite 2
ESA	European Space Agency
FM	Flight Model
FWHM	Full Width at Half Maximum
GEANT4	Giga bit European Academic NeTwork 4
GOES-11	Geostationary Operational Environmental Satellite 11
GOME	Global Ozone Monitoring Experiment
GOMOS	Global Ozone Monitoring by Occultation of Stars
HALOE	Halogen Occultation Experiment
IMK	Institut für Meteorologie und Klimaforschung
LIDAR	Light Detection And Ranging
LORE	Limb Ozone Retrieval Experiment
LRR	Laser RetroReflector
LT	Local Time
MERIS	MEdium Resolution Imaging Specrometer
MIPAS	Michelson Interferometer for Passive Atmospheric Sounding
MLS	Microwave Limb Sounder
MWR	MicroWave Radiometer

continued

Acronyms	Meanings
Nasa	National Aeronautics and Space Administration
Nserc	National Sciences and Engineering Research Council
Osiris	Optical Spectograph and Infra-Red Imaging System
Poam	Polar Ozone and Aerosol Measurement
Ra-2	Radar Altimeter 2
Ram	Radiometer for Atmospheric Measurements
Rsas	Rayleigh Scattering Attitude Sensor
Sage	Stratospheric Aerosol and Gas Experiment
Sbuv	Solar Backscatter UltraViolet
Sciamachy	SCanning Imaging Absorption spectroMeter of Atmospheric CHartographY
Slimcat	Single Layer Isentropic Model of Chemistry And Transport
Sme	Solar Mesosphere Explorer
Solse	Shuttle Ozone Limb Scattering Experiment
True	Tangent height Retrieval by Ultraviolet-B Exploitation
Uars	Upper Atmosphere Research Satellite
Ugamp	Universities Global Atmospheric Modelling Programme
Utc	Universal Time Coordinated
Vk	Vegard-Kaplan
Wmm 2000	World Magnetic Model 2000
Wmo	World Meteorological Organization

E Bibliography

Agostinelli, S., Allison, J., Amako, K. and Apostolakis, J., 2003: GEANT4 – a simulation toolkit. *Nuclear Instruments and Methods in Physics Research, Section A: Accelerators, Spectrometers, Detectors and Associated Equipment*, **503**, 3, 250–303.

Akima, H., 1978: A Method of Bivariate Interpolation and Smooth Surface Fitting for Irregularly Distributed Data Points. ACM *Trans. Math. Software*, **4**, 2, 148–159, ISSN 0098-3500.

van Allen, J. A. and Hopfield, J. J., 1948: Preliminary report on atmospheric ozone measurements from rockets. *Science*, **108**, 746.

Anderson, S. M. and Mauersberger, K., 1992: Laser measurements of ozone absorption cross sections in the Chappuis band. *Geophys. Res. Lett.*, **19**, 9, 933–936.

Avaste, O. A., Fedynsky, A. V., Grechko, G. M., Sevastyanov, V. I. and Willmann, C. I., 1980: Advances in noctilucent cloud research in the space era. *Pure Appl. Geophys.*, **106**, D8, 528–580.

Badger, R. M., Wright, A. C. and Whitlock, R. F., 1965: Absolute intensities of the discrete and continuous absorption bands of oxygen gas at 1.26 and 1.065 μm and the radiative lifetime of the $a^1\Delta_g$ oxygen state. *J. Chem. Phys.*, **43**, 4345–4350.

Baker, D. N., 2000: Effects of the Sun on the Earth's environment. *J. Atmos. Sol.-Terr. Phys.*, **56**, 2, 127–150.

Bates, D. R. and Nicolet, M., 1950: The photochemistry of atmospheric water vapor. *J. Geophys. Res.*, **55**, 301.

Bates, E. R., 1984: Rayleigh scattering by air. *Planet. Space Sci.*, **32**, 6, 785–790.

Baulch, D. L., Cox, R. A., Hampson, R. F., Kerr, J. A., Troe, J. and Watson, R. T., 1980: Evaluated kinetic and photochemical data for atmospheric chemistry. *J. Phys. Chem. Ref. Data*, **9**, 295.

Bertaux, J. L., Megie, G., Chassefiere, T. W. E., Pellinen, R., Kyrölä, E., Korpela, S. and Simon, P., 1991: Monitoring of ozone trend by stellar occultations: the GOMOS instrument. *Adv. Space Res.*, **11**, 237–242.

Bogumil, K., Orphal, J., Homann, T., Voigt, S., Spietz, P., Fleischmann,

O. C., Vogel, A., Hartmann, M., Bovensmann, H., Frerick, J. and Burrows, J. P., 2003: Measurements of molecular absorption spectra with the Sciamachy pre-flight model: Instrument characterization and reference data for atmospheric remote sensing in the 230–2390 nm region. *J. Photochem. Photobiol. A*, **157**, 167–184.

Bovensmann, H., Buchwitz, M., Frerick, J., Hoogeveen, R., Kleipool, Q., Lichtenberg, G., Noël, S., Richter, A., Rozanov, A., Rozanov, V. V., Skupin, J., von Savigny, C., Wuttke, M. and Burrows, J. P., 2004: Sciamachy on Envisat: In-flight optical performance and first results. In *Proceedings of* Spie*: Remote Sensing of Clouds and the Atmosphere*, vol. 5235, K. P. Schäfer and A. Comeron and M. R. Carleer and R. H. Picard.

Bovensmann, H., Burrows, J. P., Frerick, J., Noël, S., Rozanov, V. V., Chance, K. V. and Goede, A. P. H., 1999: Sciamachy: Mission objectives and measurements modes. *J. Atmos. Sci.*, **56**, 2, 127–148.

Bracher, A., Bovensmann, H., Bramstedt, K., Burrows, J. P., von Clarmann, T., Eichmann, K.-U., Fischer, H., Funke, B., Gil-López, S., Glatthor, N., Grabowski, U., Höpfner, M., Kaufmann, M., Kellmann, S., Kiefer, M., Koukouli, M. E., Linden, A., López-Puertas, M., Tsidu, G. M., Milz, M., Noël, S., Rohen, G., Rozanov, A., Rozanov, V. V., v. Savigny, C., Sinnhuber, M., Skupin, J., Steck, T., Stiller, G. P., Wang, D.-Y., Weber, M. and Wuttke, M. W., 2005: Cross comparisons of O_3 and NO_2 measured by the atmospheric Envisat instruments Gomos, Mipas, and Sciamachy. *Adv. Space Res.*, **36**, 855–867, doi `10.1016/j.asr.2005.04.005`.

Brasseur, G. and Solomon, S., 1984: *Aeronomy of the Middle Atmosphere.* Dordrecht: D. Reidel Pub.

Bremer, H., von König, M., Kleinböhl, A., Küllmann, H., Künzi, K., Bramstedt, K., Burrows, J. P., Eichmann, K.-U., Weber, M. and Goede, A. P. H., 2002: Ozone depletion observed by Asur during the arctic winter 1999/2000. *J. Geophys. Res.*, **107**, D20, doi `10.1029/2001JD000546`.

Brühl, C., Drayson, S. R., Russell, J. M., Crutzen, P. J., McInerney, J. M., Purcell, P. N., Claude, H., Gernandt, H., McGee, T. J., McDermid, I. S. and Gunson, M. R., 1996: Halogen Occultation Experiment ozone channel validation. *J. Geophys. Res.*, **101**, 10 217–10 240, doi `10.1029/95JD02031`.

Buchwitz, M., 2000: *Strahlungstransport- und Inversions-Algorithmen zur Ableitung atmosphärischer Spurengasinformationen aus Erdfernerkundungsmessungen in Nadirgeometrie im ultravioletten bis nahinfraroten Spektralbereich am Beispiel* Sciamachy. Ph.D. thesis, Universität Bremen.

Buchwitz, M., de Beek, R., Burrows, J. P., Bovensmann, H., Warneke, T., Notholt, J., Meirink, J. F., Goede, A. P. H., Bergamaschi, P., Körner, S., Heimann, M. and Schulz, A., 2005: Carbon monoxide, methan and carbon dioxide columns retrieved from Sciamachy by Wmf-doas: Year 2003 initial data set. *Atmos. Chem. Phys.*, **5**, 1943–1971.

Burrows, J. P. and Chance, K. V., 1991: SCanning Imaging Absorption spectrometer for Atmospheric CHartographY. In *Proc. of* Spie, vol. 1490.

Burrows, J. P., Hölzle, E., Goede, A. P. H., Visser, H. and Fricke, W., 1995: Sciamachy – Scanning Imaging Absorption Spectrometer for Atmospheric Chartography. *Acta. Astronautica*, **35**, 7, 445–451.

Burrows, J. P., Richter, A., Dehn, A., Deters, B., Himmelmann, S., Voigt, S. and Orphal, J., 1999a: Atmospheric remote-sensing reference data from Gome: 2. Temperature-dependent absorption cross sections of O_3 in the 231–794 range. *J. Quant. Spectrosc. Radiat. Transfer*, **61**, 509–517.

Burrows, J. P., Weber, M., Buchwitz, M., Rozanov, V., Weissenmayer, A. L., Richter, A., de Beek, R., Hoogen, R., Bramstedt, K., Eichmann, K.-U., Eisinger, M. and Perner, D., 1999b: The Global Ozone Monitoring Experiment (Gome): Mission concept and first scientific results. *J. Atmos. Sci.*, **56**, 151–175.

Carbary, J. F., Morrison, D., Romick, G. J. and Yee, J.-H., 2003: Leonid meteor spectrum from 110 to 860 nm. *Icarus*, **161**, 223–234.

Chapman, S., 1929: On the variations of ozone in the upper atmosphere. *Gerlands Beitr. Geophys.*, **24**, 66.

Chapman, S., 1930: A theory of the upper atmospheric ozone. *Mem. Roy. Meteor. Soc.*, **3**, 130.

Chappuis, J., 1880: Sur le spectre d'absorption de l'ozone. *C. R. Acad. Sci. Paris*, **91**, 985.

Chipperfield, M. P., 1999: Multiannual simulations with a three dimensional chemical transport model. *J. Geophys. Res.*, **104**, 1781–1805.

Chipperfield, M. P., Santee, M. L., Froidevaux, L., Manney, G. L., Read, W. G., Waters, J. W., Roche, A. E. and Russell, J. M., 1996: Analysis of Uars data in the southern polar vortex in September 1992 using a chemical transport model. *J. Geophys. Res.*, **101**, 18 861–18 881.

von Clarmann, T., Fischer, H., Funke, B., Glatthor, N., Grabowski, U., Höpfner, M., Kiefer, M., Martin-Torres, F. J., Milz, M. and Stiller, G. P., 2001: Mipas interactive semi-operational level-2 data processing. In *Current Problems in Atmospheric Radiation*, Smith, W. L. and Timofeyev, Y. M., eds., Hampton, Va.: A. Deepak Publ.

von Clarmann, T., Glatthor, N., Grabowski, U., Höpfner, M., Kellmann, S., Kiefer, M., Linden, A., Mengistu Tsidu, G., Milz, M., Steck, T., Stiller,

G. P., Wang, D. Y., Fischer, H., Funke, B., Gil-López, S. and López-Puertas, M., 2003: Retrieval of temperature and tangent altitude pointing from limb emission spectra recorded from space by the Michelson Interferometer for Passive Atmospheric Sounding (Mipas). *J. Geophys. Res.*, **108**, D23.

Clemesha, B. R., 1995: Sporadic neutral metal layers in the mesosphere and lower thermosphere. *J. Atmos. Sol.-Terr. Phys.*, **57**, 725–736.

Crutzen, P. J., 1970: The influence of nitrogen oxides on the atmospheric ozone content. *Quart. J. Roy. Meteorol. Soc.*, **96**, 320–325.

Crutzen, P. J., Isaksen, I. S. A. and Reid, G. C., 1975: Solar proton events: Stratospheric sources of nitric oxide. *Science*, **189**, 457–458.

Dalgarno, A. and Williams, D. A., 1962: Raman and Rayleigh scattering of Lyman-α by molecular hydrogen. *Mon. Not. R. Astron. Soc.*, **124**, 313–319.

Degenstein, D. A., 1999: *Atmospheric volume emission tomography from a satellite platform*. Ph.D. thesis, Department of Physics and Physics Engineering, University of Saskatchewan, Saskatoon, Sasketchewan, Canada.

Edlén, B., 1966: The dispersion of standard air. *Appl. Opt.*, **43**, 339–344.

Endemann, M. and Fischer, H., 1993: Envisat's high resolution limb sounder: Mipas. *ESA Bull.*, **76**, 47–52.

Esa, 2001: *Envisat Gomos, an Instrument for Global Atmospheric Ozone Monitoring*. Tech. Rep. SP-1244, Esa, Esa Publications Division, Estec, P.O. Box 299, 2200 Noordwijk, Netherlands.

Esa, 2005: url www.envisat.esa.int. Envisat Homepage.

Evans, W. F. J., Hunten, D. M., Llewellyn, E. J. and Vallance-Jones, A., 1968: Altitude profile of the Infrared Atmospheric system of oxygen in the dayglow. *J. Geophys. Res.*, **73**, 2885.

Evans, W. F. J. and Llewellyn, E. J., 1970: Ground based photometric observations of the $1.27\,\mu$ band in the evening twilight. *Planet. Space Sci.*, **18**, 1065.

Evans, W. F. J., McDade, E. C., Yuen, J. and Llewellyn, E. J., 1988: A rocket measurement of the O_2 infrared atmospheric band $(0,0)$ emission in the dayglow and a determination of the mesospheric ozone and atomic oxygen densities. *Can. J. Phys.*, **66**, 941–946.

Fabry, C. and Buisson, H., 1921: A study of the ultra-violet end of the solar spectrum. *Astrophys. J.*, **54**, 297.

Farman, J. C., Gardiner, B. G. and Shanklin, J. D., 1985: Large ozone losses of total ozone in Antarctica reveal seasonal ClO_x/NO_x interaction. *Nature*, **315**, 207–210.

Fischer, H. and Oelhaf, H., 1996: Remote sensing of vertical profiles of

atmospheric trace constituents with Mipas limb-emission spectrometers. *Appl. Opt.*, **35**, 16, 2787–2796.

Fleig, A., McPeters, R., Barthia, P. K., Schlesinger, B., Cebula, R., Klenk, K., Taylor, S. and Heath, D., 1990: *Nimbus 7 Solar Backscatter Ultraviolet (*Sbuv*) ozone products user's guide.* Tech. Rep. 1234, Nasa Reference Publication.

Flittner, D. E., Bhartia, P. K. and Herman, B. M., 2000: O_3 profiles retrieved from limb scatter measurements: Theory. *Geophys. Res. Lett.*, **27**, 17, 2601–2604.

Frerick, J. H., Bovensmann, H., Noël, S. and Dobber, M., 1997: Sciamachy on-ground/in-flight calibration, performance verification and monitoring concepts. In *Proceedings of* Spie, vol. 3117.

Friedl-Vallon, F., Maucher, G., Kleinert, A., Lengl, A., Keim, C., Oelhaf, H., Fischer, H., Seefeldner, M. and Trieschmann, O., 2004: Design and characterization of the balloon-borne Michelson Interferometer for Passive Atmospheric Sounding. *Appl. Opt.*, **43**, 3335–3355.

Fritzenwallner, J. and Kopp, E., 1998: Model calculations of the silicon and magnesium chemistry in the mesosphere and lower thermosphere. *Adv. Space Res.*, **21**, 859–862.

Froidevaux, L., 1996: Validation of Uars Microwave Limb Sounder ozone measurements. *J. Geophys. Res.*, **101**, 10 017–10 060.

Glatthor, N., von Clarmann, T., Fischer, H., Funke, B., Grabowski, U., Höpfner, M., Kellmann, S., Kiefer, M., Linden, A., Milz, M., Steck, T., Stiller, G. P., Mengistu Tsidu, G. and Wang, D. Y., 2005: Mixing processes during the Antarctic vortex split in September/October 2002 as inferred from source gas and ozone distributions from Envisat-Mipas. *J. Atmos. Sci.*, **62**, 3, 787–800.

Goede, A. P., Hoogeveen, R. W. M., de Vries, J., van der A, R. J., Smorenburg, C. and Visser, H., 1994: Sciamachy instrument development for Poem 1. *Adv. Space Res.*, **14**, 17–20.

Götz, F. W. P., Meetham, A. R. and Dobson, G. M. B., 1934: The vertical distribution of ozone in the atmosphere. *Proc. R. Soc. London*, **A145**, 416.

Hartley, W. N., 1881: On the absorption of solar rays by atmospheric ozone. *J. Chem. Soc. A.*, **39**, 111.

Herzberg, G., 1950: *Spectra of Diatomic Molecules.* New York: D. Van Nostrand Co.

Hess, M., Koepke, P. and Schult, I., 1998: Optical properties of aerosols and clouds: the software package Opac. *Bull. Amer. Meteorol. Soc.*, **79**, 5, 831–844.

Hilsenrath, E., 1971: Ozone measurements in the mesosphere and strato-
    sphere during two significant geophysical events. *J. Atmos. Sci.*, **28**, 295.

Hoxit, L. R. and Henry, R. M., 1973: Diurnal and annual temperature vari-
    ations in the 30–60 km as indicated by statistical analysis of rocketsonde
    temperature data. *J. Atmos. Sci.*, **30**, 5, 922–933.

Huffman, R. E., 1992: *Atmospheric Ultraviolet Remote Sensing.* Interna-
    tional Geophysics Series Vol. 52, San Diego: Academic Press.

Jackman, C. H., DeLand, M. T., Labow, G. J., Fleming, E. L., Weisenstein,
    D. K., Ko, M. K. W., Sinnhuber, M., Anderson, J. and Russell, J. M.,
    2005a: The influence of the several very large solar proton events in years
    2000–2003 on the neutral middle atmosphere. *Adv. Space Res.*, **35**, 445–
    450.

Jackman, C. H., DeLand, M. T., Labow, G. J., Fleming, E. L., Weisenstein,
    D. K., Ko, M. K. W., Sinnhuber, M. and Russell, J. M., 2005b: Neutral
    atmospheric influences of the solar proton events in October-November
    2003. *J. Geophys. Res. (Space Phys.)*, **110**, A9, S27.

Jackman, C. H., Fleming, E. L., Chandra, S., Considine, D. B. and Rosen-
    field, J. E., 1996: Past, present and future modeled ozone trends with
    comparisons to observed trends. *J. Geophys. Res.*, **101**, 28 753–28 767.

Jackman, C. H. and McPeters, R. D., 2004: The effect of solar proton
    events on ozone and other constituents. In *Solar Variability and its Effects
    on Climate*, no. 10.1029/141Gm21 in Geophysical Monograph, American
    Geophysical Union, 305–319.

Janz, S. J., Hilsenrath, E., Flittner, D. and Heath, D., 1996: Rayleigh scat-
    tering attitude sensor. *Proc. of* Spie, **2831**, 146–153.

Johnson, B. R. and Kinsey, J. L., 1989: Dynamical interpretation of the
    Hartley-absorption oscillations in O_3. *Phys. Rev. Lett.*, **62**, 607–1610.

Joiner, J., Barthia, P. K., Cebula, R. P., Hilsenrath, E., McPeters, R. D.
    and Park, H., 1995: Rotational Raman scattering (Ring effect) in satellite
    backscatter ultraviolet measurements. *Appl. Opt.*, **34**, 4513–4525.

Jones, A. V. and Harrison, A. W., 1958: $a^1\Delta_g - X^3\Sigma_g^- - O_2$ infrared emission
    band in the twilight airglow spectrum. *J. Atmos. Terr. Phys.*, **13**, 45–60.

Kaiser, J. W., 2001: *Atmospheric Parameter Retrieval from Ultraviolet, Vi-
    sible, Near-Infrared Limb Scattering Measurements.* Ph.D. thesis, Univer-
    sity of Bremen.

Kaiser, J. W., von Savigny, C., Eichmann, K.-U., Noël, S., Bovensmann, H.
    and Burrows, J. P., 2004: Satellite-pointing retrieval from atmospheric
    limb-scattering of solar Uv-B radiation. *Can. J. Phys.*, **82**, 1041–1052.

Kaufmann, M. O., Gusev, O. A., Grossmann, K. U., Martin-Torres, F. J.,
    Marsh, D. R. and Kutepov, A. A., 2003: Satellite observations of day-

time and nighttime ozone in the mesosphere and lower thermosphere. *J. Geophys. Res.*, **108**, D9, 4272–4285.

King, L. V., 1923: On the complex anisotropic molecule in relation to the dispersion and scattering of light. *Proc. Roy. Soc. Lond.*, **A104**, 333–357.

Kinnersley, J. S., 1996: The climatology of the stratospheric THIN AIR model. *Quart. J. Roy. Meteorol. Soc.*, **122**, 219–252.

Kokhanovsky, A., 2005: Microphysical and optical properties of noctilucent clouds. *Earth Sci. Rev.*, **71**, 127–146.

Krüger, A. J., Günther, B., Fleig, A. J., Heath, D. F., Hilsenrath, E., McPeters, R. and Prabhakara, C., 1980: Satellite ozone measurements. *Phil. Trans. R. Soc. Lond.*, **A296**, 191–204.

Kyrölä, E., Tamminen, J., Leppelmeier, G. W., Sofieva, V., Hassinen, S., Bertaux, J. L., Hauchecorne, A., Dalaudier, F., Cot, C., Korablev, O., d'Anton, O. F., Barrot, G., Mangin, A., Théodore, B., Guirlet, M., Etanchaud, F., Snoeij, P., Koopman, R., Saavedra, L., Fraisse, R., Fussen, D. and Vanhellmont, F., 2004: GOMOS on Envisat: An overview. *Adv. Space Res.*, **33**, 7, 1020–1028.

Langer, J., 1999: *Comparison of ozone-measurements at Ny-Alesund, Spitsbergen, in 1997 and 1998*. Ph.D. thesis, University of Bremen. In German.

Lary, D., 1997: Catalytic destruction of stratospheric ozone. *J. Geophys. Res.*, **102**, 21 515–21 526.

Lenoble, J., 1993: *Atmospheric Radiative Transfer: Standard Computational Procedures*. Hampton, Virginia, Usa: A. DEEPAK Publishing.

Leslie, R. C., 1885: Sky glows. *Nature*, **32**, 245.

Lichtenberg, G., Kleipool, Q., Krijger, J. M., van Soest, G., van Hees, R., Tilstra, L. G., Acarreta, J. R., Aben, I., Ahlers, B., Bovensmann, H., Chance, K., Cloudemans, A. M. S., Hoogeveen, R. W. M., Jongma, R., Noël, S., Pieters, A., Schrijver, H., Schrijvers, C., Sioris, C. E., Skupin, J., Slijkhuis, S., Stammes, P. and Wuttke, M., 2005: SCIAMACHY level 1 data: Calibration concept and in-flight calibration. *Atmos. Chem. Phys.*, **5**, 8925–9877.

Llewellyn, E. J., Evans, W. F. J. and Wood, H. C., 1973: $O_2(a^1\Delta_g)$ in the Atmosphere. In *ASSL Vol. 35: Physics and Chemistry of Upper Atmospheres*.

Llewellyn, E. J. and Gattinger, R. L., 1998: *Estimated* OSIRIS *ultraviolet/visible baffle on-orbit performance*. Tech. Rep., University of Saskatchewan.

Llewellyn, E. J. and Witt, G., 1977: The measurements of ozone concentrations at high latitudes during the twilight. *Planet. Space Sci.*, **25**, 2, 165–172.

López-Gonzáles, M. J., López-Moreno, J. J. and Rodrigo, R., 1992: The altitude profile in the infrared atmospheric system of O_2 in twilight and early night: Derivation of ozone abundances. *Planet. Space Sci.*, **40**, 1391–1397.

López-Puertas, M., 2000: *Definition of observational requirements for support to a future Earth explorer atmospheric chemistry mission.* Tech. Rep. ESTEC Contract Number 13048/98/NL/DG, WP 6000: Molecular Non-Local Thermodynamic Equilibrium Working Document V2.0, Instituto de Astrofisica de Andalucia (CSIC), Granada, Spain.

Lucke, R. L., Korwan, D., Bevilacqua, R. M., Hornstein, J. S., Shettle, E. P., Chen, D. T., Daehler, M., Lumpe, J. D., Fromm, M. D., Debrestian, D., Neff, B., Squire, M., König-Langlo, G. and Davis, J., 1999: The Polar Ozone and Aerosol Measurement (POAM III) instrument and early validation results. *J. Geophys. Res.*, **104**, 18 785–18 799.

Lumpe, J. D., Randall, C. E., Bevilacqua, R. M., Hoppel, K. W., Nedoluha, G. E. and Prados, A. I., 2003: POAM III Validation Summary. AGU *Fall Meeting Abstracts*, D711.

Macmillan, S. and Quinn, J. M., 2000: *The Derivation of World Magnetic Model 2000.* Tech. Rep. WM/00/17R, British Geological Survey, Edinburgh.

McCormack, J. P. and Hood, L. L., 1996: Apparent solar cycle variations of upper stratospheric ozone and temperature: Latitude and seasonal dependences. *J. Geophys. Res.*, **101**, D15, 20 933–20 944.

McLinden, C. A., Olsen, S. C., Hannegan, B., Wild, O. and Prather, M. J., 2000: Stratospheric ozone in 3-D models: A simple chemistry and the cross-tropopause flux. *J. Geophys. Res.*, **105**, 14 653–14 665.

McPeters, R., 1993: Ozone profile comparisons. In *The Atmospheric Effects of Stratospheric Aircraft: Report of the 1992 Models and Measurement Workshop*, no. 1292 in NASA Reference Publ., M. J. Prather and E. E. Remsberg, D31–D37.

McPeters, R. D., Janz, S. J., Hilsenrath, E., Brown, T. L., Flittner, D. E. and Heath, D. F., 2000: The retrieval of O_3 profiles from limb scatter measurements: Results from the Shuttle Ozone Limb Sounding Experiment. *Geophys. Res. Lett.*, **27**, 17, 2597–2600.

Meyer, J., Bracher, A., Rozanov, A., Schlesier, A. C., Bovensmann, H. and Burrows, J. P., 2005: Solar occultation with SCIAMACHY: algorithm description and first validation. *Atmos. Chem. Phys.*, **5**, 1589–1604.

Mie, G., 1908: Beiträge zur Optik trüber Medien, speziell kolloidaler Metallösungen. *Annalen der Physik*, **25**, 3, 377–445.

Miller, A. J., 1989: A review of satellite observations of atmospheric ozone. *Planet. Space Sci.*, **37**, 12.

Mlynczak, M. G. and Olander, D. S., 1995: On the utility of the molecular oxygen dayglow emissions as proxies for middle atmospheric ozone. *Geophys. Res. Lett.*, **22**, 11, 1377–1380.

Molina, M. J. and Rowland, F. S., 1974: Stratospheric sink for chlorofluoromethanes: Chlorine atom catalyzed destruction of ozone. *Nature*, **249**, 810.

Moore, C. E., 1971: *Atomic energy levels (Nat. Stand. Ref. Data Ser., 35)*, vol. 1. Nbs.

Nagatani, R. M. and Rosenfield, J. E., 1993: Temperature, net heating and circulation. In *The Effect of Stratospheric Aircraft: Report of the 1992 Models and Measurement Workshop*, no. 1292 in Nasa Reference Publ., M. J. Prather and E. E. Remsberg, A1–A47.

Natarajan, M. L., Deaver, L. E., Thompson, E. and Magill, B., 2005: Impact of twilight gradients on the retrieval of mesospheric ozone from Haloe. *J. Geophys. Res.*, **110**, D13305.

Nazarayan, H., McCormick, M. P. and Russell, J. M., 2005: New studies of Sage ii and Haloe ozone profile and long-term change comparisons. *J. Geophys. Res. (Atmos.)*, **110**, D9, 9305.

Noxon, J. F., 1975: Twilight enhancements in $O_2(b^1\Sigma_g)$ emission. *J. Geophys. Res.*, **80**, 1370–1373.

Orphal, J., 2002: *A critical review of the absorption cross sections of* O_3 *and* NO_2 *in the 240–790 nm region, part I: ozone.* Tech. Rep. Technical note Mo-Tn-Esa-Go-0302, Esa.

Orsolini, Y. J., Manney, G. L., Santee, M. L. and Randall, C. E., 2005: An upper stratospheric layer of enhanced HNO_3 following exceptional solar storms. *Geophys. Res. Lett.*, **32**, L12S01.

Palm, M., von Savigny, C., Warneke, T., Velazco, V., Notholt, J., Künzi, K., Burrows, J. and Schrems, O., 2005: Intercomparison of O_3 profiles observed by Sciamachy and ground based microwave instruments. *Atmos. Chem. Phys.*, **5**, 2091–2098.

Peck, E. R. and Reeder, K., 1972: Dispersion of air. *J. Opt. Soc. America*, **62**, 8, 958–962.

Porter, H. S., Jackman, C. H. and Green, A. E. S., 1976: Efficiencies for production of atomic nitrogen and oxygen by relativistic proton impact. *J. Chem. Phys.*, **65**, 154–167.

Prölls, G. W., 2003: *Physik des erdnahen Weltraums.* Berlin: Springer.

Randall, C. E., Harvey, V. L., Manney, G. L., Orsolini, Y., Codrescu, M., Sioris, C., Brohede, S., Haley, C. S., Gordley, L. L., Zawodny,

J. M. and Russell, J. M., 2005: Stratospheric effects of energetic particle precipitation in 2003–2004. *Geophys. Res. Lett.*, **32**, 5802, DOI 10.1029/2004GL022003.

Rees, M. H., 1989: *Physics and chemistry of the upper atmosphere.* Cambridge: Cambridge University Press.

Reid, G. C., 2001: *Solar energetic particles and their effects on their terrestrial environment.* Dordrecht: D. Reidel Publishing.

Richter, J. P., 1970: *The literary works of Leonardo da Vinci*, vol. I. London: Phaidon.

Rodgers, C. D., 2000: *Inverse Methods for Atmospheric Sounding.* Oxford: World Scientific Publishing.

Rohen, G., von Savigny, C., Sinnhuber, M., Llewellyn, E. J., Kaiser, J. W., Jackman, C. H., Kallenrode, M.-B., Schröter, J., Eichmann, K.-U., Bovensmann, H. and Burrows, J. P., 2005: Ozone depletion during the solar proton events of October/November 2003 as seen by SCIAMACHY. *J. Geophys. Res.*, **110**, A9, A09S39, DOI 10.1029/2004JA010984.

Rohen, G. J., von Savigny, C., Llewellyn, E. J., Kaiser, J. W., Eichmann, K.-U., Bracher, A., Bovensmann, H. and Burrows, J. P., 2006: First results of ozone profiles between 35 and 65 km retrieved from SCIAMACHY limb spectra and observations of ozone depletion during the solar proton events in Oct./Nov. 2003. *Adv. Space Res.*, **37**, 12, 2263–2268, DOI 10.1016/j.asr.2005.03.160.

Rosenfield, J. E., Newman, P. A. and Schoeberl, M. R., 1994: Computation of the diabatic descent in the stratospheric polar vortex. *J. Geophys. Res.*, **99**, D8, 16 677–16 689.

Rothman, L. S., Rinsland, C. P., Goldman, A., Massie, S. T., Edwards, D. P., Flaud, J.-M., Perrin, A., Camy-Peyret, C., Dana, V., Mandin, J.-Y., Schroeder, J., McCann, A., Gamasche, R. R., Wattson, R. B., Yoshino, K., Chance, K. V., Jucks, K. W., Brown, L. R., Nemtschinov, V. and Varanasi, P., 1998: The HITRAN molecular spectroscopic database and HAWKS (HITRAN Atmospheric Workstation): 1996 edition. *J. Quant. Spectrosc. Radiat. Transfer*, **60**, 5, 665–710.

Rozanov, A., Bovensmann, H., Bracher, A., Hrechanyy, S., Rozanov, V., Sinnhuber, M., Stroh, F. and Burrows, J. P., 2005: NO_2 and BrO vertical profile retrieval from SCIAMACHY limb measurements: Sensitivity studies. *Adv. Space Res.*, **36**, 5, 846–854.

Rozanov, V. V., Diebel, D., Spurr, R. J. D. and Burrows, J. P., 1997: GOMETRAN: A radiative transfer model for the satellite project GOME; the plan-parallel version. *J. Geophys. Res.*, **102**, D14, 16 683–16 695.

Rusch, D. W., Bevilacqua, R. M., Randall, C. E., Lumpe, J. D., Hoppel,

K. W., Fromm, M. D., Debrestian, D. J., Olivero, J. J., Hornstein, J. H., Guo, F. and Shettle, E. P., 1997: Validation of POAM ozone measurements with coincident MLS, HALOE, and SAGE II observations. *J. Geophys. Res.*, **102**, 23 615–23 628.

Rusch, D. W., Gerard, J.-C., Solomon, S., Crutzen, P. J. and Reid, G. C., 1981: The effect of particle precipitation events on the neutral and ion chemistry of the middle atmosphere – I. Odd nitrogen. *Planet. Space Sci.*, **29**, 767–774.

Rusch, D. W., Mount, G. H., Barth, C. A., Rottmann, G. J., Thomas, R. J., Thomas, G. E., Sanders, R. W., Lawrence, G. M. and Eckman, R. S., 1983: Ozone densities in the lower mesosphere measured by a limb scanning UltraViolet Spectrometer. *Geophys. Res. Lett.*, **10**, 4, 241–244.

Rusch, D. W., Mount, G. H., Barth, C. A., Thomas, R. J. and Callan, M. T., 1984: Solar Mesosphere Explorer Ultraviolet Spectrometer: Measurements of ozone in the 1.0–0.1 mbar region. *J. Geophys. Res.*, **89**, D7, 11 677–11 687.

Russell, J. M., Gordley, L. L., Park, J. H., Drayson, S. R., Hesketh, W. D., Cicerone, R. J., Tuck, A. F., Frederick, J. E., Harries, J. E. and Crutzen, P. J., 1993: The Halogen Occultation Experiment. *J. Geophys. Res.*, **98**, 10 777–10 797.

von Savigny, C., 2002: *Retrieval of Stratospheric Ozone Density Profiles from OSIRIS Scattered Sunlight Observations.* Ph.D. thesis, York University Toronto.

von Savigny, C., Bovensmann, H. and Kaiser, J. W., 2004: SCIAMACHY *limb pointing retrieval report – improvement of pointing performance after the December 2003 update.* Tech. Rep., University of Bremen.

von Savigny, C., Kaiser, J. W., Bovensmann, H., Burrows, J. P., McDermid, I. S. and Leblanc, T., 2005a: Spatial and temporal characterization of SCIAMACHY limb pointing errors during the first three years of the mission. *Atmos. Chem. Phys.*, **5**, 2593–2602.

von Savigny, C., Rozanov, A., Bovensmann, H., Eichmann, K.-U., Noël, S., Rozanov, V., Sinnhuber, B.-M., Weber, M., Burrows, J. P. and Kaiser, J. W., 2005b: The ozone hole breakup in September 2002 as seen by SCIAMACHY on Envisat. *J. Atmos. Sci.*, **62**, 721–734.

Schoeberl, M. R. and Hartmann, D. L., 1991: The dynamics of the stratospheric polar vortex and its relation to springtime ozone depletion. *Science*, **251**, 46–52.

Schönbein, C. F., 1840: Recherches sur la nature de l'd odeur qui se manifeste dans certaines actions chimiques. *Comptes Rendus Acad. Sciences*, **10**, 706–710.

Schröter, J., Heber, B., Steinhilber, F. and Kallenrode, M.-B., 2005: Energetic particles in the atmosphere: A Monte-Carlo simulation. *Adv. Space Res.* In press.

Schwab, A., Mager, R. and Fricke, W., 1996: SCIAMACHY *pointing error budget.* Tech. Rep. TN-SCIA-0000DO/06, A, Dornier.

Seppälä, A., Veronnen, P. T., Kyrölä, E., Hassinen, S., Backman, L., Hauchecorne, A., Bertaux, J. L. and Fussen, D., 2004: Solar proton events on October - November 2003: Ozone depletion in the northern hemisphere polar winter as seen by GOMOS/Envisat. *J. Geophys. Res.*, **31**, L190 107, DOI 10.1019/2004GL020142.

Shumilov, O. I., Kasatkina, E. A., Henriksen, K. and Vashenyuk, E. V., 1996: Enhancements of stratospheric aerosols after solar proton event. *Ann. Geophys.*, **14**, 1119–1123.

Sioris, C. E., Haley, C. S., McLinden, C. A., von Savigny, C., McDade, I. C., McConnell, J. C., Evans, W. F. J., Lloyd, N. D., Llewellyn, E. J., Chance, K. V., Kurosu, T. P., Murtagh, D., Frisk, U., Pfeilsticker, K., Bösch, H., Weidner, F., Strong, K., Stegman, J. and Mégie, G., 2003: Stratospheric profiles of nitrogen dioxide observed by OSIRIS on the Odin satellite. *J. Geophys. Res.*, **108**, 4215–4234, DOI 101029/2002JD002672.

Sobolev, V. V., 1975: *Light scattering in planetary atmospheres*. Pergamon Press.

van Soest, G., 2005: *Investigation of* SCIAMACHY *limb spatial straylight.* Tech. Rep. SRON-EOS-RP-05-006, SRON.

Solomon, S. and Crutzen, P. C., 1981: Analysis of the August 1972 solar proton event including chlorine chemistry. *J. Geophys. Res.*, **86**, 1140–1146.

Solomon, S., Reid, G. C., Rusch, D. W. and Thomas, R. J., 1983: Mesospheric ozone depletion during the solar proton event of July 13, 1982. Part II. Comparison between theory and measurements. *Geophys. Res. Lett.*, **10**, 257–260.

Steck, T., Blumenstock, T., von Clarmann, T., Glatthor, N., Grabowski, U., Hase, F., Hochschild, G., Höpfner, M., Kellmann, S., Kopp, G., Linden, A., Milz, M., Oelhaf, H., Stiller, G. P., Wetzel, G., Zhang, G., Fischer, H., Funke, B., Wang, D. Y., von der Gathen, P., Hansen, G., Kyrölä, E., Pieters, A., Redondas, A., Steinbrecht, W. and Yela, M., 2006: Validation of MIPAS-IMK ozone profiles. In MIPAS *Data User Meeting*, IMK Karlsruhe.

Steinfeld, J. I., Alder-Golden, S. M. and Gallagher, J. W., 1987: Critical survey of data on the spectroscopy and kinetics of ozone in the mesosphere and thermosphere. *J. Phys. Chem. Ref. Data*, **16**, 4, 911–951.

Stolarski, R. and Cicerone, R., 1974: Stratospheric chlorine: a possible sink for ozone. *Can. J. Chem.*, **52**, 1610.

Strutt, J. W., 1871: On the scattering of light by small particles. *The London, Edinburgh and Dublin Philosophical Magazine and Journal*, **41**, 102, 447–454.

Swider, W. and Kenesha, T. J., 1973: Decrease of ozone and atomic oxygen in the lower mesosphere during a PCA event. *Planet. Space Sci.*, **21**, 1969.

Thomas, G. E., Barth, C. A., Hansen, E. R., Hord, C. W., Mount, G. M., Rottman, G. H., Rusch, D. W., Stewart, A. I., Thomas, R. J., London, J., Bailey, P. L., Crutzen, P. J., Dickenson, R. E., Gille, J. C., Liu, S. C., Noxon, J. J. and Farmer, C. B., 1980: Scientific objectives of the Solar Mesosphere Explorer mission. *Pure Appl. Geophys.*, **118**, 591–615.

Thomas, G. E. and Olivero, J. J., 1989: Climatology of polar mesospheric clouds, 2. Further analysis of Solar Mesosphere Explorer data. *J. Geophys. Res.*, **94**, 14 673–14 681.

Thomas, R. J., Barth, C. A., Rottman, G. J., Rusch, D. W., Mount, G. H. and Lawrence, G. M., 1983: Ozone densities in the mesosphere (50–90 km) measured by the SME limb scanning near infrared spectrometer. *Geophys. Res. Lett.*, **20**, 245.

Trinks, H., 1975: Ozone measurements between 90 and 110 km altitude by mass spectrometer. *Geophys. Res. Lett.*, **2**, 99–102.

Twomey, S., 1977: *Introduction to the Mathematics of Inversion in Remote Sensing and Indirect Measurement*. Amsterdam: Elsevier Scientific Publishing Company.

Vitt, F. M. and Jackman, C. H., 1996: A comparison of sources of odd nitrogen production from 1974 through 1993 in the Earth's middle atmosphere as calculated using a two-dimensional model. *J. Geophys. Res.*, **101**, 6729–6739.

Wallace, J. M. and Hobbs, P. V., 1977: *Atmospheric Science*. New York: Academic Press.

Wayne, R. P., 1985: *Chemistry of the Atmospheres*. Oxford: Oxford Science Publications.

Wayne, R. P., 1987: The Photochemistry of Ozone. *Atmos. Env.*, **21**, 1683–1694.

Weeks, L. H., Chuikay, R. S. and Corbin, J. R., 1972: Ozone measurements in the mesosphere during the solar proton event of 2 November 1969. *J. Atmos. Sci.*, **29**, 1138–1142.

Weeks, L. H., Good, R. E., Randhawa, J. S. and Trinks, H., 1978: Ozone measurements in the stratosphere, mesosphere, and lower thermosphere during Aladdin 74. *J. Geophys. Res.*, **83**, 978–982.

Wilson, W. J. and Schwartz, P. R., 1981: Diurnal variations of mesospheric ozone using millimeter-wave measurements. *J. Geophys. Res.*, **86**, 7385–7388.

Winick, J. R., Picard, R. H., Sharma, R. D. and Nadile, R. M., 1985: Oxygen singlet delta 1.58-micrometer $(0, 1)$ limb radiance in the upper stratosphere and lower mesosphere. *J. Geophys. Res.*, **90**, A10, 9804–9814.

WMO, 1986: *Atmospheric Ozone 1985*. Tech. Rep. 16, World Meteorological Organization, Geneva.

Wofsy, S., McElroy, M. and Yung, Y., 1975: The chemistry of atmospheric bromine. *Geophys. Res. Lett.*, **2**, 215–218.

Young, A. T., 1980: Revised depolarization corrections for atmospheric extinction. *Appl. Opt.*, **19**, 20, 3427–3428.